4D Strain from Tagged Magnetic Resonance Images by Unwrapping the Harmonic Phase Images

by

Bharath Ambale Venkatesh

A dissertation submitted to the Graduate Faculty of
Auburn University
in partial fulfillment of the
requirements for the Degree of
Doctor of Philosophy

Auburn, Alabama
May 9th 2011

Keywords: magnetic resonance imaging, tagged MRI, harmonic phase, phase unwrapping, ventricles, strain, torsion, hysteresis

Approved by

Thomas S. Denney Jr., Chair, Professor of Electrical and Computer Engineering
Stanley J. Reeves, Professor of Electrical and Computer Engineering
Jitendra Tugnait, Professor of Electrical and Computer Engineering

Abstract

Accurate assessment of ventricular function is clinically important. Tagged magnetic resonance imaging (MRI) is the modality of choice for calculating parameters such as torsion, rotation and strain that characterize regional myocardial function. In this dissertation, a method for reconstructing three-dimensional strain over time from unwrapped harmonic phase measurements obtained from tagged MRI is presented. The procedure involved the placement of branch cuts before unwrapping the phase images to remove inconsistencies and obtaining displacement measurements. An affine prolate spheroidal B-spline (APSB) model was then used to reconstruct strain from the estimated displacement measurements. Initially, this method was implemented to obtain strain and torsion in the left ventricle (LV) by the manual placement of branch cuts through a graphical user interface (GUI) before unwrapping. This procedure is known as manual Strain from Unwrapped Phase (mSUP). The strain obtained was compared to 3D strain obtained from a feature-based method and 2D strain obtained from harmonic phase strain measurements.

A method called the biventricular strain from unwrapped phase (BiSUP) for reconstructing three-dimensional plus time (3D+t) biventricular strain maps from unwrapped harmonic phase (HARP) images was then introduced. This is an extension of mSUP to obtain 3D+t strain in the right ventricle (RV). Accurate assessment of RV function is clinically important. Compared to LV, however, analysis of RV function is relatively difficult because of a lack of geometric symmetry and the comparatively thinner myocardium. Displacement estimates were obtained from unwrapped harmonic phase measurements, in a procedure similar to the mSUP, and were then used to reconstruct 3D strain using a discrete model free (DMF) approach. The DMF method of reconstruction does not require the model to have geometric symmetry and so performed efficiently to produce accurate strains. The BiSUP strain and

displacements were compared to those estimated by a 3D feature-based (FB) technique and a 2D+t HARP technique.

A computer-assisted Strain from Unwrapped Phase (caSUP) procedure to automatically place branch cuts was then devised. A combination of simulated annealing and exhaustive search methods were used to obtain the optimal branch cut configuration. The energy function that was minimized in the search methods aimed to maintain spatial and temporal continuity. This process reduced the manual intervention required to obtain 3D+t strain to nearly one-third of that of the GUI-based approach. The strain obtained was compared to 3D strain obtained from mSUP.

To summarize, these works included validation and detailed comparisons of strains, torsion and rotation parameters of both the LV and the RV in human subjects of different pathologies and morphologies.

Acknowledgments

I would like to take this opportunity to thank my advisor Dr. Thomas S. Denney Jr. I feel priveleged to have had the chance to work with him for the past few years. He has been both inspirational and immensely supportive to my work. He has given me ample freedom to explore my thoughts in my research, given ideas/suggestions when necessary and guided me through the various roadblocks I faced in my research. I will forever be grateful to him.

I would like to thank my advisory committee members, Dr. Stanley J. Reeves and Dr. Jitendra Tugnait for providing valuable suggestions at various times. I would also like to thank Dr. Amnon J. Meir for being the outside reader for my dissertation.

I would like to express my sincere gratitude to my labmates. The stimulating discussions and seminars we had certainly sparked plenty of ideas in my research. They have been both helpful and supportive, providing me with a great workplace atmosphere.

My friends and roommates have been great. They made moving to a new place, a daunting task in my mind, fun and easy. I will never forget the laughs, the parties, and the random sports and science discussions. They have been a part of some of the best memories of my life. Thank you. I would like to thank the cricket team for a lot of great moments, I really enjoyed the cameraderie and it was a privelege to be a part of the team.

Finally, I would like to thank my family for showering me with unconditional love and affection. This would not have been possible without your constant encouragment and moral support. I dedicate this dissertation to you.

Table of Contents

Abstract ii
Acknowledgments iv
List of Figures x
List of Tables xiv
1 Introduction 1
1.1 Structure and Functioning of the Heart 2
1.1.1 Structure of the Heart 2
1.1.2 Functioning of the Heart 3
1.1.3 Cardiovascular Diseases 5
1.2 Cardiac Imaging 7
1.2.1 MR Imaging 7
1.2.2 Cardiac Cine MR Imaging 9
1.2.3 Cardiac MR Tagging 9
1.3 Applications of Tagged MRI 13
1.3.1 Strain 13
1.3.2 Torsion 14
1.3.3 Applications 16
2 Tagged Image Analysis 17
2.1 Feature-based Methods 17
2.1.1 Segmentation 18
2.1.2 Tag Tracking 20
2.1.3 3D Motion Reconstruction 27
2.2 Harmonic Phase (HARP) MRI 31

2.2.1 HARP Refinement . . . 32
2.2.2 Extended HARP Tracking . . . 33
2.2.3 3D HARP . . . 36
2.3 Optical-Flow Methods . . . 39
2.4 Non-rigid Registration Techniques . . . 40
2.5 Conclusion . . . 41
3 Other MR Imaging Methods to Compute Myocardial Function . . . 43
3.1 3D Myocardial Tagging . . . 43
3.2 Slice Following HARP . . . 44
3.3 zHARP . . . 44
3.4 Combined Harmonic Phase and Strain Encoded MRI . . . 46
3.5 DENSE . . . 46
3.6 Conclusion . . . 50
4 Objectives . . . 51
5 Phase Unwrapping . . . 54
5.1 Introduction . . . 54
5.2 Two-dimensional Phase Unwrapping Terminology . . . 57
5.2.1 Residues . . . 57
5.2.2 Dipoles . . . 57
5.2.3 Branch Cuts . . . 57
5.2.4 Quality Maps and Masks . . . 58
5.3 Two-dimensional Phase-Unwrapping Algorithms . . . 59
5.3.1 Path-Following Algorithms . . . 59
5.3.2 Least-squares Methods . . . 63
5.4 Conclusion . . . 65
6 3D Left Ventricular Strain from Unwrapped Phase: A GUI-based approach . . . 67
6.1 Introduction . . . 67

6.2 Materials and Methods . . . 69
6.2.1 Human Subjects . . . 69
6.2.2 Data Acquisition . . . 69
6.2.3 Unwrapping HARP Phase . . . 69
6.2.4 Quality-Guided Phase Unwrapping . . . 71
6.2.5 Residues and Branch Cuts . . . 72
6.2.6 Demodulated HARP Phase . . . 76
6.2.7 Inter-frame Phase Consistency . . . 77
6.2.8 Motion and Strain Estimation . . . 78
6.3 Results . . . 81
6.3.1 Computation Time . . . 81
6.3.2 Quantitative Comparisons . . . 81
6.3.3 mSUP Strains in Normals and Patients . . . 84
6.4 Discussion . . . 85
7 Comparison Of 2D And 3D Torsion Measured From Tagged MRI . . . 88
7.1 Introduction . . . 88
7.2 Methods . . . 88
7.3 Results and Discussion . . . 89
7.4 Conclusion . . . 92
8 3D+t Bi-Ventricular Strain using Phase Unwrapped HARP . . . 93
8.1 Introduction . . . 93
8.2 Materials and Methods . . . 94
8.2.1 Human Subjects . . . 94
8.2.2 Materials . . . 95
8.2.3 Segmentation . . . 95
8.2.4 Displacement Estimation . . . 95
8.2.5 Strain Computation . . . 98

8.2.6 Validation Experiments . . . 98
8.3 Results . . . 99
8.3.1 Computation time . . . 99
8.3.2 Comparison of Displacement Estimates with FB Technique . . . 100
8.3.3 Comparison of End-Systolic Strains with Feature-Based Technique . . . 100
8.3.4 Comparison with HARP Strains . . . 101
8.4 Discussion . . . 107
9 Computer-Assisted Strain from Unwrapped Phase . . . 111
9.1 Introduction . . . 111
9.2 Materials and Methods . . . 112
9.2.1 Human Subjects . . . 112
9.2.2 Data Acquisition . . . 112
9.2.3 Phase Unwrapping . . . 113
9.2.4 Simulated Annealing . . . 114
9.2.5 caSUP . . . 116
9.2.6 Motion and Strain Estimation . . . 118
9.3 Experiments . . . 119
9.3.1 Computation Time . . . 119
9.3.2 Validation . . . 119
9.3.3 caSUP in Normals and Patients . . . 124
9.4 Discussion . . . 124
10 Torsion Hysteresis . . . 126
10.1 Introduction . . . 126
10.2 Magnetic Resonance Imaging . . . 127
10.3 Geometric analysis . . . 127
10.4 Torsional Deformation Analysis . . . 128
10.5 Torsional Hysteresis . . . 128

10.6 Results and Discussion 129
11 Conclusion and Future Work 134
Bibliography 136

List of Figures

1.1 The anterior view of the human heart. 4

1.2 The cardiac cycle. 5

1.3 LV Hypertrophy illustration. 7

1.4 Slice prescriptions in cardiac MR imaging. 10

1.5 Tag patterns illustration. 11

1.6 Illustration of tag planes. 12

1.7 Illustration of displacement measurement using tags. 12

1.8 Strain characterization in different coordinate systems. 14

1.9 AHA 17-segment model. 15

1.10 Depiction of basal and apical rotation in the LV. 16

2.1 Contour propagation illustration. 19

2.2 ML/MAP tag tracking results. 23

2.3 Coupled B-snake tracker. 24

2.4 Deformable B-solid. 25

2.5 Thin-plate spline 3D deformation grid. 26

2.6 Model tags. 27

2.7 HARP filtering illustration. 33

2.8 Refined HARP tracking. 34

2.9 Extended HARP tracking. 36

2.10 3D HARP - material mesh. 37

2.11 3D HARP - In-plane motion. 38

3.1 SF HARP illustration. 44

3.2 SF HARP Planes Illustration. 45

3.3 DENSE: flood-fill unwrapping. 49

3.4 DENSE: procedure illustration. 49

5.1 1D phase unwrapping. 55

5.2 The original MRI image and corresponding residues. 58

5.3 The effect of branch cuts on unwrapping. 62

5.4 Unwrapping using least-squares methods. 64

6.1 LV HARP illustration. 70

6.2 Placement of branch cuts in mSUP. 73

6.3 Phase unwrapping result from mSUP. 74

6.4 Demodulated HARP and mSUP. 76

6.5 Displacement vectors from mSUP. 79

6.6 Strain maps: mSUP vs. FB. 83

6.7 Torsion angle from mSUP in normals and patients. 85

7.1 3D vs. 2D rotation and torsion plots. 90

7.2 Peak mitral annulus displacement. 90

8.1 PHTN heart illustration. 94

8.2 Segmentation of heart for BiSUP. 96

8.3 Branch cut placement for BiSUP. 97

8.4 Strain maps: BiSUP vs. FB. 102

8.5 Bland-Altman and correlation plots in LV: BiSUP vs. FB. 103

8.6 Bland-Altman and correlation plots in RV: BiSUP vs. FB. 104

8.7 Strain over time plots: BiSUP vs. HARP. 106

8.8 Emin strain over time from BiSUP. 108

9.1 Possible branch cut configurations given the no. of residues. 114

9.2 Branch cut perturbation illustration. 117

9.3 Time taken for simulated annealing and exhaustive searches. 118

9.4 Bland-Altman and correlation plots: mSUP vs caSUP. 121

9.5 Strain maps: mSUP vs. caSUP. 122

9.6 Emin over time using caSUP. 123

10.1 Volume time curve for the 3 groups. 128

10.2 Torsion time curve for the 3 groups. 129

10.3 Schematic diagram for calculating torsional hysteresis. 130

10.4 Torsion Volume loops. 131

10.5 Torsion hysteresis data in 3 groups. 132

List of Tables

6.1 Displacement measurements: mSUP vs FB. 82

6.2 Strain comparison: mSUP vs. FB. 82

6.3 Strain comparison: mSUP vs. HARP. 84

7.1 Comparison of 3D and 2D rotation and torsion. 91

8.1 Displacement measurements: BiSUP vs. FB. 100

8.2 Strain Comparison: BiSUP vs. FB. 101

8.3 Strain comparison: BiSUP vs. HARP. 105

9.1 Strain comparison: mSUP vs caSUP. 124

Chapter 1

Introduction

Image processing has found a number of applications in medical imaging. It has been an essential tool for diagnostic purposes. It has been observed that geometric and mechanical properties of the heart are key parameters in the prediction of the condition of the heart and the efficacy of therapies. Magnetic resonance imaging (MRI) in particular has a lot of advantages over other modalities. First, it uses non-ionizing radiation, unlike CT or PET, and therefore has no known harmful effect on the body. Second, it has good image quality and provides for 3D imaging. Cine MRI captures slices of the heart at various angles that can then be put together to form a 3D geometric model. It is capable of providing a series of such images over the entire cycle of the heart. Most importantly, tagged MR imaging helps in calculating key mechanical properties of the heart. In addition, non-invasive analysis of cardiac motion is possible through MR imaging. It is, however, necessary that the image analysis be both efficient and accurate for the purpose of clinical use. In this dissertation, we are concerned with tracking cardiac tissue and modeling the deformation of the cardiac LV from tagged MR images.

This chapter starts off by introducing the structure and functioning of the heart. It is followed by an overview of cine MR imaging and tagged MR imaging. Chapter 2 reviews the current techniques in analysis of tagged MR images and in particular the harmonic phase method (HARP). Chapter 3 gives an overview of the latest techniques being developed for 3D imaging. Chapter 4 lists the objectives and contributions of the current research. Chapter 5 lists some of the common phase unwrapping algorithms that were implemented to test their performance on phase images from tagged MRI. Chapter 6 explains the formulation of a procedure to obtain 3D strain from tagged MR images by using a graphical user interface

(GUI) approach to the phase unwrapping problem (mSUP). Chapter 7 compares 2D (HARP strains) and 3D (mSUP) strains and explores the advantages of the obtained 3D strains. Chapter 8 extends the mSUP method to obtain strain in the right ventricle (BiSUP). Chapter 9 details a method (caSUP) to reduce the manual intervention involved in the mSUP method. In chapter 10, an explanation of the energy mechanics of the heart using commonly measured parameters is explored. Chapter 11 lists suggestions for future work.

1.1 Structure and Functioning of the Heart

1.1.1 Structure of the Heart

The heart is a hollow muscular organ situated between the lungs and the ribcage, and is surrounded by a fibrous sac called the pericardium [1], [2]. It is about the size of a fist and is located underneath the sternum.

The human heart consists of four chambers (Figure 1.1): two atria and two ventricles. The right side of the heart (the right atrium and the right ventricle) is in charge of circulation of blood through the lungs or pulmonary circulation. The left side (the left atrium and the left ventricle) is in charge of pumping blood to the rest of the body or systemic circulation. There are two sets of vessels connected to the heart: arteries and veins. There are two arteries connected to the heart: the aorta that takes oxygenated blood away from the left ventricle; and the pulmonary artery that takes deoxygenated blood from the right ventricle to the lungs. There are two sets of veins connected to the heart: the superior and inferior vena cavae return deoxygenated blood to the right atrium; and the pulmonary veins return oxygenated blood from the lungs to the left atrium.

The septum divides the right and left sides of the heart, preventing passage of blood from one side to the other. The heart has four valves: pulmonary, aortic, mitral and tricuspid, that allow for blood flow within the heart and throughout the body. Cusps are segments in the valve that regulate the blood flow. Valves are either bicuspid or tricuspid. The pulmonary valve guards the opening of the right ventricle to the pulmonary artery. The

aortic valve helps blood flow to the aorta from the left ventricle and prevents it from flowing back. The mitral and tricuspid valves regulate blood flow from the atria to the respective ventricles. They are connected to the ventricular walls through fibrous strands called chordae tendinae.The papillary muscles limit the movement of the two atrio-ventricular valves and prevent them from inverting.

The wall of the heart consists of three layers. The myocardium is the thick muscular layer of the heart responsible for the contraction and relaxation of the heart. To the outside of the myocardium is the epicardium, which consists mostly of tissue and fat. The inner lining of the heart is made of smooth membrane and is called the endocardium.

The cells that comprise cardiac muscle are called cardiomyocytes [3]. The cardiac myocyte is a specialized muscle cell that is approximately 25μ in diameter and about 100μ in length. The myocyte is composed of bundles of myofibrils that contain myofilaments. The myofibrils have distinct, repeating microanatomical units, termed sarcomeres, which represent the basic contractile units of the myocyte.

1.1.2 Functioning of the Heart

The heart contracts rhythmically to move blood throughout the body through the circulatory system. Each beat of the heart encompasses a cardiac cycle. A cardiac cycle consists of three phases: the atrial systole, the ventricular systole and the complete cardiac diastole. Figure 1.2 explains the complete cardiac cycle. Atrial systole involves contraction of atrial walls to pump blood to the ventricles. Ventricular systole involves contraction of ventricular walls to pump blood out to the aorta and the pulmonary arteries. The atrioventricular valves close, preventing blood flowing back to the atria, while the pulmonary and aortic valves open. The beating sound of the heart is from the opening and closing of these valves. The complete cardiac diastole involves relaxation of the entire heart. Blood fills up from the vena cavae and the pulmonary veins into the right and left atria respectively.

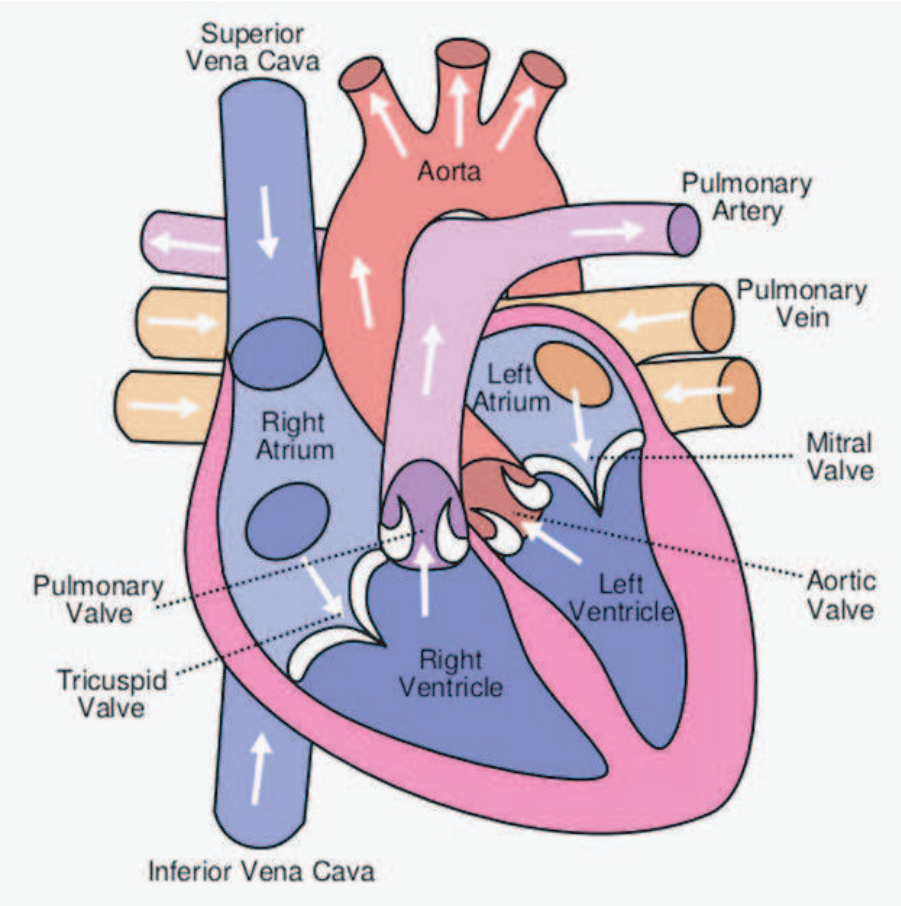

Figure 1.1: The anterior view of the human heart [4].

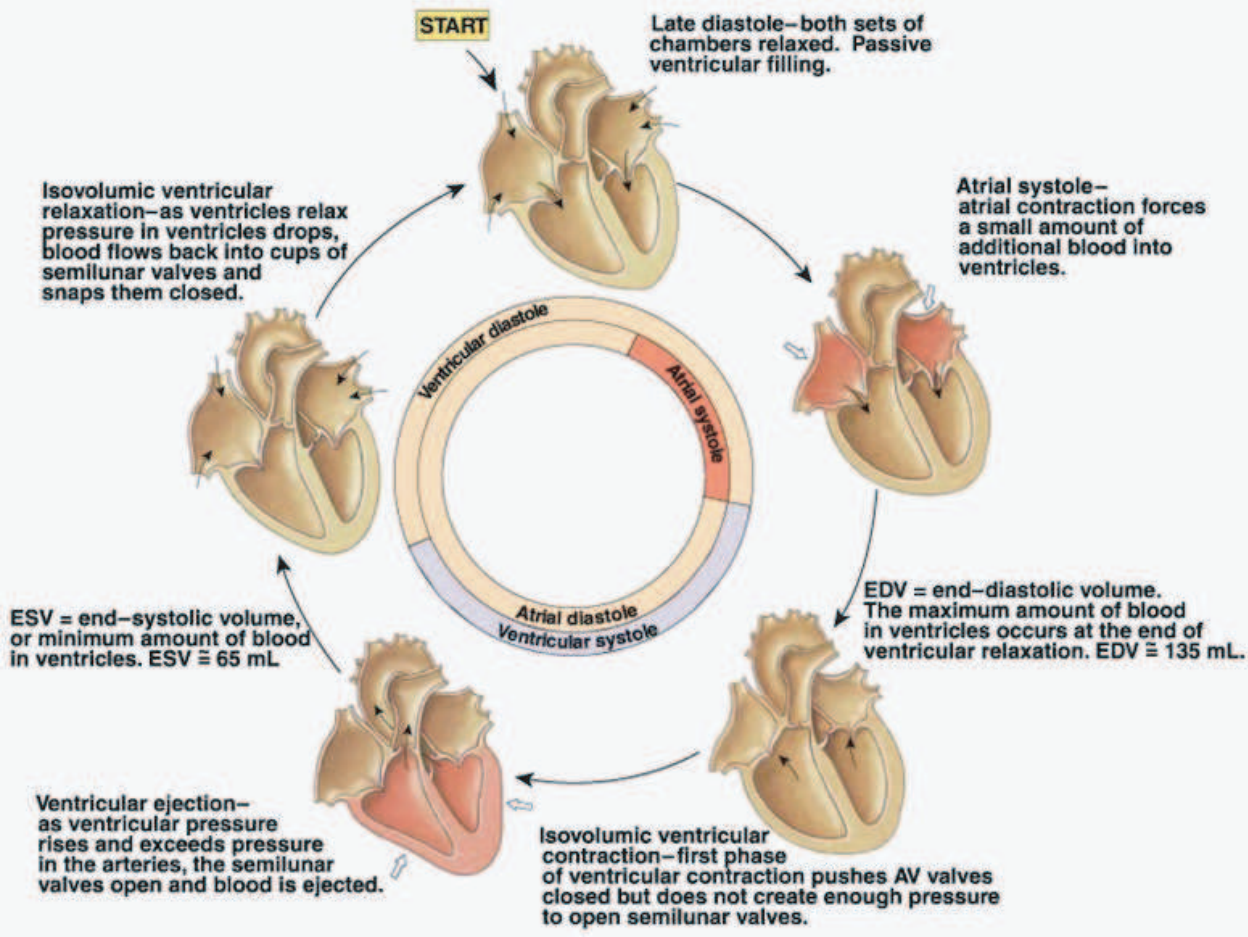

Figure 1.2: The cardiac cycle [2]. The arrows indicate the direction of blood flow.

The systematic and rhythmic beating of the heart is controlled by electrical impulses. These electrical impulses are provided by two electrical nodes: the sinoatrial node and the atrioventricular node. During diastole, there are no electrical signals traveling through the heart. The sinoatrial node sends out an electrical signal, which starts the contraction of atria leading to atrial systole. At the end of the atrial systole these signals reach the atrioventricular valve, which then triggers ventricular systole.

1.1.3 Cardiovascular Diseases

There are many diseases that affect the heart, but we shall now take a look at a few we presently study [5].

Ischemia is a restriction in blood supply, generally due to factors in the blood vessels, with resultant damage or dysfunction of tissue. Myocardial infarction is a disease state that occurs when blood supply to a part of the heart is interrupted or severely reduced. This happens when one of the coronary arteries is blocked. The blockage is caused by the building up of plaque inside the arteries; this is called atherosclerosis. When the plaque deposits disintegrate at once, a blood clot forms and blocks the flow of blood. This leads to a heart attack. By looking at strain maps, the area of infarction can be identified, and the progress observed.

Mitral regurgitation, also known as mitral insufficiency, is the abnormal leaking of blood through the mitral valve, from left ventricle into the left atrium. The mitral valve is composed of valve leaflets, the mitral valve annulus (which forms a ring around the valve leaflets), papillary muscles and chordae tendinae. A dysfunction of any of these can cause mitral regurgitation. Long-standing mitral regurgitation may show evidence of left atrial enlargement and left ventricular hypertrophy. Different phases of the disease show different symptoms.

Hypertension or High Blood Pressure is defined in an adult as a systolic pressure in excess of 140 mm Hg and/or a diastolic pressure in excess of 90 mm Hg. The heart has to work harder to maintain blood pressure, and thus, would be more prone to injuries. This leads to ventricular remodeling and other heart diseases. By studying the increase in volume of the heart, progress of the hypertensive heart can be monitored.

Ventricular remodeling refers to changes in size, shape and function of the heart after injury to the left ventricle. It might be because of any number of causes, acute myocardial infarction, chronic hypertension, and valvular heart diseases included. Left ventricular hypertrophy is the thickening of the myocardium of the left ventricle. There are two types of hypertrophy. Concentric hypertrophy is caused by increased systolic loads (pressure overload), leading to an increase in the mass of the chamber. Sarcomeres are added in parallel and the myofibers get fatter. Eccentric hypertrophy is caused by increased diastolic volume (volume overload), leading to an increase in myocardial mass. Sarcomeres increase in series

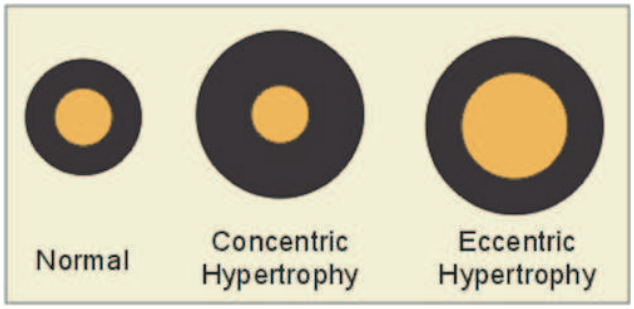

Figure 1.3: Illustration of the change in size and shape of the left ventricular wall for concentric and eccentric hypertrophy compared to normal heart [2].

and the myofibers get longer. The thickness of the affected chamber walls may be the same as in a healthy heart or thinner. An illustration of hypertrophy is shown in Figure 1.3.

Diabetes is a disease where the body does not produce enough insulin or when the insulin is not utilized properly (insulin resistance). Insulin resistance is associated with fatty buildups in arteries (atherosclerosis) and blood vessel disease, even before diabetes is diagnosed. Therefore, diabetes raises the risk of heart attacks and strokes.

1.2 Cardiac Imaging

Many imaging modalities like Computed Tomography (CT), Magnetic Resonance Imaging (MRI), X-rays, Echocardiography (ultrasound) can be used to image the heart, but we shall limit our discussion to cardiac MR imaging. This report concentrates on images obtained by the method described in Prince and Links [6]. As mentioned earlier, MRI provides many advantages over other imaging modalities and is especially useful for some applications. It is non-ionizing, non-invasive, allows for 3-D imaging and tagged MR imaging has the ability to measure tissue motion. We shall take a look at the basis for MR imaging and how cardiac MR imaging is performed in this section.

1.2.1 MR Imaging

Standard MRI is based on exciting the protons in hydrogen atoms. The tissues in the human body consist mostly of molecules of water and fat, which are the source of

hydrogen atoms. The protons possess a spin, and when a magnetic field B_0 is introduced, these spins align themselves with the main field. These spin at a frequency known as the Larmor frequency, $\omega = \gamma B_0$, which is proportional to the magnetic field applied. γ is the gyromagnetic ratio, which is 42.58 MHz/T for protons.

This magnetization is then excited by the application of a radio-frequency (RF) pulse such that it introduces a second magnetic field B_1 perpendicular to the main field. This field introduces a transverse magnetization vector, $M_{xy} = M_0 \sin(\alpha)$, orthogonal to the main field and a vector, $M_z = M_0 \cos(\alpha)$, parallel to it. M_0 is the initial equilibrium longitudinal magnetization, and $\alpha = \int \gamma B_1 dt$ is the flip angle. The proton precesses around the main field at the Larmor frequency and the rotating transverse signal produces a current in an RF coil placed near the signal. This is the signal measured by an MR scanner.

After the excitation, M_z recovers exponentially to M_0 with a rate constant of T_1, and M_{xy} decays exponentially with a rate constant of T_2. T_1 and T_2 are a result of spin-lattice and spin-spin interactions respectively. These parameters depend on the tissue and provide a source of contrast for imaging. If each region experiences a unique magnetic field, then we can image the position of the region. This is accomplished by spatially varying the magnetic field.

The second step of spatial localization is called phase encoding. A magnetic gradient field is applied briefly in one of the directions (y). As the change in frequency is very brief, when the gradient is switched off, it causes a change in phase that is proportional to the distance. The protons in the x direction have similar phase. The protons in the y direction have different phases. In a standard spin echo, the number of phase-encoding steps is equal to the number of lines in the matrix. Each step is performed with an incremental change in the strength of the phase-encoding gradient. The last step of spatial localization is frequency encoding, applied in the direction perpendicular to the phase-encoding direction (x). The precessional frequency of columns of nuclear spins varies in the direction of the frequency-encoding gradient. This gradient is applied during data acquisition.

The MR signal is a mix of all these frequencies (encoding in the frequency-encoding direction) and phase shifts (encoding in the phase-encoding direction). The Fourier Transform (FT) of the obtained signal gives describes the frequency spectrum. This is sampled for each row of the slice to obtain the entire Fourier space for the image. An inverse FT then yields the image. Back-projection techniques can be used when polar schemes are used to obtain the signals.

1.2.2 Cardiac Cine MR Imaging

The technique in Section 1.2.1 describes how to obtain cardiac images known as cine images. Generally, the images are obtained for an entire cardiac cycle. Images are obtained as a series of short-axis (SA) images that cut across the length of the heart, from the base to the apex. The left ventricle appears circular in these images. A long-axis (LA) slice would be orthogonal to the SA slices. It can be prescribed either as a set of radial slices, or as 2-chambered and 4-chambered LA images. Figure 1.4 illustrates how slices are prescribed. Cine images are used to measure parameters such as wall thickening, stroke volume, ejection fraction and wall thickness. In this research, we are concerned with the measurement of strain, for which tagged MR images are used. The next section discusses how MR tagging is done.

1.2.3 Cardiac MR Tagging

One of the major advantages of using MRI for cardiac imaging is that it can measure heart motion [8–10]. There are many ways for estimating heart motion using MRI, like phase contrast MRI (PCMRI), tagged MRI (TMRI) and displacement encoding with stimulated echoes (DENSE). In this dissertation, we are concerned only about extracting information from tagged MR images.

Tags or temporary fiducial markers that change with the underlying tissue can be placed in the image. The tag patterns can be of many types, but the two most popular ones are the

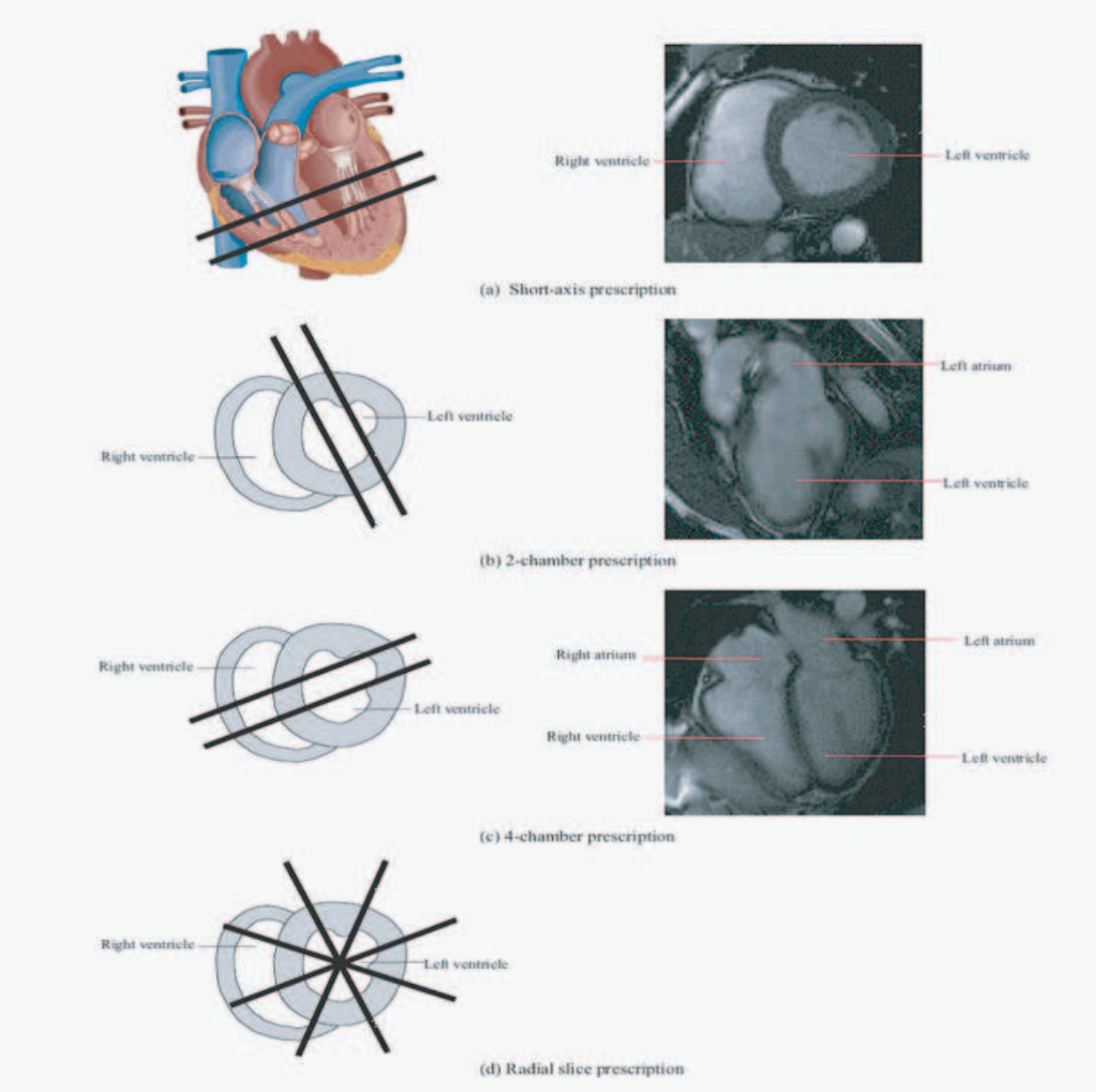

Figure 1.4: Slice prescriptions in cardiac MR imaging. Right: The slice prescriptions. The bold lines indicate the plane of the slices. Left: The corresponding cardiac MR images [7].

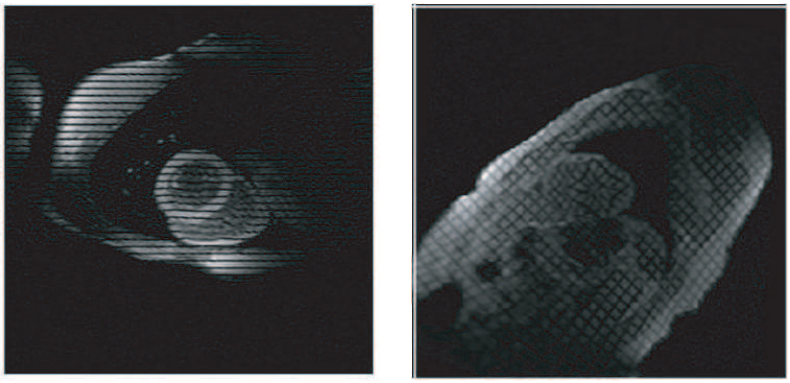

(a) (b)

Figure 1.5: A midventricular slice for two different tag patterns: parallel taglines (a) and grid tags (b).

parallel stripe pattern (Figure 1.5(a)), and the grid pattern with perpendicular tag planes (Figure 1.5(b)).

These tags are generated by a procedure known as SPAtial Modulation of Magnetization (SPAMM) tagging procedure [11]. Tags are created by dephasing the magnetizing gradient by the application of a spoiler gradient perpendicular to the tags. The tags are introduced at the initial time frame, usually at end-diastole, and are tracked for an entire cycle. The tags fade over time due to T_1 relaxation. The tags cut across as planes across the entire cross-section of the slice, and the planes deform with time as shown in Figure 1.6.

The tags are encoded onto the tissue and can be considered as material points. They are a measure of the displacement of the underlying tissue [12]. Tags, though, can measure displacement only in the direction perpendicular to them as shown in Figure 1.7. To obtain a 3D displacement field, tags in three orthogonal directions are required [13]. In the next chapter, a discussion of the present methods for extracting information from tagged images is presented.

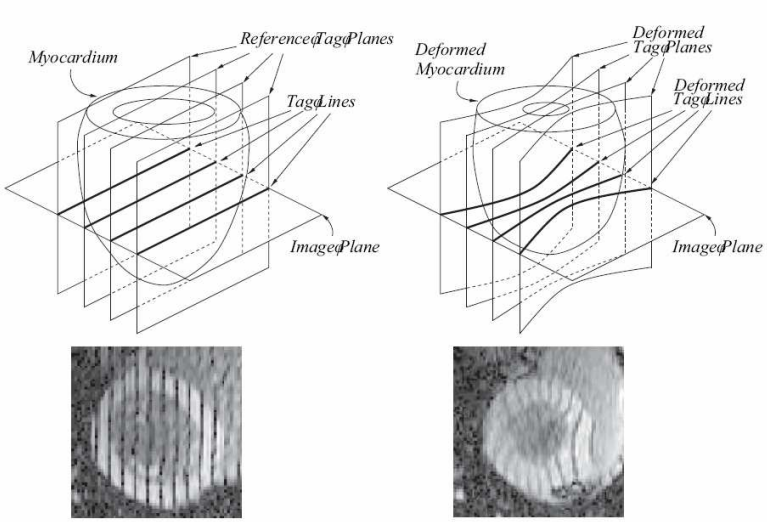

Figure 1.6: Illustration of tag planes [7]. Left: Tag planes introduced at end-diastole. Right: Deformation of the planes observed at end-systole.

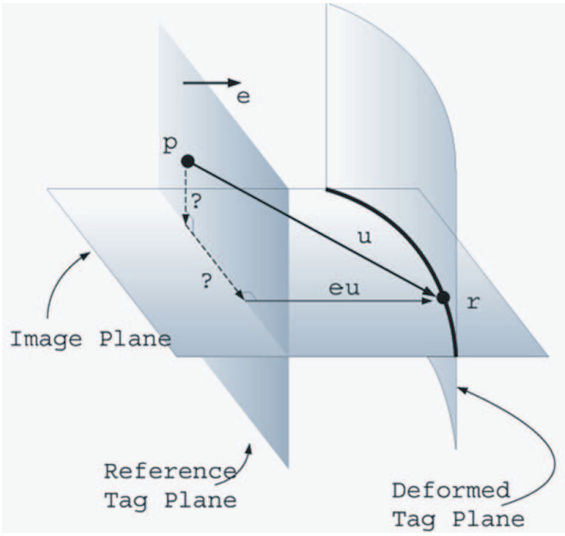

Figure 1.7: Illustration of displacement measurement using tags [14]. As observed in the figure, the point r originates from point p but the only displacement in the direction perpendicular to the tag plane can be measured.

1.3 Applications of Tagged MRI

Tagged MRI facilitates the capture of regional function of the heart [15,16]. Measures of function can be obtained transmurally, at several levels between the base and the apex, and along the different segments of the heart wall. These measures of function include strain, strain rate, shear, rotation and torsion.

1.3.1 Strain

Strain defines the amount of stretch or compression along a material line or elements of fibers, i.e. normal strain, and the amount of distortion associated with the sliding of plane layers over each other, i.e. shear strain [17]. Strain, in general depends on the particular direction being considered. During systole, typically, the heart wall may be thickening in the radial direction, leading to increased radial strain (E_{rr}), and simultaneously shortening in the circumferential and longitudinal directions, leading to decreased strains (E_{cc} and E_{ll} respectively). Also, the angle between two material directions in the wall will generally change due to shear strains (E_{cl}, E_{rl}, E_{cl}). Figure 1.8 shows the three normal strains and three shear strains usually measured for a given 3D displacement field [18]. Strain can also be characterized in a direction based on the orientation of fibers in the heart. Figure 1.8 illustrates both the above characterizations. Alternatively, strain can also be characterized in a coordinated system-independent way through the corresponding eigenvectors and eigenvalues. This way of characterization gives maximal stretching (E_{max}) and shortening (E_{min}) strains. The time derivative of the strain gives the strain rate.

The LV is segmented to represent the obtained regional strains in an arrangement that makes it easy to compare the results in different conditions or between patients. Figure 1.9 illustrate the segmentation in more detail.

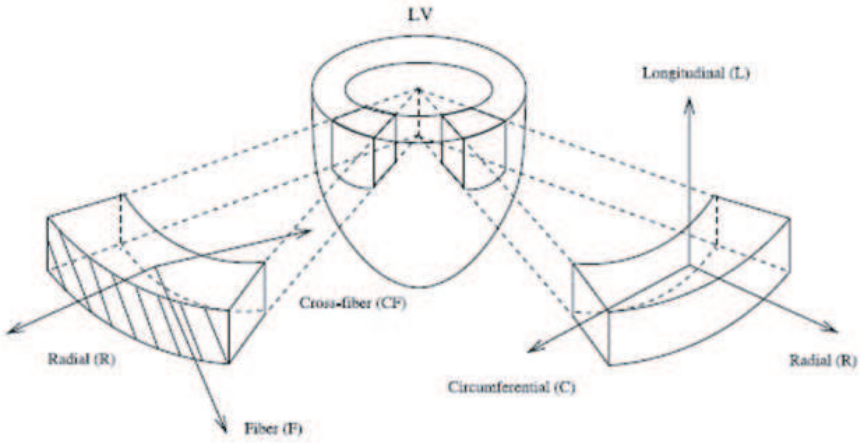

Figure 1.8: Strain characterization in two different coordinate systems [18].

1.3.2 Torsion

Torsion measures the twisting of an object due to an applied torque. The LV undergoes a wringing motion to pump blood during systole, and subsequently, has torsion associated with it. Figure 1.10 illustrates the measurement of torsion in LV. The apex and the base both undergo rotation with respect to their position at end-diastole; the difference between these rotational components gives the torsion. Twist is the ratio of the measured torsion and the distance between the apex and base.

Torsion has been traditionally computed in a 2D sense. A basal and an apical slice are captured using tagged MRI. The points are then tracked through the time frames using either one of the mesh tracking methods [20–22] or the HARP method [23]. The rotation is calculated in each of the two slices through the cycle. The difference in the rotational components between the apex and the base gives the desired torsion measurement.

2D torsion measurements can be erroneous because there usually is a longitudinal shortening of the LV which results in a change in the position of the basal slice through the cycle. As a result, 3D methods to compute the true torsion have been proposed [24–27].

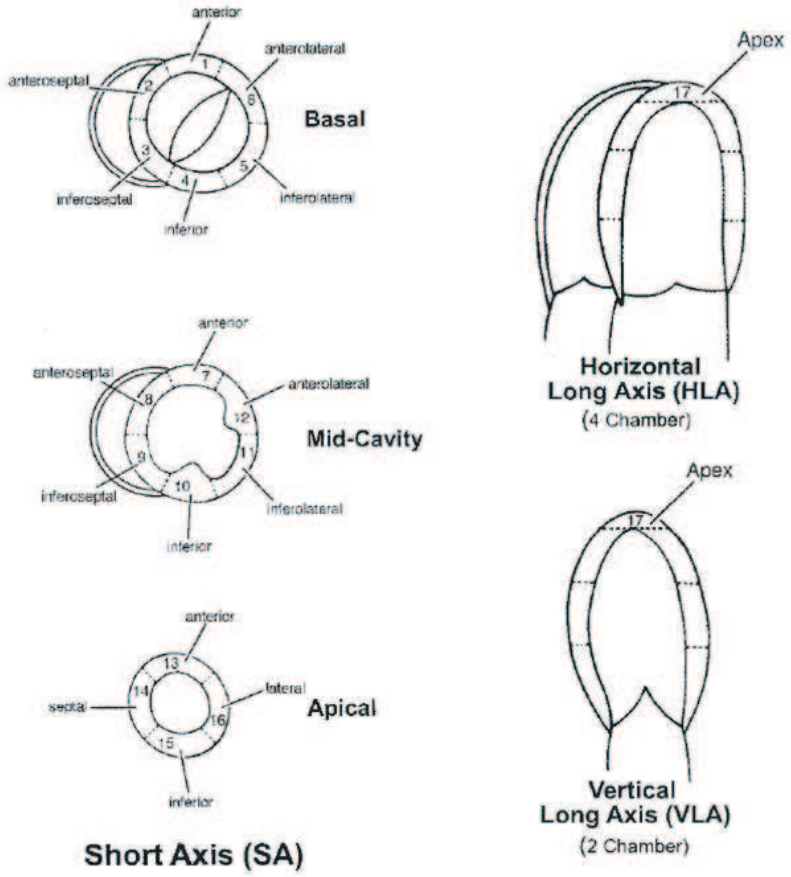

Figure 1.9: The muscle and cavity of the left ventricle can be divided into a variable number of segments [19]. Based on autopsy data the AHA recommends a division into 17 segments for the regional analysis of left ventricular function or myocardial perfusion. The left ventricle is divided into equal thirds perpendicular to the long axis of the heart. This generates three circular sections of the left ventricle: basal, mid-cavity, and apical. Only slices containing myocardium in all 360^o are included. The basal part is divided into six segments of 60^o each. Similarly the mid-cavity part is divided into six $60^o segments$. Only four segments of 90^o each are used for the apex because of the myocardial tapering. The apical cap represents the true muscle at the extreme tip of the ventricle where there is no longer cavity present.

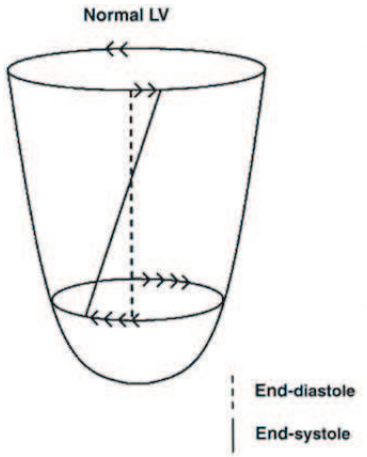

Figure 1.10: Schematic depiction of basal and apical rotation during systole in the normal LV [23]. Arrowheads indicate the direction and magnitude of rotation.

1.3.3 Applications

The regional measures of function help us better understand the normal functioning of the heart [15, 28–30]. The normal motion of the heart is complex and encompasses regional non-uniformities. The differences in the measures of function are not only time-dependent, but also transmural. They can also be used as a means to characterize different cardiovascular diseases such as valve disease [31], hypertension [32], myocardial infarction [33] and cardiomyopathy [34–37].

It has been observed that in patients with mitral regurgitation, the rate of untwisting in early-diastole reduces when compared to normal volunteers [31, 38]. Patients with hypertension tend to have hearts that experience higher amount of torsion [39] and nonuniform circumferential shortening [32] to compensate for the increased blood pressure. Infarcted areas of the myocardium tend to experience lower strains than normal myocardial tissue [33]. The effect of age, sex and size on the functioning of the heart has also been studied using tagged MRI [18, 40]. As a clinical tool, tagged MRI provides a detailed functional and quantitative assessment of the function of the heart.

Chapter 2

Tagged Image Analysis

Tagged MR images provide the ability to track tissue in the heart. Tracking the heart tissue helps us derive regional parameters such as strain, and torsion. Tagged image analysis is the process of extraction of this information from tagged MR images.

Tag tracking involves extracting displacement estimates from the tag lines in the image. Various methods have been proposed for this procedure. We shall take a look at a few of the most widely used methods — optical flow-based methods [41–43], feature-based data extraction methods [14, 44–47] and the harmonic phase (HARP) based methods [27, 48–52].

This procedure is complicated because of the complex and nonuniform motion of the heart, the through-plane motion (i.e. the movement of the base of the heart towards the apex as the heart contracts), the fading of the tag lines through the cardiac cycle, and various artifacts found in images due to incorrect imaging. It is important that the process be quick and accurate and involve the least amount of manual intervention, in spite of the difficulties, to be clinically viable. In this chapter, each procedure is further discussed.

2.1 Feature-based Methods

Tagged image analysis using feature-based methods involves three steps:

1. Segmentation of the myocardium.
2. Tag tracking.
3. 3D motion reconstruction.

2.1.1 Segmentation

Delineating the endocardial and epicardial boundaries of the heart is important for a number of reasons. Firstly, from the myocardial boundary contours, global functional parameters such as ejection fraction, volume, mass, etc, can be computed. Secondly, regional myocardial functional parameters are computed in segments within the myocardial boundaries. The 17-segment AHA model is normally used for this purpose. Thirdly, data outside the myocardium is generally noisy and may interfere in tracking of points within the heart wall in most techniques. Finally, the contour data helps in registration of the SA and LA images, and eventually, in the development of the 3D deformation model.

Automatic methods for myocardial segmentation in tagged images have to overcome problems of high noise, intensity inhomogeneities and complex backgrounds. Morphological image processing [44, 53] was first used for automated tagged MR myocardial segmentation. It involves a morphological closing operation to remove the tag lines found in the tissue, before using intensity-based thresholding. Markov random fields [45, 54] have been used too. These methods involve the modeling of the background tissue, tagged tissue and the myocardial tissue as random variables and then using a MAP decision rule to identify the myocardial boundaries. Gabor filter [55] based methods involve the removal of the tag lines using Gabor filters and using deformable models to obtain the final segmentation. These methods though are not adequately accurate.

Manual input is normally used to segment the myocardium in at least one image of the sequence. This is normally the end-diastolic time-frame image. This contour is then propagated to the rest of the image sequence using deformable models [56, 57] and non-rigid registration [58]. Once the myocardial boundaries have been segmented, the next procedure is tag tracking.

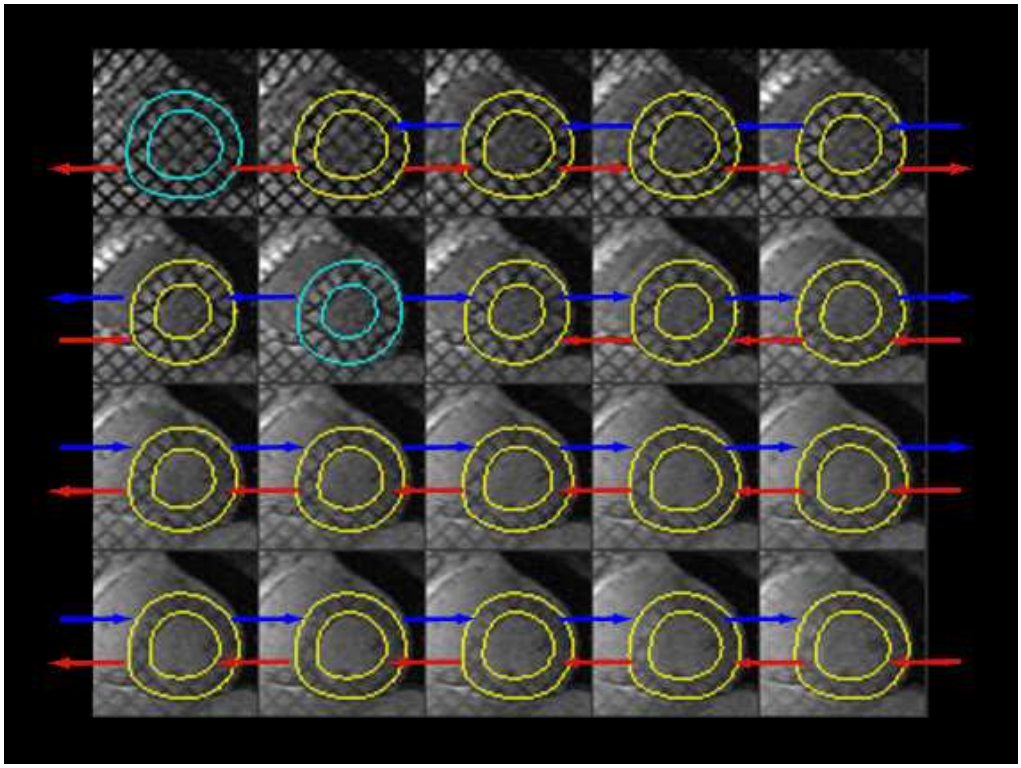

Figure 2.1: A result of myocardial segmentation in a SA slice through the cycle. The contours at ED and ES were manually drawn and then propagated using non-rigid registration.

2.1.2 Tag Tracking

This method involves the use of tag lines as dark intensity lines. To reconstruct motion, the tag lines are to be tracked over time. In most methods, tag lines are detected either manually or semi-automatically [59]. The tags for image frames are obtained by matching a template of the tags obtained in the previous time or a user-defined template for the most probable tags. The tag lines themselves can be detected using various ways — template matching [44] and filters [46,54,60,61]. Methods that do not require user-defined myocardial contours [45] have also been suggested. Once the displacement vectors are obtained for the tag lines, data is interpolated to obtain the full-field displacement data. The major disadvantage in these methods is that interpolation is required to obtain a dense displacement field. Manual intervention to correct the tracked tag lines is often required.

Template Matching

Guttman et al. used morphological image processing [44] to detect tag lines in radial tagged images. The first step is the detection of myocardial boundaries detected after processing a morphologically closed image to remove the tags. The tag lines are next detected in the initial image of the sequence. To detect the tags in the next image of the sequence, an a priori position is first determined based on the expected rotation and the previous position of the tags. A search window is then devised around the determined a priori point to find a point in the image with a tag profile closest to the tag profile of the applied tag lines. This method of tag tracking is a very basic method; more complicated and accurate algorithms have since been developed.

ML/MAP Estimation of Tag Lines

Denney explained a procedure for automated tag identification and tracking in [45]. This technique does not require user-defined segmentation of the myocardium. The user needs to specify a region of interest (ROI) enclosing the myocardium at the first time frame.

The tags at the first image are obtained from the imaging parameters. This method, called the ML/MAP method, consists of three stages.

First, a set of candidate tag line centers are estimated across the entire region of interest (ROI) with a snake algorithm. The initial snake is determined based on tags from the previous time frame. This snake is then deformed to minimize an energy function consisting of four terms:

$$\begin{aligned} E(\mu_j) = \sum_{i=0}^{N_c-1} [\varsigma_{ij} L(\mu_{ij}, w_{ij}) \\ + \gamma_{ij} E_{sep}(\mu_{ij+1} - \mu_{ij}) + \gamma_{ij} E_s ep(\mu_{ij} - \mu_{ij-1})] \\ + E_{stretch}(v_j) + E_{bend}(v_j). \end{aligned} \tag{2.1}$$

The first term consists of image forces applied to each snake point determined from a maximum likelihood (ML) estimate of the tag center μ. μ_{ij} is the i^{th} tag center on the j^{th} tag line. N_c is the number of centers in each tag line. w is a set of image pixels along a line perpendicular to the tag line. $L(\mu_{ij}, w_{ij})$ is the log-likelihood function that is to be minimized to match the template of the estimated tag center with the expected tag template. This forces the snake to converge to the dark intensity lines in the image. ς_{ij} is a normalizing function that prevents the weight of the first term in the overall function from being too large.

The second term enforces a constraint to maintain separation between adjacent tag lines.

$$E_{sep}(x) = \begin{cases} 0, & \text{for } x \geq d_{sep} \\ \frac{1}{2}(d_{sep} - x)^2, & \text{for } x < d_{sep} \end{cases} \tag{2.2}$$

where d_{sep} is the minimum distance between tag points. γ_{ij} is the weght of the separation constraint and is set to zero if μ_{ij} is outside the myocardium.

The third and fourth terms are constraints on the snake to control the stretching and bending of the snake. v_j is the displacement of the tag line μ_j from its initial undeformed position p_j such that $\mu_j = p_j + v_j$.

After optimization, the tag centers for the present time frame are obtained. Once the tag centers in the ROI are obtained, next it is determined if the tag center is in the myocardium or not. The tag center estimation algorithm above is not completely accurate, which may lead to points in the myocardium that are not part of the tag tissue to be a candidate tag center. Two MAP tests are applied to test if the tag centers are part of a tag line. Three mutually exclusive hypotheses are considered:

- Hypothesis T: The neighborhood contains tagged myocardium. The signal model under hypothesis T depends on the tag pattern, proton density, T_1, T_2, the imaging protocol and noise.

- Hypothesis M: The neighborhood contains untagged bright tissue (presumably, but not necessarily myocardium). The signal model under hypothesis B depends on signal samples of the myocardium and noise.

- Hypothesis B: The tissue contains untagged dark tissue such as saturated blood (in black blood images) and air. The signal model under hypothesis B depends on signal samples of tissue outside the myocardium and noise.

In the first MAP test, a candidate tag centre is considered to be part of the myocardium if it is more likely to be part of a tag line (H_T) or in untagged myocardium (H_M) than in the background tissue (H_B). In the second MAP test, a candidate tag centre is considered to be part of a tag line if it is more likely to be part of a tag line (H_T) than in untagged myocardium (H_M) or in the background tissue (H_B). In the final step, a pruning algorithm is used to remove small, isolated clusters of points that appear and disappear with time. This pruning step removes points that are not persistently tagged and isolated tag points created as a result of noise in the image.

A pre-processing step of computing image statistics necessary for the ML/MAP method is performed. Parameters such as noise variance and mean and noise of the background pixels

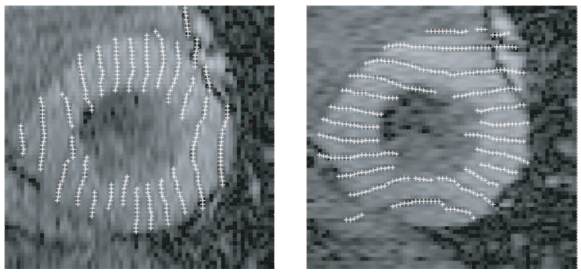

(a) (b)

Figure 2.2: Results of the ML/MAP tag tracking algorithm for a midventricular slice for two different tag angles (0 and 90 degrees) [45].

and myocardium pixels were calculated. Figures 2.2(a) and 2.2(b) show the results of the ML/MAP estimator for two different tag angles for a mid-ventricular slice.

Combined Tag Tracking and Strain Reconstruction

In [47], a method for computing three-dimensional (3D) myocardial strain from tagged cardiac magnetic resonance (MR) images called the COmbined Tag Tracking and strain (E) Reconstruction (COTTER) algorithm is presented. This algorithm fits a deformation model directly to the image data, thus combining the tag tracking and deformation reconstruction into one step. The deformation model ensures that the tag lines identified in the image data are consistent from slice to slice. The initial geometry of the deformation model is determined from user-selected, end-diastolic elliptical regions of interest (ROI). The COTTER algorithm then optimizes the control points of the cylindrical B-spline model so that tag planes deformed by the model match the tag lines in the image data. The myocardium motion field and strains can be reconstructed directly from the results of the combined tag tracking procedure without intermediate steps, such as inverse and forward motion field fitting.

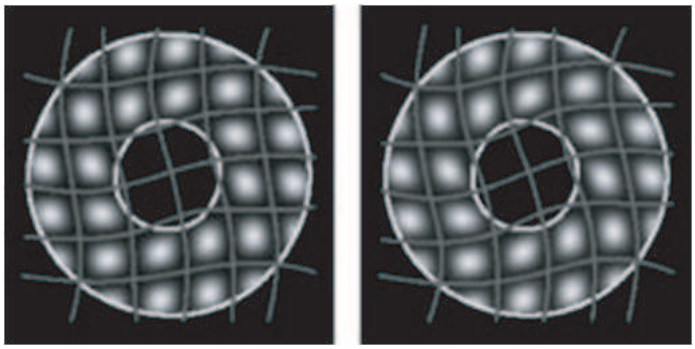

Figure 2.3: Results of couple B-snake tracker on a simulated image sequence [63].

Analysis of Tagged MR Cardiac Images with B-splines

In [62], tag lines are tracked with dynamically programmed B-snakes. Oriented tag templates were first constructed by simulating the MR imaging process. The templates are subsequently correlated with the image data, giving rise to an energy landscape, which is optimized over with dynamic programming. Tracking the valleys of the energy landscape with snakes allows for measurement of MR tag deformations due to tissue motion.

In [63, 64], coupled B-snake grids and constrained thin-plate splines are used for analysis of 2-D tissue deformations. Coupled snake grids are a sequence of spatially ordered deformable curves represented by B-spline bases, which respond to image forces, and track non-rigid tissue deformations from SPAMM data. The spline grids are constructed by having the horizontal and vertical grid lines share control points. By moving a spline control point, the corresponding vertical and horizontal snakes deform. This representation involves shared control points. B-spline bases provide local control of shape, compact representation, and parametric continuity. Efficient spline warps are proposed which warp an area in the plane such that two embedded snake grids obtained from two tagged frames are brought into registration, interpolating a dense displacement vector field. The reconstructed vector field adheres to the known displacement information at the intersections, forces corresponding snakes to be warped into one another, and for all other points in the plane, where no information is available, a C^1 continuous vector field is interpolated (thin-plate splines).

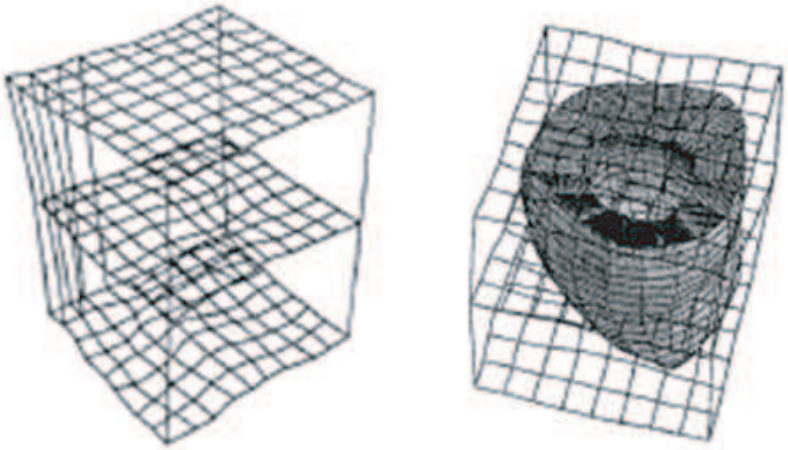

(a) (b)

Figure 2.4: (a) Tag grids formed from implicit snakes determine a B-solid. (b) Heart volumetric model located in a B-solid [65].

In [65], an approach for 3D tag localization and tracking of SPAMM data by a deformable B-solid is described. The solid is designed in terms of a 3D tensor product B-spline. The isoparametric curves of the B-spline solid (termed implicit snakes) deform under image forces from tag lines in different image slices. The localization and tracking of tag lines is performed under constraints of continuity and smoothness of the B-solid. The framework unifies the problems of localization, and displacement fitting and interpolation into the same procedure utilizing B-spline bases for interpolation. To track motion from boundaries and restrict image forces to the myocardium, a volumetric model is employed as a pair of coupled endocardial and epicardial B-spline surfaces. To recover deformations in the LV, an energy-minimization strategy is used where both tag and LV boundary data are used.

In [66], tags are tracked using surfaces represented by thin-plate splines. These surfaces represent tags in one direction and are obtained using a stochastic optimality criterion. These surfaces are estimated using tags in both past and present images maintaining temporal continuity (temporal filter). A continuous representation of each tag surface is also maintained

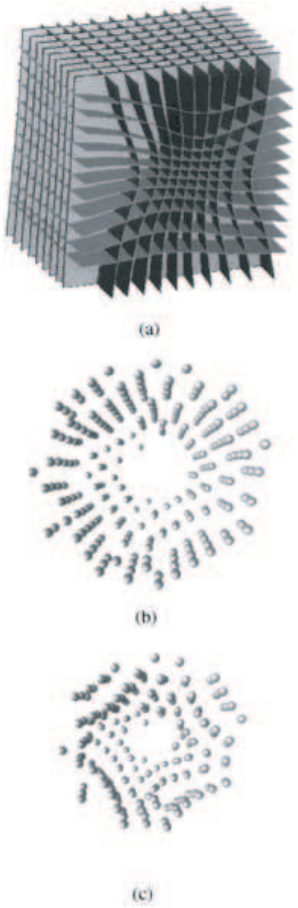

Figure 2.5: (a) 3 sets of tag surfaces are assembled into a deforming 3D grid; (b) the intersections of the grid within the LV wall mark material points of tissue (c) these markers move with the tissue, depicting 3D contraction [66].

(spatial filter). The method generates a continuous three-dimensional reconstruction of deformed tag planes. Tag plane movement is modeled as a time update process, where each update consists of a quadratic component that describes the bulk motion of the tag planes plus a stochastic component that characterizes the fine-scale variation in the motion.

Model Tags

A method is described for the reconstruction of 3-D heart wall motion directly from tagged magnetic resonance images, without prior identification of ventricular boundaries or tag stripe locations in [67, 68]. The method utilizes a finite-element model to describe the shape and motion of the heart. Initially, the model geometry is determined at the time of

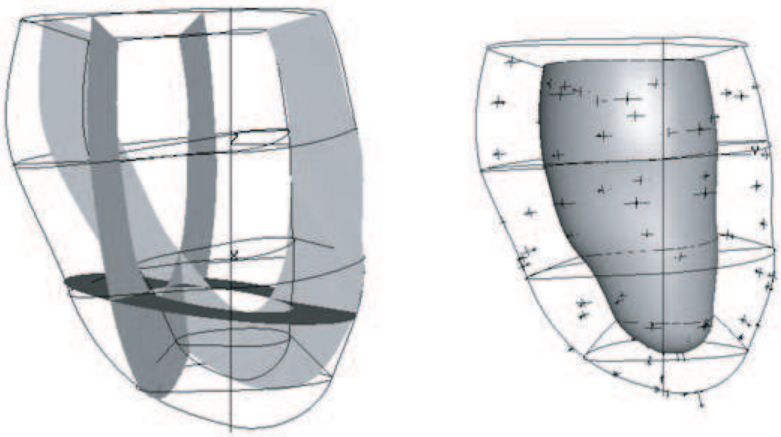

(a) (b)

Figure 2.6: (a) Model tags at the time of creation [67]. The two lighter tags are from short-axis images while the dark tag is from a long-axis image. (b) Model fit to guide points at ED [67]. Endocardial surface shaded, guided data as +. Corresponding model locations (joined to each guide point with a line) are shown with cross-hairs.

tag creation by fitting a small number of guide points which are placed interactively on the images. Model tags are then created within the model as material surfaces which define the location of the image tags. An objective function is derived to measure the degree of match between the model tags and the image stripes. The objective is minimized by allowing the model to deform directly under the influence of the images, utilizing an efficient method for calculating image-derived motion constraints. The model deformation can also be manipulated interactively by guide points.

2.1.3 3D Motion Reconstruction

Once the myocardium has been segmented and the points tracked, the 2D motion vectors are combined to obtain a 3D deformation field. The most common method involves fitting a model to the calculated 2D displacement estimates. This method also involves optimization and smoothing of the deformation field, for both interpolating missing data points and to compensate for erroneously tracked points. Many 3-D LV deformation models have been

proposed, including methods based on prolate-spheroidal basis functions [69], finite elements [67], finite differences , free-form deformations [70, 71], and B-spline functions [47, 65, 72–74]. Combined tag tracking and deformation field fitting algorithms have been proposed that fit the deformation field directly to the image data [47, 54]. This alleviates the need for smoothing, but this method is sensitive to registration errors between slices.

TEA: Tag Strain(E) Analysis

For the 3D reconstruction of the displacement field, a series expansion is expressed in a dimensionless prolate spheroidal coordinate system $[\lambda^*, \varphi, \theta]$. λ^* represents wall depth and has values of zero at mid-wall, -0.5 at the endocardial surface, and 0.5 at the epicardial surface. φ, θ represent azimuthal and circumferential angles, respectively. Displacement $\delta\lambda$ in the radial coordinate direction can be represented using associated Legendre polynomial functions and $a_{r,l,m}$, the unknown coefficients. The number of terms included in the series expression is given by the parameters n_r and n_l. Similar expressions are used to model the angular displacement in the longitudinal and circumferential directions, $\delta\varphi$ and $\delta\theta$. The measured displacements in X, Y and Z directions are projected onto the local prolate spheroidal coordinate unit vectors, and the $\delta\lambda$, $\delta\varphi$ and $\delta\theta$ series coefficients are determined simultaneously. The backward displacement field is inverted at the points where the strain is computed using a gradient descent approach. Iterations are stopped when an arbitrary precision is reached. The fit to the prolate spheroidal coordinate-based model is preceded by a correction for the bulk motions of the ventricle. This is necessary because the origin and long axis of the prolate spheroidal coordinate system are singularity points which should be kept out of the myocardium. This 3D kinematic model functions to interpolate the myocardial motion between samples in space, to filter out noise in the sampled data and to facilitate the computation of the local displacement gradients used for strain calculation.

DMF: Discrete Model-Free

The discrete model-free (DMF) algorithm [14] uses finite-difference analysis to reconstruct displacement and strain from tag lines and user-defined myocardial contours. For each imaged time frame, the DMF first constructs a 3D segmentation of the LV wall on a regularly spaced discrete grid of points from the user-defined endocardial and epicardial contours. The grid spacing is equal to the pixel size in the MR image. A displacement vector is estimated for each grid point in the LV segmentation that maps the grid point back to its end-diastolic position. The displacement vectors to be estimated at a certain time are obtained from the one-dimensional constraints obtained from the tag line data. Since the grid spacing is small compared with the tag line spacing, there are many more unknown displacement vectors than tag line constraints, and a smoothness constraint is required. The smoothness constraint minimizes the spatial variation of the displacement field. This is imposed by setting the differences between pairs of displacement vectors on the spatial point grid equal to zero-mean random variables. The linear minimum mean-square estimate from the tag line and smoothness constraints is then obtained by solving a system of equations containing a sum of the two constraints. A weighting parameter controls the resulting smoothness and the spatial resolution of the reconstructed displacement field. Strain is computed by first converting the reconstructed displacement field to material coordinates using linear interpolation. The displacement gradient is then computed using a finite-difference derivative approximation averaged over a $3 \times 3 \times 3$ point neighborhood. Finally, the Lagrangian strain tensor is computed from the displacement gradient.

TTT: Tag Tissue Tracking

Initially, for each short axis image plane, time frame and short-axis tag stack, a two-dimensional B-spline field is formulated to approximate the one-dimensional displacement of a tag surface. Once displacement fields of both tag stacks at a given short-axis image plane and time frame are calculated, two components of the past total trajectory of any tag

point can be determined. The final inverse motion field gives for each point the 3D vector pointing to its reference material point at the undeformed state. The missing component, the SA through-plane motion, is computed from LA images as follows: (a) a 2D B0-spline field is fit for the displacement on each long-axis imaging plane; (b) this parametric field is then evaluated at each SA image plane intersection line; (c) through-plane displacement information coming from all LA images is used to fit a second field in each SA plane. The same region of interest in both SA tag displacement field fitting and the last step of long-axis analysis is used, and a single formula for a B-spline inverse deformation field is defined. The forward deformation at the corresponding point at tagging time should be the inverse. The forward deformation is also formulated as a three-dimensional B-spline tensor product for a given time frame. After the 3D forward deformation field is constructed for each time frame, a 1D time smoothing is performed on control points. The motion of the heart is then described as a four-dimensional B-spline forward motion field.

FTEA: Four-D Tag Strain(E) Analysis

The backward transformations deform a point x onto a point for which the coordinates are defined as a tensor product of B-spline curves, as for the B-solid defined in [65] or for the forward transformation in TTT. The transformation is estimated by minimizing a criterion which is the weighted sum of a data term, which is the sum of squared distances of each deformed tag points from its tagging plane, and a smoothing term, which is the integral of the square of the second derivatives of the backward transformations. The criterion is minimized with a conjugate gradient method. The transformations are estimated sequentially, using the deformation field at the previous time as the initial transformation for the conjugate gradient. With all the backward transformations obtained, a 4D planispheric transformation is computed. Displacements in the planispheric coordinates can be defined using a B-spline tensor product in time and space. To compute the forward transformation at a particular time, a least-squares criterion is estimated that minimizes the difference in the distance

between a tag point position and its position after performing the corresponding backward and forward transformations at that point.

Summary

These methods were found to yield noticeable differences in the displacement and strain [13]. DMF uses the least smoothing and was found to have the highest spatial resolution, but it was also the most noise sensitive. FTEA uses the most smoothing and hence was least noise sensitive but had the lowest spatial resolution. The TEA and TTT methods were found to fall somewhere in the middle. It was also found that all the methods produced strain maps that were useful for characterizing myocardial function with high precision. The method chosen thus is a trade off between smoothing and noise sensitivity.

2.2 Harmonic Phase (HARP) MRI

HARP analysis concentrates on the Fourier transform of tagged MR images. Figure 2.7(a) shows a grid-tagged MR image and its Fourier transform (Figure 2.7(b)). One DC peak at the center of Fourier space, and the harmonic spectral peaks can be seen in Figure 2.7(b). A bandpass filter is applied to isolate a spectral peak, which can be identified by the index k. The inverse Fourier transform of the k^{th} peak produces the complex image

$$I_k(y,t) = D_k(y,t)e^{j\phi_k(y,t)} \tag{2.3}$$

where y is the location of a pixel on the image plane, t is the time sampled in discrete steps and corresponding to one of the time frames, D_k is called the harmonic magnitude image, and ϕ_k is called the harmonic phase image. Since phase angles can only be measured modulo 2π, however, only a "'wrapped"' value of harmonic phase in the range of $[-\pi, \pi]$ can

be obtained, which can be denoted as

$$\psi_k(y,t) = W(\phi_k(y,t)) \tag{2.4}$$

where W is a nonlinear wrapping function and ψ is the HARP angle image. The HARP angle image is shown in Figure 2.7(c). The main properties of the HARP image are:

- The locations of the wrapping transitions on the HARP angle image are closely coincident with the locations of the tag lines during myocardial motion.
- The phase values on the HARP image are dense, providing more information than just the locations of tags lines.
- The phase value of a material point is fixed from the tagging instant and does not change, i.e., the HARP value is a material property of the underlying tagged tissue. This phase invariance property is the basis of HARP tracking [27, 49, 75]. The slope of the phase is used to compute the local tissue strain [50, 76, 77].

Due to the fact that the phase is wrapped, an assumption of small motion between two adjacent time frames is needed to guarantee that the points can be uniquely associated. In particular, if a point has a displacement of greater than one-half tag spacing in any of the tag directions, HARP analysis does not guarantee correct displacement estimates. To be clear, the HARP tracking algorithm will converge in all cases, but in the case of large motion, it will converge to a point having the same pair of HARP values but is one or more tag periods away from the true corresponding point [48].

2.2.1 HARP Refinement

In [48], a method called the HARP refinement method based on seeded region-growing is introduced. Starting from a seed point, defined by the user, to be tracked correctly through the entire sequence, this method tracks the motion of the entire tissue. Once the seed point

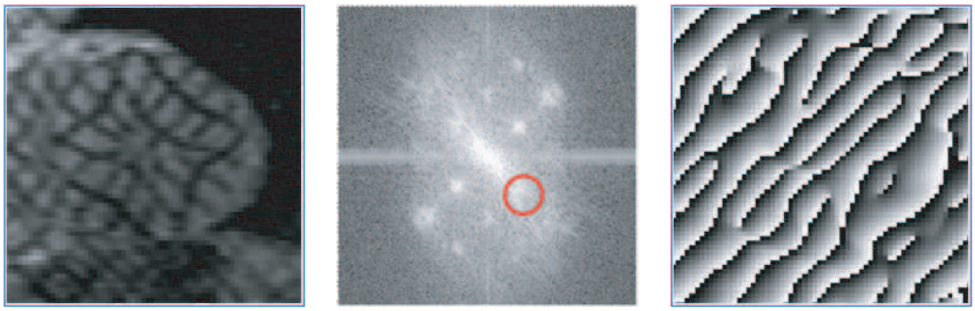

(a) (b) (c)

Figure 2.7: (a) a tagged short-axis image acquired near end-systole in a normal human; (b) the Fourier transform log-magnitude of (a); (c) HARP image obtained by bandpass filtering around one of the peaks in (b).

is tracked, its neighbors are added to a sequentially sorted list (SSL). These points are known as boundary points. The first point on the SSL is then tracked with the initial guess for HARP tracking being provided by the displacement of the seed point. After tracking, this point is added to the list of seed points and its neighbors added to the SSL. The points in the SSL are sorted based on a cost function. The cost function is defined as the wrapped phase difference between the boundary point in the reference time frame and the initial guess provided for HARP tracking in the target time frame. Illustration of the region-growing method is shown in Figures 2.8(a)-2.8(f).This method was applied on tagged MR images of the tongue. It was seen that some points that were mistracked using the traditional HARP tracking method were corrected using the HARP refinement procedure. This method thus makes it possible for more accurate HARP tracking.

2.2.2 Extended HARP Tracking

Due to the combination of the conical shape of the heart and its longitudinal motion, new tissues appear during the systolic phase near the epicardial contour and other tissues disappear near the endocardial contour. Since these new tissues are not present during the time frame with the undeformed tag pattern, their angle values are not available and,

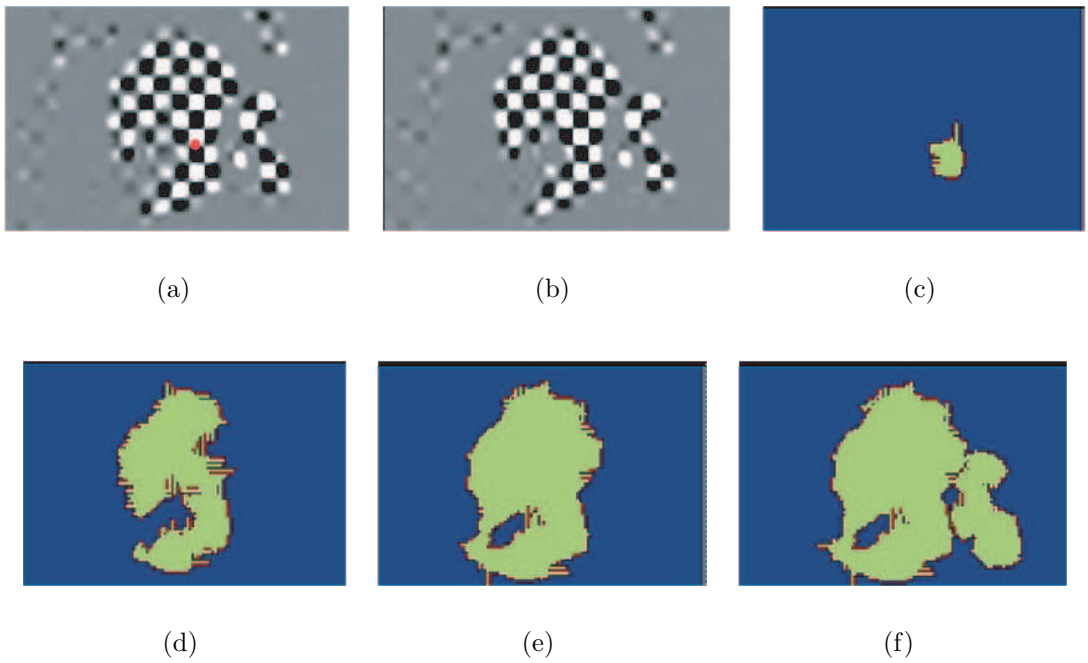

Figure 2.8: Illustration of the region-growing process [48]. (a) is the checkerboard image at the first time frame by overlaying two perpendicularly oriented tagged images. (b) is the checker board image at the second time frame. The red dot in (a) is the manually placed seed point. (c-f) shows how the region grows. The green color means tracked points, brown means boundary points, and blue means points that are not tracked and not boundary points.

consequently, these points are not tracked. However, disregarding these points can lead to systematic errors in the strain results, due to the transmural gradient in the strain. In [77], an extended HARP tracking method is described, which tracks the new points that enter into the image plane during the systolic phase and recovers the points that reappear at the endocardial contour during the diastolic phase. With this extended method, the authors aim to track all parts of the myocardium completely during all phases of the cardiac cycle.

First, the myocardial contours for the target and reference time frames are computed. All points inside a square region encompassing the myocardial contours and points within an additional distance of two tag lines from the contours in the reference time are tracked. The resulting tracked points are then classified into active and inactive points. Active points are those that fall inside the myocardial contours in the target time and also satisfy a set of conditions relating to the topology. HARP tracking can be erroneous in areas of large displacements; the topology-based conditions remove these points off the active list. After tracking all active points, the absolute displacement field is computed and used to estimate the displacement of the inactive neighbors. If a point is currently inactive but one or more of its near neighbors is active, the displacement of this inactive point is set equal to the averaged displacement of its active neighbors. The resulting estimated displacement is applied to the inactive point. If the estimated position falls inside the current contours, the point is made active and it is tracked. This procedure is continued for all the time frames. Figure 2.9(b) demonstrates the increased myocardial coverage as a result of the extended version of HARP tracking.

Comparing the strain results obtained with both HARP tracking versions, it was observed that, on average, the extended version leads to less circumferential shortening. The decrease is expected, since the myocardium points near the endocardium have higher circumferential shortening and the original HARP tracking version is biased toward this region. Therefore, in comparison with the original HARP tracking version, this extended version leads to strain results that represent more of the myocardium.

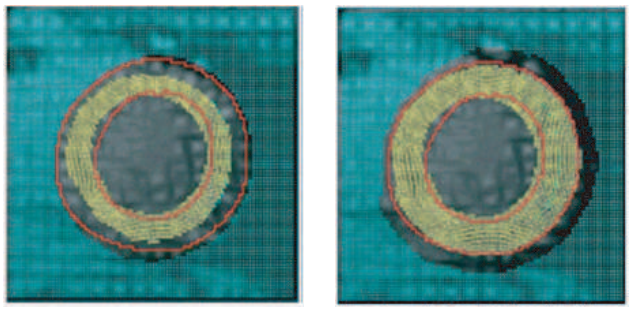

(a) (b)

Figure 2.9: Visualization of the rectangular region of tracking encompassing the left ventricular short-axis image at end-systole [77]. The red curves represent the myocardial contours, the blue marks the inactive points and the yellow marks the active points. Since the endocardial contour is difficult to delineate, a point that is successfully tracked and falls less than two pixels in distance outside the endocardial contour is labeled as active. (a) Original HARP tracking version. (b) Extended HARP tracking version.

2.2.3 3D HARP

3D-HARP [27] is a fast, semiautomatic method for tracking three-dimensional (3-D) cardiac motion from a temporal sequence of short-axis and long-axis tagged MR images. This method extends the HARP approach, previously described for two-dimensional (2-D) tag analysis, to 3-D. A 3-D material mesh model is built to represent a collection of material points inside the left ventricle (LV) wall at a reference time. Harmonic phase, a material property that is time-invariant, is used to track the motion of the mesh and deform the mesh along with an additional constraint to control the internal properties of the mesh.

The basic algorithm is as follows. The user initializes the 3D material mesh (Figure 2.10) at the initial time frame. In the next time frame, intersection points of the mesh with the image are determined. If the phase-time invariance is not satisfied, the in-plane motion is determined using 2D HARP tracking. Based on the tracking, the material mesh is deformed. This is illustrated in Figure 2.11. In (a), the material mesh intersects with an SA image plane S. The intersection point $y(\mu)$ is located on both the image plane and the material mesh. y' is the closest point to the intersection point $y(\mu)$ on the image plane S that has

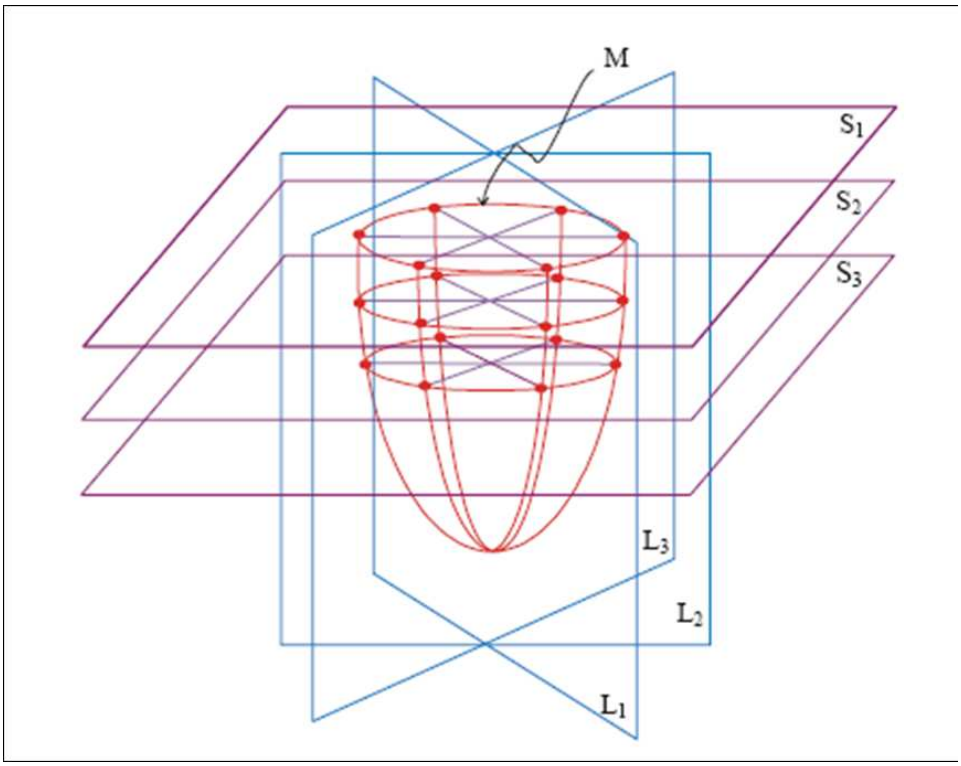

Figure 2.10: A material mesh built at the reference time [27]. S is an SA image plane and L is an LA image plane.M is the material mesh. The material mesh is initialized as latitude circles and longitude lines.

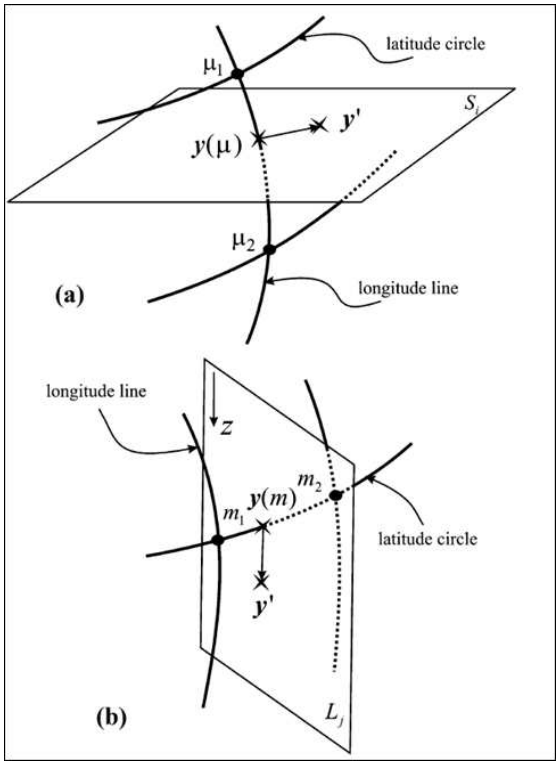

Figure 2.11: Diagram of the intersection of the material mesh and image planes, as well as a description of the in-plane motion of intersection points in (a) SA case and (b) LA case [27].

the same 2-D phase value as the initial phase value, of μ. The displacement vector between y and y' describes the in-plane 2-D motion of the intersection point $y(\mu)$. Similarly, in (b), the material mesh intersects with an LA image plane L at the intersection point $y(m)$, and y' is the closest point to the intersection point $y(m)$ on the image plane L that has the same 1-D phase value as the initial phase value of m. The displacement vector between y and y' describes the in-plane 1D motion of the intersection point. This procedure is repeated till the phase-time invariance is satisfied to obtain the material mesh at that time. This material mesh is then used as the initial mesh for the next time to be tracked.

Various motion-related functional properties of the myocardium, such as circumferential strain and left ventricular twist, are computed from the tracked mesh. This method though is less robust to large interframe deformations and can track motion only in the middle third of the myocardium.

2.3 Optical-Flow Methods

Optical-flow methods have been developed for the analysis of tagged cardiac MR images [41–43]. These methods use low-frequency tag patterns, modeled as sinusoidal brightness patterns. Dense motion estimates can be obtained using gradient-based optical flow motion estimation techniques. The brightness constraint equation (Equation (2.5)) is the basis for this method. The equation is

$$\phi_x u + \phi_y v + \phi_t = 0, \tag{2.5}$$

where ϕ denotes the pixel intensity and (u, v) are the velocity components to be determined. This method involves estimating the spatial gradient of the intensity image, using finite differences of the intensities at neighboring pixels, as well as a temporal intensity derivative which is estimated by subtracting the intensity at a pixel from one time frame to the next in a cine acquisition. The resulting formulation requires the solution of a pair of coupled partial

differential equations (PDEs) to find the velocity field estimate. This method assumes that a material point possesses the same brightness throughout the entire cycle, but tags fade over time in MR images, and this assumption fails. Variable-brightness optical-flow methods have been suggested that model the tag fading over the time sequence and produce more accurate displacement fields [43]. One problem with these methods is that, to measure large motions, like the ones between end-diastole and end-systole, the motion between intermediate time-frame images has to be measured, and tracking is necessary to obtain total motion.

2.4 Non-rigid Registration Techniques

Non-rigid registration methods use a similarity criterion and transformation models to estimate the deformation in a sequence of images. Chandrashekara et al. [70] first developed a method for computing myocardial motion using non-rigid registration. Recently, robust methods for computing displacement fields in tagged MRI [78] as well as from cine MR images [58] have been developed.

Chandrashekhara et al. [70] used normalized mutual information as the similarity measure to obtain the displacement field. This procedure involves the combined nonrigid registration of SA and LA images. Initially one volume is built from the SA stack and another from the LA stack of images. Mutual information is then used to obtain the local affine deformation field between two volumes from adjacent time frames. The similarity measure used is a summation of the mutual information from the registration of the SA stack volume and the LA stack volume. The affine transformation obtained between successive time frames is then aggregated to obtain the displacement field back to end-diastole.

Ledesma-Carbayo et al. [78] use a multi-source nonrigid registration algorithm to compute the displacement field from vertical and horizontal tagged images. A series of transformations between successive pairs of images is defined. The transformation field was then optimized based on an energy term comprising two terms. The first term (data term) computes the sum of squared differences between the reference image and the deformed image

from the two sources. The second term (regularization term) was chosen as the vector Laplacian of the resulting transformation. This scheme also used multiresolution to improve the speed and robustness of the process.

2.5 Conclusion

All of the above methods are ill posed: thermal noise and image artifacts can cause ambiguities in the tracking of tag, optical flow or phase features. The above tracking methods tend to be problematic near the boundary, where the epicardial and endocardial surfaces often appear as dark lines and thus can be confused as tag features. The myocardium near the boundary is also particularly difficult to characterize because tag lines can appear or disappear due to through-plane motion of the myocardium. These conditions near the boundaries can cause failures for all the algorithms in several ways:

1. The intensity template used by the feature-based methods may lock onto the boundary instead of a tag.

2. The boundaries can occlude tags and can act as spurious matches that confound the optical-flow solution and the non-rigid registration techniques.

3. The boundaries can introduce apparent shifts of the tagging pattern in subendocardial and subepicardial tissue, which can cause inaccuracies in the motion recovered from harmonic phase method.

As a result, researchers have used regularization methods to find a motion field which balances fidelity to tag features with a smoothness constraint imposed on the overall motion field.

Tag tracking based on feature extraction has an advantage over the optical-flow, HARP and non-rigid registration techniques, in that the tracked tags can be manually corrected. The tag points that are detected using feature-based techniques can be moved around by the user to the correct location after manual inspection. HARP and non-rigid registration

though produce denser displacement estimates and hence alleviate the need for interpolation. 2D HARP strain (without tracking) is the preferred method for computing 2D strain maps as there is no need for tracking the material points. This method though can be erroneous; moreover, 3D strain maps can be more beneficial for diagnostic purposes.

We have studied the procedures generally followed in the analysis of tagged MR images. Many different techniques can be applied in the segmentation of the myocardium and the tracking of tissue. All of these methods are plagued by inaccuracies as a result of various imaging factors. The obtained displacement field is smoothed to alleviate the inconsistency in the obtained deformation field. The scope of improvement in analysis techniques is limited to the quality of images obtained. In the next chapter, we look at a few MR imaging methods that seek to improve upon the MR tagging technique both in terms of ease of analysis and the accuracy of measurements.

Chapter 3

Other MR Imaging Methods to Compute Myocardial Function

MR imaging methods based on MR tagging [11, 79], phase-contrast velocity imaging [80, 81] and stimulated-echo imaging [82–84] have been used to study the regional functional characteristics of the heart. Recent advances in imaging methods [27, 85–87] have improved the clinical viability of MR imaging techniques. Most of these advances are nascent and have not yet found their way into regular clinical use.

3.1 3D Myocardial Tagging

The 3D-CSPAMM [79] tagging preparation is an extension of the 2D-CSPAMM sequence. CSPAMM is based on the subtraction of two images with complementary signed tagging modulation. The subtraction technique reduces tagline intensity fading and consequently allows observation of the heart motion throughout the heart cycle. The 3D-CSPAMM tagging preparation generates a 3D tagging grid on the myocardium. Two 90^o block pulses, interspersed by a dephasing gradient, produce a sinusoidal modulation of z-magnetization and thus a line-shaped tag pattern. To generate a 3D tagging grid, the modulation is repeated in all three spatial directions. 3D-CSPAMM is a valuable technique to register the 3D motion of the myocardium. It overcomes the matching problems that may arise when combining short-axis and long-axis tagging images to generate 3D tagging images. The major disadvantage is that the scan duration is 40 minutes which is almost double that of SPAMM tagged MR images.

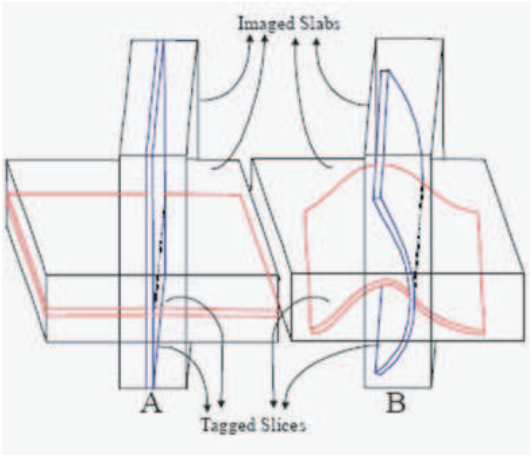

Figure 3.1: SF HARP illustration. A thin slice is selectively tagged while imaging a larger slab that encompasses the moving tagged slice [87].

3.2 Slice Following HARP

The slice following (SF) CSPAMM technique [87], selectively tags a thin slice at an early time frame A while imaging a large slab that always encompasses the moving tagged slice even at a later time frame B (Figure 3.1). After subtracting the complementarily signed tag-modulated images, the reconstructed images represent the same material slice at all time points irrespective of where it has moved in the through-plane direction. Therefore, performing 2D HARP point tracking on these SF images yields a true 2D displacement of the material point. Now consider two orthogonal SF tagged slices, both of which have two tag orientations, and consider a point lying on the intersection of the original tag planes of these slices. Such points have two projected pathlines that can be computed using 2D HARP tracking on orthogonal planes (Figure 3.2), and these projected pathlines can be combined into a single 3D pathline representing the 3D motion of an MR marker. This can be done on any such intersection point and can be computed automatically.

3.3 zHARP

zHARP [86] is a novel method for calculating cardiac 3D strain using a stack of two or more images acquired in only one orientation. The zHARP pulse sequence encodes in-plane

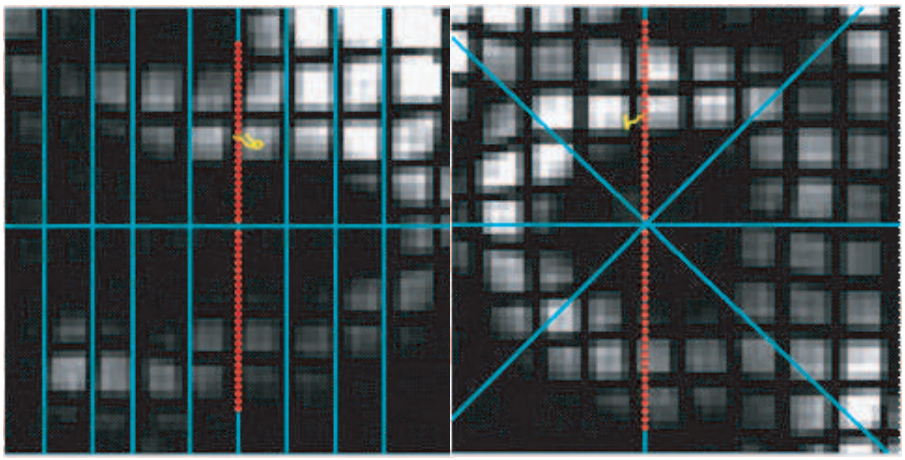

Figure 3.2: SF HARP Planes Illustration. Points common to SA and LA slices would have two pathlines tracked using 2D HARP. These are combined to give a 3D pathline [87].

motion using MR tagging and out-of-plane motion using phase encoding, and is capable of computing 3D displacement within a single image plane. Here, data from two adjacent image planes are combined to yield a 3D strain tensor at each pixel; stacks of zHARP images can be used to derive stacked arrays of 3D strain tensors without imaging multiple orientations and without numerical interpolation.

The proposed technique, zHARP, is similar to the standard slice-following CSPAMM (SF-CSPAMM), except that during the imaging sequence, a small z-encoding gradient is applied immediately before the readout and again with opposite polarity to the second orthogonal CSPAMM acquisition. This gradient adds a z-position dependent phase φ_z to every material point in the acquired slice. This additional phase is linearly related to the distance of the point from the iso-center. Unfortunately, susceptibility and general field inhomogeneities lead to an additional and artifactual phase accumulation. This erroneous phase is identical in both the horizontally and vertically tagged images, which can be exploited to separately compute the in-plane and through-plane displacements. The algorithm runs on the two orthogonally tagged data. First, k-space data are processed using HARP, upon extracting both the positive and negative harmonic peaks. Second, the harmonic phase maps φ_x, φ_y and φ_z, in the x, y and z directions are computed. Third, material points are tracked

in 3-D. Given an arbitrary material point, a tracking procedure is introduced to track the in-plane motion using HARP on the φ_x and φ_y maps, from which the z-position can be extracted using the φ_z map.

The zHARP technique is a modification of SF-CSPAMM, where encoding gradients add a through-plane motion-dependent phase to every material point in the acquired slice. Data acquisition for zHARP requires no extra time over a conventional CSPAMM acquisition; however, the spatial resolution and accuracy of this method have yet to be carefully evaluated.

3.4 Combined Harmonic Phase and Strain Encoded MRI

HARP-SENC MRI [85] is a method to measure the dynamic evolution of three normal components of myocardial strain within a six-heartbeat acquisition per imaging slice using a HARP-SENC MRI pulse sequence. The calculation of the true 3-D strain tensor cannot be obtained using this technique described, as longitudinal shear components are not measured. The post-processing of the datasets acquired from a six-heartbeat breath-hold provides full quantification and visualization of three-component myocardial strains with good temporal resolution in a single SA slice. For a stack of n contiguous SA slices prescribed in the left ventricle, these images are acquired in a single breath-hold lasting $6n$ heartbeats. This method is still under development, as some artifacts have been observed in the SENC images.

3.5 DENSE

Displacement encoding with stimulated echoes (DENSE) is a quantitative MRI technique that encodes tissue displacement into the phase of the complex MRI images [83,84,88]. Cine DENSE provides a time series of these images, thus facilitating the non-invasive study of myocardial kinematics. DENSE images are used for the quantification of regional displacement and strain as a function of time.

Spottiswoode et al. [82], developed a method for analyzing DENSE image sequences using a 3D flood-fill phase unwrapping method. To achieve enhanced motion sensitivity, relatively high displacement encoding frequencies are used to capture DENSE images and phase wrapping typically occurs. Algorithms to phase unwrap a time series of cine-DENSE images, thus enabling the computation of absolute myocardial motion trajectories are developed. The unwrapping was implemented by extending a 2D quality-guided path following phase unwrapping method [89] to unwrap phase through time as well as space.

Let $\varphi(i,j)$ be the wrapped phase and $\phi(i,j)$ be the true, unwrapped phase. The coordinates i and j define the pixel position within the image. Phase wrapping can be defined as $\phi(i,j) = \varphi(i,j) + 2\pi k(i,j)$, where $k(i,j)$ are integers that force $\varphi(i,j)$ to lie between $-\pi$ and π radians. Phase unwrapping entails determining all values of $k(i,j)$, and it can be done along a particular path by integrating the wrapped phase differences of the initially wrapped phases.

The 2D quality-guided phase unwrapping method uses a measure of phase "quality" to guide the path of unwrapping. A good measure of phase quality is a root-mean-square measure of the variances of the spatial partial derivatives within an $n \times n$ pixel region. The unwrapping path is guided by a region-growing algorithm, which floods into regions of high-quality phase before those with lower quality. Figure 3.3 captures six steps of the 2D quality-guided flood-fill procedure commencing from an arbitrary seed point in the myocardium, and using the phase quality map shown in Figure 3.4(c).

To obtain absolute phase measurements, it is necessary that the unwrapping path be initiated on a portion of tissue with known absolute phase. Very little cardiac motion takes place between the displacement encoding and the acquisition of the first frame of cine-DENSE data. It is therefore characteristic that no phase wrapping will have occurred on the first frame, and that all phase measurements in the myocardium will be absolute. Unwrapping the phase through time will thus result in measurements of absolute phase for all frames. This implicitly assumes that the true motion magnitude between frames for each pixel separated

in time amounts to less than $|\pi|$ radians. This will always be the case given practical values of pixel size and displacement encoding frequencies. If the phase quality maps for a cine series are stacked on top of each other, then the quality-guided algorithm can easily be adapted to unwrap in 3D (one temporal and two spatial dimensions).

The following algorithm for unwrapping cine DENSE phase images was implemented:

1. Calculate phase quality maps for all frames.

2. Manually place a seed point anywhere in the myocardium on the first frame.

3. Perform 3D quality-guided phase unwrapping, limiting the spatial unwrapping to a specified radius per frame. As soon as an unwrapped pixel appears on a particular frame, disallow all unwrapping for all previous frames.

4. Once unwrapped pixels are present on all frames, perform 2D quality-guided phase unwrapping for each frame independently, starting at the correctly unwrapped reference pixels.

Step 2 serves to force the unwrapping through time using only high phase quality. If the 3D quality-guided flood-fill is used for the entire unwrapping process, phase inconsistencies are introduced at the later stages of the procedure due to temporal unwrapping between isolated regions of high-quality phase in the noisy areas (lungs and ventricular cavities) and regions within the myocardium. The radius size is set based on the frame rate and the maximum expected amount of cardiac displacement per frame. It should be large enough to allow the 3D unwrapping to migrate spatially with the ventricle as it moves, but small enough to restrict the 3D unwrapping to relatively high values of phase. A radius of 2 pixels was used here.

Once the images were unwrapped and the trajectories tracked, a fifth-order Fourier series curve is fitted to the tracked trajectories. This improves the accuracy of measurements for noisy image data.

Figure 3.3: Progression of the guided flood-fill operation using the quality map in Figure 3.4(c). The calculation intervals are arbitrary.

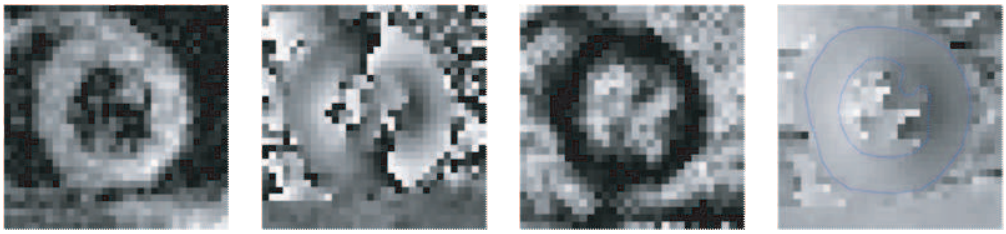

(a) (b) (c) (d)

Figure 3.4: (a) Short-axis DENSE magnitude image. (b) Wrapped DENSE phase image for horizontal motion. (c) Variance of the derivatives of the locally unwrapped phase for the four neighboring pixels. (d) Unwrapped image with LV endocardial and epicardial contours superimposed. [82]

A useful method for estimating where phase-unwrapping errors may have occurred involves combining a map of unwrapped phase discontinuities with the phase quality map. The discontinuity map specifies the locations of pixels that differ from a neighbor by more than π radians. Unwrapping errors are likely to have occurred within regions isolated by the combined map. The combined maps were used to aid a visual inspection of the left ventricle (LV) for unwrapping errors. If a single error was encountered, then the image was deemed incorrectly unwrapped. It was shown that this method correctly unwrapped 786 out of the 800 images analyzed (98.3%).

The only manual interaction required was the placement of a seed point and the myocardial contours. The rest of the algorithm is automated. It was shown that the strain measurements obtained were comparable to those obtained from tagged image data.

3.6 Conclusion

MR tagging of the myocardium is a powerful method for assessment of regional myocardial deformation. It has permitted new insights into normal physiology and myocardial diseases. Applications of MR tagging in a routine clinical setting are yet to be commonplace due to the long imaging times and expensive and time-consuming post-processing procedures. Automated tagged image analysis procedures are an active research area. Many of the concepts developed in the analysis of tagged images can be useful in the analysis of images obtained from newer and faster imaging methods. With effective solutions in both analysis procedures and imaging methods, tagged MR imaging is likely to become an important technique for clinical assessment of cardiovascular function.

Chapter 4

Objectives

This chapter discusses the objectives and contributions of this dissertation. As discussed in Chapter 2, there are several problems with the existing cardiac motion tracking methods in tagged MRI. The feature-based methods involve tracking of tags as dark intensity lines. Mistracking of tags is a big problem and there is a need for extensive manual intervention to correct for the errors in tracking. This procedure is tedious and cumbersome when a series of images have to be processed. Interpolation is also necessary to produce dense displacement fields. The phase-based methods overcome the need for interpolation. They do not require any manual intervention but, this is a disadvantage as it does not allow for correction of errors after tracking. HARP tracking produces incorrect results when the displacement of the tracked tissue between consecutive time frames is more than one-half the tag-spacing (because of phase ambiguity). The 3D imaging methods discussed in Chapter 3, require lesser analysis time but need twice the amount of time to acquire a slice.

The objective of this research was to develop a method to compute 4D strain in the human heart using tagged MR images. The method:

1. must require minimal user intervention.

2. should be capable of measuring strain through to mid/end diastole.

3. should include a way to recognize and fix the errors from the automatic algorithm.

4. should produce dense displacement measurements.

5. should be robust to large inter-frame motion.

First, the phase ambiguity problem in HARP tracking was solved by unwrapping the HARP phase image. Different methods of phase unwrapping were explored and a suitable procedure for unwrapping a sequence of HARP images was identified. The residue-compensation procedure (see Chapter 5), where inconsistencies in the phase image are removed using branch cuts was chosen. A graphical user interface to help the users place branch cuts was developed and a procedure to efficiently and accurately compute displacements by unwrapping a sequence of images was devised. The procedure developed was faster to compute 3D displacement over time and produced denser displacement fields compared to the feature-based methods. It was more accurate compared to the HARP tracking procedure. Since it used SPAMM tagged MR images, the acquistion of a slice was twice as fast compared to other recent 3D MR imaging methods.

Secondly, the phase unwrapping method was extended to obtain 4D strain in the RV. Obtaining 4D strain in the RV has been problematic because of the thin myocardium and the lack of geometric symmetry in the RV. The thin myocardium causes problems in tissue-tracking in feature-based (too few tag points to reconstruct deformation field) and phase-based methods (interference from myocardial borders is greater). Using the phase unwrapping procedure developed for the LV (Chapter6), a dense deformation field with no tracking errors was obtained. The DMF method (see Chapter 2) is then used to compute 3D strain from the unwrapped-phase-derived displacement measurements. The DMF method has the advantage of not requiring the object being modeled to have geometric symmetry and hence produces accurate biventricular strains.

Thirdly, a computer-assisted approach was developed for the placement of the branch cuts and unwrap a sequence of images. Here, branch cuts are automatically placed using either a simulated annealing procedure or an exhaustive search procedure. An energy function was proposed to impose temporal continuity of the unwrapped phases between time frames. If errors were detected after the automated placement of branch cuts, the user corrected the

branch cut configuration. This procedure reduced the time taken for manual intervention to about one-third of that of the procedure where all branch cuts were manually placed.

Fourthly, An explanation of the energy mechanics in the heart using commonly measured parameters is explored. Parameters that are measured easily such as volume, area, strain and torsion are used to develop a framework to classify hearts based on their energy consumption through a cycle.

Chapter 5 reviews the problems and current techniques associated with phase unwrapping. Chapter 6 presents a method to manually correct the problems and then unwrap HARP images to obtain strain (this work was published in JMRI 2010 [90] and ISBI 2008 [91]). Chapter 7 compares 2D and 3D torsion measured from tagged MR images and explains the effect of through-plane motion on obtained measurements (this work was published in ISMRM 2009 [92]). Chapter 8 extends the concept of phase unwrapping to the right ventricle (RV) to obtain 4D biventricular strain (this work was published in ISMRM 2010 [93] and ISMRM 2008 [94]). Chapter 9 describes a computer-assisted technique for phase unwrapping HARP images (this work was published in ISBI 2009 [95]). Chapter 10 explains the energy mechanics in the heart using commonly measured parameters.

Chapter 5

Phase Unwrapping

5.1 Introduction

This chapter starts out with an introduction to phase unwrapping followed by a comparison of the results to determine the best method. Other implementation issues specific to the geometry of the heart are also discussed.

Phase unwrapping is a well established field in other forms of imaging such as SAR interferometry [96], optics [97] and brain MRI imaging [98]. It is a well-researched problem. Our aim here is to unwrap the HARP images [49]. As we shall see through this chapter, it is a difficult procedure as it is sensitive to noise and phase aliasing.

When continuous phase is wrapped, it lies between $-\pi$ and $+\pi$. This is normally so because phase is obtained using the arctangent function. The procedure of making the discrete wrapped phase continuous to give the continuous unwrapped phase that lies from $-\infty$ to $+\infty$ is called phase unwrapping. It is important to understand the aspects involved in one-dimensional phase unwrapping before we proceed to two-dimensional (images) phase unwrapping. Let us look at a simple example of a one-dimensional phase unwrapping problem. Consider a complex signal,

$$s(t) = e^{j5\pi t}, \quad 0 \leq t \leq 1 \tag{5.1}$$

We wish to reconstruct the continuous phase $\phi(t) = 5\pi t$ from $s(t)$. We can only obtain the wrapped phase estimate $\psi(t)$ by using the arctangent function of the imaginary phase ($\Im(s(t))$) over the real phase ($\Re(s(t))$) to extract phase.

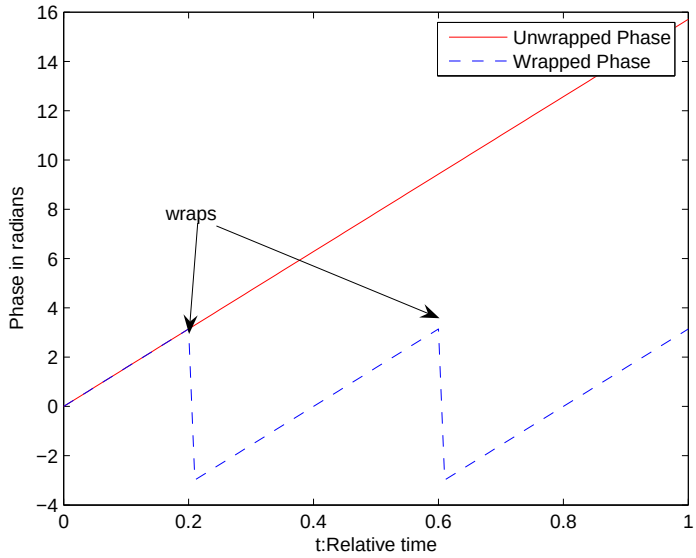

Figure 5.1: Illustration of one-dimensional phase unwrapping

$$\psi(t) = \arctan \frac{\Im(s(t))}{\Re(s(t))} \tag{5.2}$$

An illustration of one-dimensional phase unwrapping is given in Figure 5.1. The phase wraps at π and 3π can be clearly seen. It is also clear that by adding 2π at the first phase wrap and to every subsequent point thereafter until the next wrap occurs, the wrapped and the unwrapped phase would match. By adding 2π every time the phase wraps (drops by) 2π, we can reconstruct the continuous phase. The phase wraps themselves are detected by observing the phase differences. A simple unwrapping operation can be defined as follows:

$$\begin{aligned} \psi(n) - \psi(n-1) \geq \pi \quad &\Rightarrow \quad \phi(n) = \phi(n) - 2\pi \\ \psi(n) - \psi(n-1) \leq \pi \quad &\Rightarrow \quad \phi(n) = \phi(n) + 2\pi \end{aligned} \tag{5.3}$$

There are many problems associated with one-dimensional phase unwrapping that are of interest to us. First is the problem of phase aliasing [99]. If the data is sampled at a lower rate such that one of the phase wraps is completely missed, then the phase calculated thereafter is all wrong. This is a particular problem that we experienced in tagged cardiac MRI. For example, in Figure 5.3(a), we can see two tag lines merge (at 4 'o clock). This would amount to missing of a phase wrap while unwrapping. Another problem is the noise associated with the signal. If the signal is noisy and a phase wrap is not detected in the unwrapping procedure, the unwrapped phase would be faulty. These are two of the most important factors that ultimately decide the applicability of phase unwrapping to a given problem.

The easiest way one can think of implementing phase unwrapping for images is to extend the one-dimensional algorithm to the two-dimensional case, but there are some problems that are introduced when we want to use phase unwrapping in images that make it ineffective. Shearing of the phase plane is one of the problems. This gives rise to both problems of phase aliasing and introduction of singularities in the wrapped phase. Singularities are undesired points of discontinuity. Rotation of the phase plane too is a problem as it introduces phase aliasing. These are two of the more difficult ones to deal with because of the shearing and rotation the heart undergoes at and near end-systole. In the regions of blood flow and air in the image obtained, the MR signal is corrupted leading to a noisy phase. This noise in the phase obtained at points outside the myocardium makes the algorithm highly sensitive to the myocardial segmentation. It is important to realize that any algorithm designed should deal with all these problems in a satisfactory way. With this introduction, we shall look at the two-dimensional unwrapping terminology and the various methods that were implemented [89]. Phase unwrapping has already been used for motion estimation using CINE DENSE [82]; here we try to use it for SPAMM-tagged images.

5.2 Two-dimensional Phase Unwrapping Terminology

5.2.1 Residues

Residues arise out of singularities in the wrapped phase or zeros in the complex function used to derive the wrapped phase. They are the cause for inconsistencies in the image. A simple method for identifying the residues is by unwrapping around a small 2×2 block around a pixel.

$$\mathbf{res} = \sum_{2\times 2} \nabla\psi \tag{5.4}$$

This is the smallest loop one can obtain in an image. The sum of the phase differences around the 2×2 block should be zero. If the result of the unwrapping, **res**, is not zero, then a residue is said to be present. Residues in general add up to either $+2\pi$ or -2π and are respectively known as positive or negative residues. Residues are a major problem in phase unwrapping and the presence of residues implies that the unwrapping is no more path-independent. Removal of residues is essential to obtain unwrapped phase without any discontinuities.

5.2.2 Dipoles

It is common to see positive and negative residues next to each other in the image. These are known as dipoles and are removed from the image. The basic concept of residue removal is the neutralization of the charges on the residues; connecting a positive residue to a negative residue and vice versa. A dipole is already balanced.

5.2.3 Branch Cuts

The connection of a positive and a negative residue in an image is known as a branch cut. A decision must be made as to which positive and negative residues the branch cut should

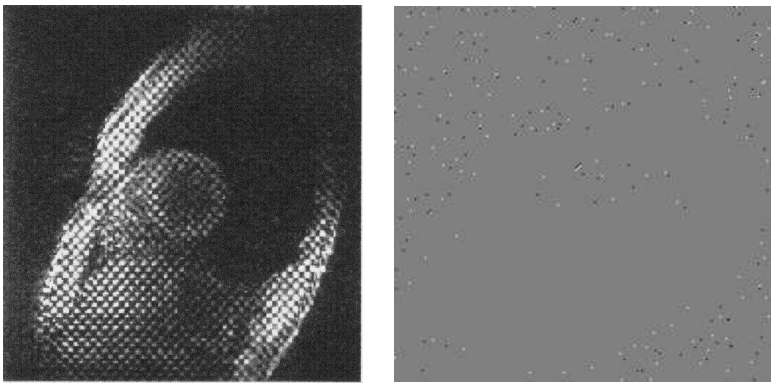

(a) (b)

Figure 5.2: (a) The original MRI image; (b) The residues are marked black and white for negative and positive residues respectively. The number of residues is clearly larger in the outer areas where there is air and areas of the image with large motion compared to the areas with tissues as seen in the original MRI image.

connect. In general, every image has an equal number of positive and negative residues. The two most popular and widely used methods for balancing the residues are:

- minimizing the aggregate length of the branch cuts
- choosing the shortest branch cut available every time

In our algorithms, the objectives are:

- to obtain the unwrapped phase only inside the myocardium
- not to isolate any portion of the myocardium
- keep the myocardium on a whole connected

These objectives are important when using path-following methods to do the unwrapping.

5.2.4 Quality Maps and Masks

In the path-following methods of phase unwrapping, it is necessary to base the integration on a certain quantity that will improve accuracy. This is done by the use of phase

quality maps [100]. The two most common quantities used to describe the quality are the phase derivative and the phase derivative variance. In the phase derivative quality map, the wrapped phase derivative at each point represents the quality map. The phase derivative variance map z was obtained as follows:

$$z_{m,n} = \frac{\sqrt{\sum(\Delta^x_{i,j} - \overline{\Delta^x_{m,n}})^2} + \sqrt{\sum(\Delta^y_{i,j} - \overline{\Delta^y_{m,n}})^2}}{k^2} \tag{5.5}$$

where for each sum i, j varies over the $k \times k$ window centered at the pixel (m, n). The terms $\Delta^x_{i,j}$ and $\Delta^y_{i,j}$ are the wrapped phase derivatives, and $\overline{\Delta^x_{m,n}}$ and $\overline{\Delta^y_{m,n}}$ are the average of the derivatives in the $k \times k$ window. Normally, 3×3 window is used. Both the methods were tested and it was found that the phase variance performed better but had a longer execution time by a factor of 20 times. The phase derivative quality map was less accurate but faster.

Quality maps can be thresholded and the resulting binary image used as a mask in both the path-following methods and the least-squares methods. Thresholded quality maps are also used to segment the myocardium when only the myocardial phase is of interest.

5.3 Two-dimensional Phase-Unwrapping Algorithms

Phase unwrapping algorithms can be classified into two main categories, the path following methods and the least-squares methods. Several different algorithms from each type were implemented and their performance studied, [96, 101–105]. We shall only take a look at the basic ones and those that were implemented here.

5.3.1 Path-Following Algorithms

The path-following algorithms are a set of algorithms that perform phase integration so as to cover all the pixels in the image. They can be classified into three groups:

- path-dependent algorithms

- quality-guided algorithms
- residue-compensation algorithms

Path-Dependent Algorithms

These are the simplest algorithms and perform integration over a fixed path. They use a predefined strategy to do the unwrapping such as linear scanning, spiral scanning and multi-directional scanning. These algorithms follow a fixed order where unwrapping starts from a seed point and follows to a pixel in the predefined path. This continues till all the pixels are unwrapped. This strategy implies that if unwrapping of one of the initial pixels is wrong, all the pixels unwrapped henceforth are wrong. Moreover, the fixed order implies that it does not have the ability to avoid residues present in the path.

Quality-guided Algorithms

The quality-guided algorithms are a very robust set of algorithms as far as dealing with noisy phase data is concerned, but, since they are path-following methods, they fail to unwrap correctly when there are residues in the image. The underlying logic in every quality-guided method is simple, and they are generally fast methods. These characteristics make them popular methods to use once it has been verified that there are no residues in the image. For all the algorithms, a seed point is chosen initially. The choice of the seed point is random in most applications. From the seed point, the algorithm travels to a pixel of highest quality among its neighbors (a 4-pixel neighborhood is ususally considered) and so on till all the pixels in the image have been traversed. The quality being assessed is derived from the quality maps. It can be the pixel of lowest phase-derivative variance or the lowest phase derivative with respect to the present pixel or any other such measure. In our case, the variance map is chosen, as it is the most accurate and fairly robust in its unwrapping. It has to be used in conjunction with some other method to remove any residues or unbalanced charges that remain in the unwrapping path. This is explored in detail in the next chapter.

Residue-Compensation Algorithms

These algorithms place branch cuts to balance the residual charges. The branch cuts are placed, the unwrapping is path independent and any path can be chosen to unwrap the images. In reality, the criterion to choose a branch cut is not so easy, and one cannot be totally sure that the resulting phase is correct [106]. In our case it is even more difficult, as we want all the areas inside the myocardium to be connected and therefore avoid all branch cuts from passing through the myocardium. We prefer to unwrap the pixels in the myocardium only because the pixels outside are generally too noisy. The difficulty is choosing the right branch cut with respect to the wrapped phase observed in the heart. This is explained in detail in future chapters.

We can look at an example where we look to unwrap the wrapped image from Figure 5.3(a), which has already been segmented. The point of residues clearly are the places where the two phase (wraps) lines meet (4 o' clock) and the premature ending of the phase (wrap) line near the epicardium (10 o' clock). It can be clearly noticed that, without branch cuts, the phase is discontinuously unwrapped as in Figure 5.3(b). Figure 5.3(c) shows the result that is unwrapped with branch cuts. The unwrapped phase appears smooth and would seem to be the right phase when in actuality it is not. By rearranging the branch cuts as in Figure 5.3(d), we again obtain a smooth phase but this time it is correct as compared to the expected phase.

It is a fact that branch cuts may lead to smoothly unwrapped phase, but the unwrapped phase is not necessarily correct. Therefore the residue-compensation methods must be used with care. While they make the process on the whole slightly more accurate, they also make it unpredictable. A procedure for placing correct branch cuts to obtain correctly unwrapped phase is explained in Chapter 6.

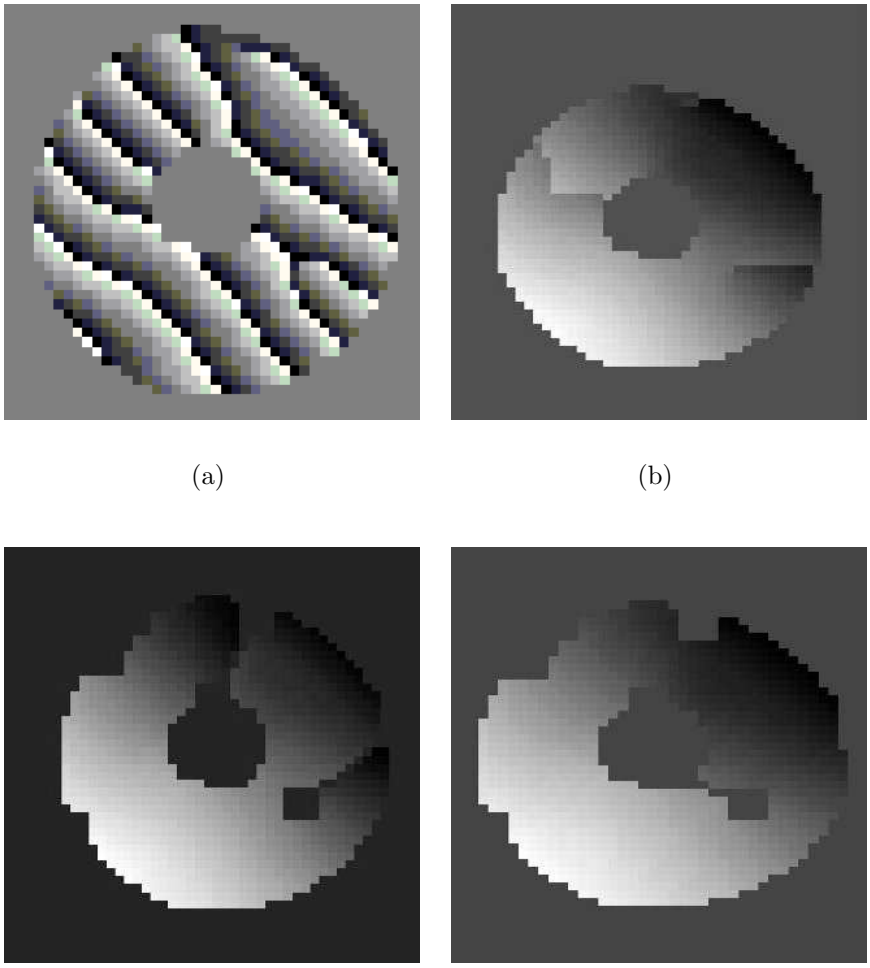

(a) (b)

(c) (d)

Figure 5.3: (a) The wrapped HARP phase to be unwrapped; (b) Unwrapping done without branch cuts and using the Quality-guided method; (c) Unwrapping done by introducing wrong branch cuts; (d) Correctly unwrapped image by introducing the correct branch cuts.

5.3.2 Least-squares Methods

The second major approach to phase unwrapping is the application of a mathematical formalism to reduce the problem to a least-squares method [97]. There are both weighted and unweighted procedures for achieving the same. In the least-squares methods, the gradient field is determined from the wrapped phase differences of the wrapped phase data and is then integrated subject to the constraint of a smooth field. This calls for the minimization of

$$\|\nabla\phi - W[\nabla\psi]\|_2^2\,, \tag{5.6}$$

where ϕ is the unwrapped phase. It can be shown that the minimizer in Equation (5.6) is the solution to a Poisson equation

$$\nabla^2\phi = \nabla \cdot W[\nabla\psi] \quad \text{on} \quad \Omega \tag{5.7}$$

with appropriate boundary conditions Ω. Hunt's matrix formulation [107] is used to convert Equation (5.7) to a discretized Poisson equation of the form

$$(\phi_{i+1,j} - 2\phi_{i,j} + \phi_{i-1,j}) + (\phi_{i,j+1} - 2\phi_{i,j} + \phi_{i,j-1}) = \rho_{i,j}, \tag{5.8}$$

where

$$\rho_{i,j} = (\delta^x_{i,j} - \delta^x_{i-1,j}) + (\delta^y_{i,j} - \delta^y_{i,j-1})$$

and $\delta^x_{i,j}$ and $\delta^y_{i,j}$ are wrapped phase differences i. e. discretized versiion of the x and y components of the gradients at pixel (i, j). The discrete cosine transform (DCT) is the most

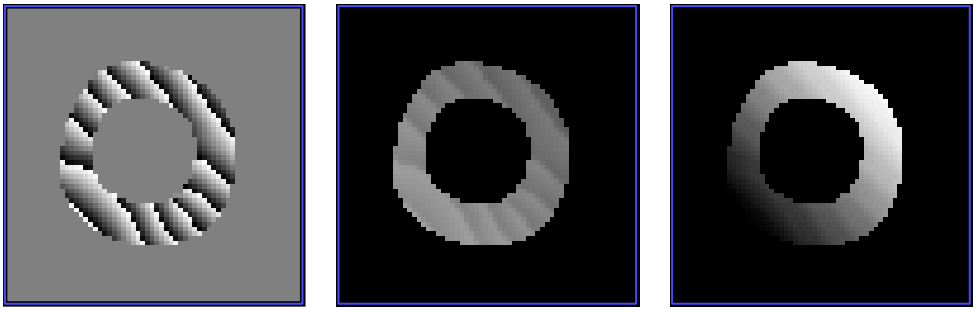

(a) (b) (c)

Figure 5.4: (a) The wrapped HARP phase to be unwrapped; (b) The phase after unwrapping using the DCT method; (c) The unwrapped phase image using the Preconditioned Conjugate Gradient method of unwrapping. The PCG algorithm uses weights to mask out the myocardium unlike the DCT algorithm.

popular method used to solve the discrete Poisson equation of Equation (5.8). It is computationally efficient since it is based on the DCT algorithm which is both memory efficient and very fast. It is also easy to implement as it does not require any prior information (quality map, identify residues etc.). The DCT algorithm can be described as follows:

1. Compute the array of values for $\rho_{i,j}$ as in Equation (5.8)

2. Compute the two-dimensional DCT of $\rho_{i,j}$ to get $\hat{\rho}_{i,j}$

3. Replace the values in $\hat{\rho}_{i,j}$ to obtain $\hat{\phi}_{i,j}$ as in Equation (5.9). This makes it memory efficient.

$$\hat{\phi}_{i,j} = \frac{\hat{\rho}_{i,j}}{2\cos(\pi i/M) + 2\cos(\pi j/N) - 4} \tag{5.9}$$

4. Compute the two-dimensional inverse DCT of $\hat{\phi}_{i,j}$ to get $\phi_{i,j}$, the unwrapped phase

The preconditioned conjugate gradient (PCG) method is an improvement over the DCT method in that it allows the user to give a weight matrix so that the user can supply the quality map that describes the areas with high signal-to-nose-ratio. The algorithm works iteratively by use of the full-lattice solution [89] as the preconditioner in the conjugate

gradient algorithm. The full-lattice problem is solved every iteration using the DCT method. In our case, the segmented myocardial pixels were designated the value of highest quality of one, and the others were designated to zero.

The results for the two implementations of the least-squares methods using the DCT and PCG methods are as shown in Figure 5.4(b) and Figure 5.4(c) for a wrapped phase given in Figure 5.4(a). The data points only inside the myocardium have been shown for the sake of easier analysis. It is clear that the PCG method performs better than the DCT method. The PCG method is fast and is a good choice compared to the DCT method, as it gives a more accurate solution. The problem is that this algorithm is sensitive to large inconsistencies in the data (large amount of residues) and does not always provide a solution that allows for pixel-accurate measurements. It was tested on tagged MR images, and it showed artifacts in the unwrapped phase images that reduce its usefulness.

A significant problem experienced with the least-squares methods is that an integral multiple of 2π is not necessarily added to ensure smoothness and this may lead to unwanted smoothing and increased differences between the original and obtained results. Least-squares methods show better performance than path-following methods when the data to be used is very noisy and shows little or no aliasing. The data used in this research generally has high SNR inside the area of interest (the myocardium) and the major problem as opposed to noise is aliasing. The unwrapped phase data that we require also needs to be highly precise to get pixel-accurate displacement measurements. Least-squares approaches are therefore not pursued.

5.4 Conclusion

The chapter reviewed the basics of phase unwrapping and how the different methods work on HARP images [108]. It has been recognized that residues caused mostly by phase aliasing are the major hurdle facing unwrapping the HARP images. It is important to realize that the residues occur when one can notice two wrapped phase lines (those that occur when

there is $-\pi$ to π shift) merge together or when a wrapped phase line ends prematurely. This is an important concept that shall be utilized later.

It has been shown that the path-following methods are a better choice than the least-squares methods at least when the input phase has a fairly high SNR. The quality-guided method did not account for any residues present in the image. The residue-compensation method, while being more unpredictable, also produces more accurate unwrapped phase maps in the presence of residues when the branch cuts are placed correctly. In Chapter 6, we explore the placement of branch cuts in harmonic phase images and in Chapter 9 we automate this procedure.

Chapter 6

3D Left Ventricular Strain from Unwrapped Phase: A GUI-based approach

6.1 Introduction

Parameters of cardiac left-ventricular (LV) mechanical function are important for diagnosing and managing patients with heart disease and assessing the efficacy of therapies over time. Imaging methods based on magnetic resonance (MR) tagging [11, 79] and displacement encoding with stimulated-echoes (DENSE) [82, 88] have been used to study the regional functional characteristics of the heart. While recent advances in imaging methods [27, 85–87] and post-processing techniques [49, 77] have improved the clinical viability of these techniques, the ability to provide dense 3-D strain maps and torsion measurements throughout the cardiac cycle in a reasonable amount of time is still an active area of research.

Tagged MRI is an established method for measuring parameters of LV deformation and strain. Tagged MRI spatially modulates the longitudinal magnetization of the underlying tissue before image acquisition. The result is a periodic tag pattern that deforms with the tissue as shown in Figure 6.1a. Several techniques have been developed to measure LV deformation and strain from the deformation of the tag pattern. These techniques include feature-based (FB) methods [14, 44–47] , optical-flow and non-rigid registration based methods [43, 70, 78, 109] , and HARP-based methods [27, 49, 51, 52].

In HARP analysis, the tag pattern deformation is measured by the local change in phase of the tag pattern. The tag pattern modulates the signal intensity of the image, producing a series of peaks in the Fourier domain as shown in Figure 6.1b. One of these peaks is filtered out and inverse Fourier transformed to produce a HARP phase image as shown in Figures 6.1c and 6.1d. The HARP phase at a point in the image is a material property of the underlying tissue and can be tracked through the image sequence or used to compute

2-D strain [49, 50] or 3D strain in the middle third of the LV wall [27]. The HARP phase, however, is wrapped because it can only be measured modulo 2π. This wrapping can cause tracking problems if a region of the tissue deforms more than one-half tag spacing i.e. a phase shift of more than π between time frames. Deformations of this magnitude are possible in both healthy and diseased hearts.

In DENSE imaging [83, 110], myocardial tissue displacement is encoded into the phase of the MR image during acquisition. To reconstruct myocardial displacement from the phase data, the phase must be unwrapped [82, 83, 110], which involves adding integer multiples of 2π to the wrapped phase so that the unwrapped phase is continuous. Noise and imaging artifacts, however, can cause phase inconsistencies where no integer multiple of 2π can yield a continuous unwrapped phase map. While DENSE phase unwrapping continues to improve [88,110], it is still possible for phase errors to occur, which can result in errors in deformation and strain estimates.

In this chapter, a new method is presented for measuring 3D deformation and strain from tagged MRI data based on unwrapping HARP images called Strain from Unwrapped Phase (mSUP). In contrast to a recently-proposed 3D wrapped-phase based method in [27], the mSUP algorithm can measure strains in the entire LV. The mSUP algorithm can also easily measure 3D strains in the entire LV wall over multiple time frames. The mSUP approach is more robust to inter-frame motion than techniques such as [27] that are based on tracking wrapped phase. With unwrapped phase, points can be tracked through an image sequence as long as the average inter-frame deformation over the entire myocardium is less than one-half tag spacing. Compared to methods based on tracking tag lines [14, 111], displacement measurements from unwrapped HARP phase images are dense, potentially resulting in more accurate estimates of strain.

6.2 Materials and Methods

6.2.1 Human Subjects

The mSUP algorithm was validated on a cohort of 40 human subjects (10 normal volunteers, 10 patients with myocardial infarction, 10 patients with mitral regurgitation, and 10 patients with hypertension). All human studies were approved by the Institutional Review Boards of both institutions (Auburn University and University of Alabama at Birmingham) and informed consent was obtained from all participants.

6.2.2 Data Acquisition

All participants underwent MRI on a 1.5T MRI scanner (GE, Milwaukee, WI) optimized for cardiac application. Tagged images were acquired in standard views (2-chamber and 4-chamber long-axis and short-axis) with a fast gradient-echo cine sequence with the following parameters: FOV = 300 mm, image matrix = 224x256, flip angle = 45, TE = 1.82ms, TR = 5.2ms, number of cardiac phases = 20, slice thickness = 8 mm. A 2D fast gradient recalled spatial modulation of magnetization (FGR-SPAMM) tagging preparation was done with a tag spacing of 7 pixels. This protocol resulted in 2 long-axis slices and on average, 12 short-axis slices per study.

6.2.3 Unwrapping HARP Phase

HARP images [49] were obtained by filtering out a single spectral peak in a tagged image and computing the phase in each pixel of the resulting complex-valued image. These phase images are wrapped because phase can only be computed modulo 2π. Phase unwrapping involves adding integer multiples of 2π to each pixel in the wrapped image so that:

1. The unwrapped phase is continuous.

2. If the unwrapped phase is re-wrapped, the result is equivalent to the original wrapped image.

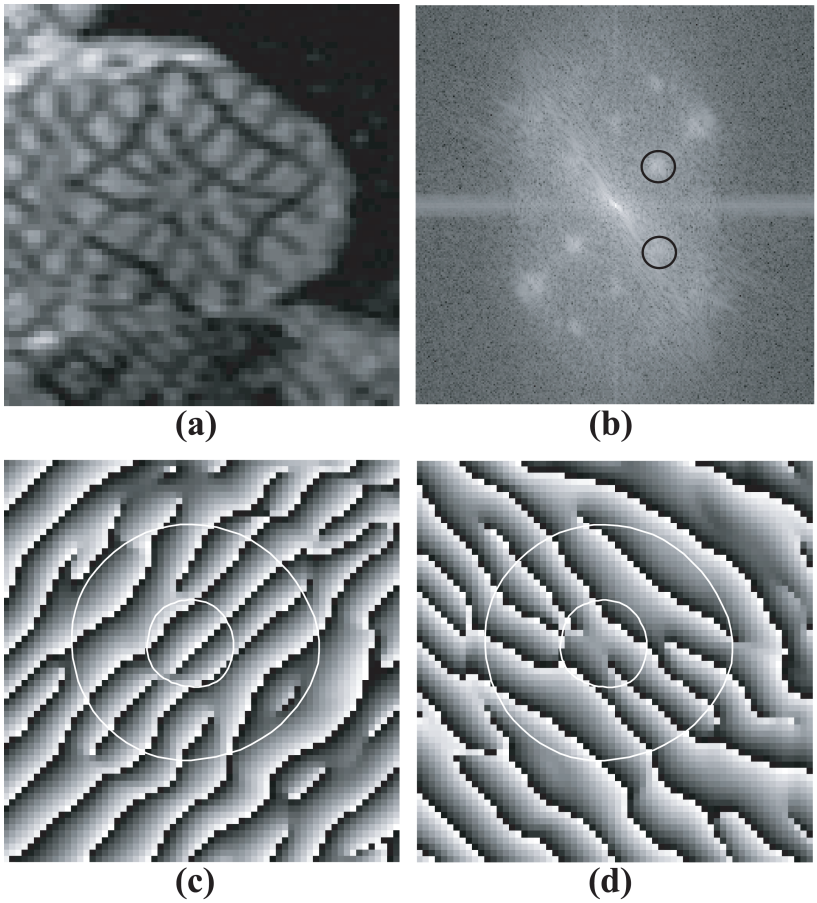

Figure 6.1: (a) A tagged short-axis image acquired near end-systole in a normal human; (b) the Fourier transform log-magnitude of (a); (c) HARP image obtained by bandpass filtering the lower circle in (b); (d) HARP image obtained by bandpass filtering the upper circle in (b).

The relationship between the wrapped phase and the unwrapped phase may be stated as

$$\psi(x,y) = \mathrm{mod}\ \{[\pi + \phi(x,y)], 2\pi\} - \pi, \quad -\pi < \psi(x,y) < \pi \tag{6.1}$$

where W is the wrapping operator. In this research, phase was unwrapped only inside the LV wall. Pixels outside the myocardium were not processed.

Several phase-unwrapping algorithms have been proposed for MRI and other applications [89] (see Chapter 5). In particular, DENSE post-processing involves unwrapping the DENSE phase maps [82, 84, 88]. In this research, a path-following method was used that is similar to the one used for DENSE in [82, 89], where phase was unwrapped along a path in the image from one pixel to another. If the phase is unwrapped correctly, the phase of the destination pixel is independent of the path taken. Two main issues arise with this approach: how to choose the path and how to handle regions of inconsistent phase. The path was chosen by the quality-guided method described below. Phase inconsistencies are called residues. These were handled by introducing branch cuts. These methods are described in detail in the following sections.

6.2.4 Quality-Guided Phase Unwrapping

In path-following methods, it is necessary to determine a path that visits each pixel of interest. The phase is unwrapped along this path. Quality-guided algorithms [100] use a quality map, which indicates the reliability of the wrapped phase map at each pixel, to guide the integration path. A starting point was arbitrarily chosen and the next pixel visited was the neighbor with the highest quality. This process was repeated until all pixels of interest were processed. Similar to DENSE [82] algorithms, quality in this research was defined as the reciprocal of the phase difference variance [112], which is given by

$$z_{m,n} = \frac{\sqrt{\sum (\delta^x_{i,j} - \overline{\delta^x_{m,n}})^2} + \sqrt{\sum (\delta^y_{i,j} - \overline{\delta^y_{m,n}})^2}}{9} \tag{6.2}$$

where each sum is over a 3×3 window, centered at the pixel (m, n). The terms $\delta^x_{i,j}$ and $\delta^y_{i,j}$ are the wrapped phase derivatives, and $\overline{\delta^x_{m,n}}$ and $\overline{\delta^y_{m,n}}$ are the average of the derivatives in the 3×3 window.

6.2.5 Residues and Branch Cuts

A fundamental assumption in phase unwrapping algorithms is that the unwrapped phase is smooth and that any large changes in phase between pixels are due to phase wrapping. Noise and artifacts, however, can cause inconsistencies in the phase map where the phase difference between pixels is large and cannot be corrected by adding an integer multiple of 2π. Tag fading, myocardial motion, and the presence of boundaries can also cause phase inconsistencies. Examples of phase inconsistencies are shown in Figure 6.2. +45 degree tag lines disappear before they reach the endocardium at 12 o'clock and 5 o'clock in Figure 6.2c. Also the tag-like phase wrap near the epicardium at 4 o'clock in Figure 6.2c is caused by the epicardial boundary. Figure 6.2d shows a "double wrap" artifact where two tag lines merge (7 o'clock).

Phase inconsistencies can cause any phase-unwrapping algorithm to fail. Figure 6.3a shows an example of a phase image with inconsistencies. Figure 6.3b shows the unwrapped phase image obtained with the technique described above. The phase inconsistencies result in discontinuities in the unwrapped phase. In this section we present a method for detecting and correcting for phase inconsistencies using residues and branch cuts.

Phase inconsistencies were detected using the principle that the wrapped phase difference around any closed path is equal to zero if the wrapped phase is consistent [89]. Consequently, these phase inconsistencies were localized by summing the wrapped phase differences around a 2×2 neighborhood of each pixel in the myocardium. It can be shown [89] that this sum is either $0, +2\pi$, or -2π. If the sum is zero, then no phase inconsistency exists. Otherwise, either a positive residue ($+2\pi$) or a negative residue (-2π) is present at that pixel. Examples of residues can be seen in Figures 6.2e and 6.2f.

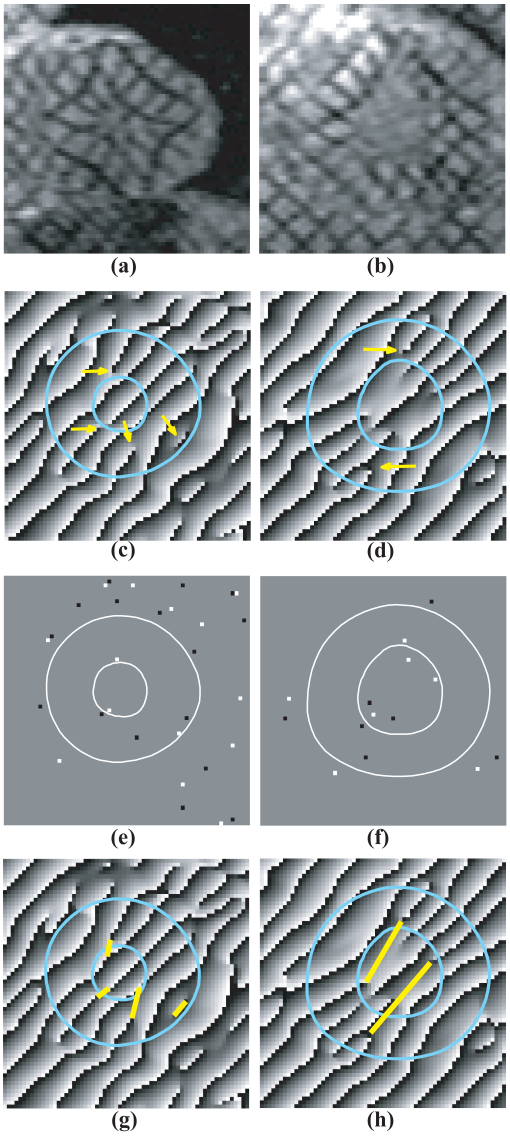

Figure 6.2: (a-b) Tagged short-axis images acquired near end-systole in two different human subjects; (c-d) HARP images obtained from a and b. Arrows indicate points of phase discontinuity. Cyan contours delineate the myocardium; (e-f) negative (black) and positive (white) residues in the HARP images in (c-d); (g-h) the corresponding HARP phase image with branch cuts drawn (yellow lines).

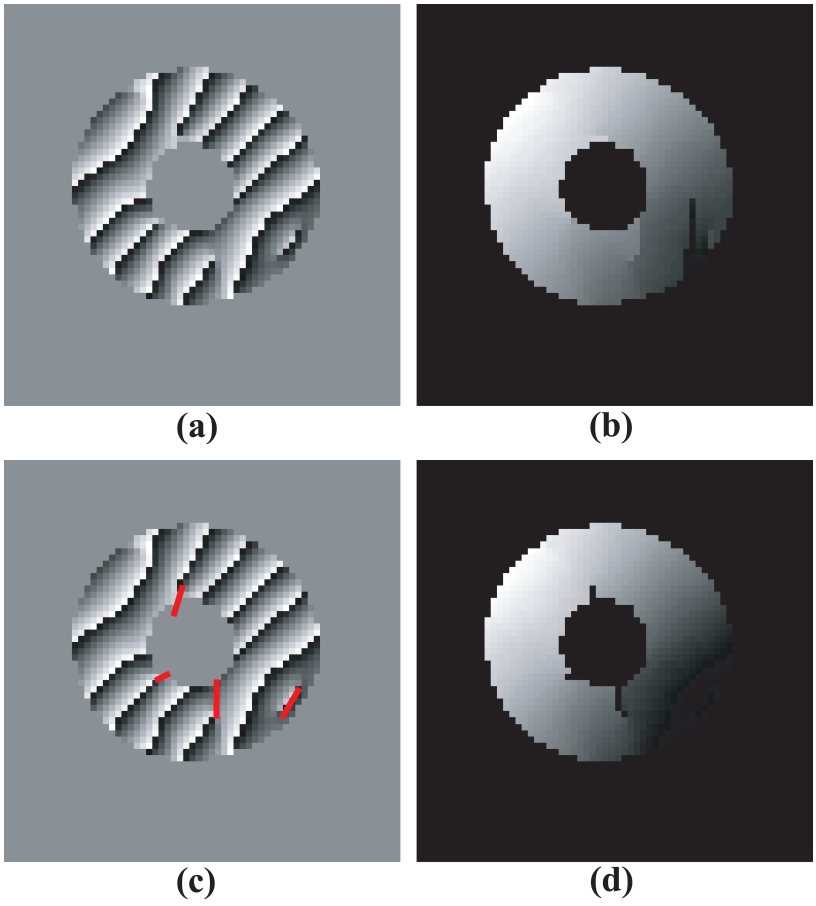

Figure 6.3: Phase Unwrapping example in a short-axis slice of a normal human left ventricle: (a) wrapped HARP phase from Figure 2c; (b) unwrapped HARP image without branch cuts; (c) HARP image with branch cuts shown in red (d) unwrapped HARP image with branch cuts.

In this research, phase inconsistencies were corrected using the residue compensation method [89], where residues were removed by connecting residues with branch cuts. Branch cuts are lines in the image where an unwrapping path is not allowed to cross. In our implementation, pixels that touch the branch cut line were removed from the myocardium segmentation. Note that the number of pixels removed due to branch cuts is negligible compared to the total number of pixels used in the 3D deformation model fit described below.

Branch cuts either connect a positive to a negative residue or, if only a region of the image is unwrapped, a residue is connected to a point outside the myocardium segmentation. The problem, of course, is which residues to connect. It is common to see positive and negative residues next to each other in the image (see Figure 6.2e). These residues are known as dipoles and can be automatically connected by a branch cut.

Connecting non-dipole residues (called monopoles), however, is a difficult problem. In cases where there are an equal number of positive and negative residues, automated methods have been proposed that, for example, minimize the average branch cut length [89, 106]. Minimizing branch-cut length, however, does not always yield the best unwrapped phase. As a result, the user must place the branch cuts interactively. This was done quickly with a graphical user interface (GUI).

Figures 6.2g and 6.2h show branch cut placement examples. The phase wraps in the second row of Figure 6.2 correspond to the +45 direction tag lines. If the phase inconsistency was caused by a prematurely ending tag line (11 o'clock and 5 o'clock in Figure 6.2c) or tag line merging (7 o'clock in Figure 6.2d), the branch cuts were placed along the missing or merged tag line. If a phase wrap occurred where there was no tag line (4 o'clock in Figure 6.2c) the branch cut was placed to remove the spurious phase wrap from the myocardium segmentation.

Once branch cuts were placed, the phase unwrapping technique described above resulted in a smooth unwrapped phase map as shown in Figure 6.3d. Note that after branch cuts

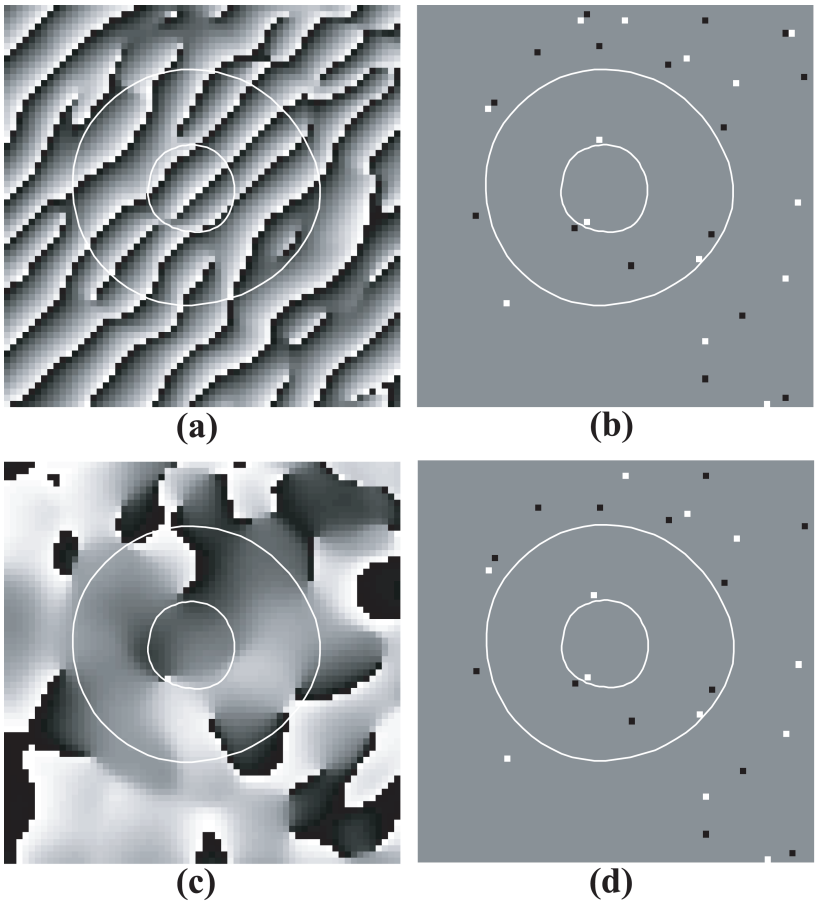

Figure 6.4: (a) HARP image; (b) negative (black) and positive (white) residues in the HARP image in (a); (c) the corresponding demodulated HARP phase image; (d) residues in the demodulated HARP image in (c).

are placed, the unwrapped phase is independent of the path taken during the unwrapping process.

6.2.6 Demodulated HARP Phase

Instead of unwrapping the HARP phase image, one could unwrap the demodulated HARP phase image. The demodulated HARP phase image is computed by shifting the filtered HARP peak to the center of k-space before computing the inverse Fourier transform. Figures 6.4a and 6.4c show the HARP phase and demodulated HARP phase images of the tagged image in Figure 6.2a. The demodulated HARP phase is similar to the phase obtained with DENSE imaging [113]. At first, it might appear that the demodulated phase is easier

to unwrap than the modulated HARP phase because there are fewer phase wraps. Phase wraps, however, are usually not a problem for phase unwrapping algorithms. The challenge in phase unwrapping is how to handle phase inconsistencies. Since phase inconsistencies are mainly caused by tag lines disappearing, tag lines merging, myocardial boundaries and other inherent properties of the tissue being imaged, they appear in both the HARP phase and demodulated HARP phase images. For example, Figures 6.4b and 6.4d show the residues for both the HARP phase and demodulated HARP phase images. The residues in both images are almost identical. While either the HARP phase or demodulated HARP phase image could be unwrapped, the HARP phase image was used in this research because the phase wraps correspond to tag lines and provide visual cues that make it easier for the user to place branch cuts as seen in Figure 6.3c.

6.2.7 Inter-frame Phase Consistency

Each image was unwrapped independently, and the starting point for phase unwrapping may correspond to a different material point in each image. As a result, the unwrapped phases in two adjacent time frames may differ by an integer multiple of 2π. This difference was corrected by adding the integer multiple of 2π to all unwrapped phases in the current time frame. In this research, the multiple was chosen to minimize the $L1$ norm of all displacements between the current and previous time frames. Note that this correction assumes that the average deformation of the heart between consecutive frames is less than one-half of the tag spacing. Inter-frame deformation of more than one-half tag spacing in a localized region or regions will not affect the unwrapped phase as long as the average deformation is less than one-half tag spacing.

6.2.8 Motion and Strain Estimation

Calculating 1-D Displacement Measurements

Once the phases were unwrapped, 1-D displacements were measured from each pixel in the myocardium similar to those measured from tag-line tracking data [14]. Each 1-D displacement measurement is the displacement of a material point back to its reference position in the direction normal to the tag plane. As in [13, 14, 114], we define the reference time to be the time the tag pattern was applied. Note that this time is several milliseconds before the first image is acquired.

To compute the 1-D displacements, an estimate of the reference phase plane must be computed. The reference phase plane was estimated by fitting a plane to the unwrapped phase plane in the first time frame in a given slice. This computation is analogous to the one performed in [13, 14, 114] to determine the tag line center and spacing. There can be some motion between the time the tags are applied and the acquisition of the first image, but this is usually small. Since tag lines are parallel when they are applied, the reference phase plane was specified by the 1-D linear equation

$$\phi_r = ms + b \tag{6.3}$$

where s is a parameter that sweeps out a line perpendicular to the tag line and m and b are parameters of the reference plane fit to the first time frame unwrapped phase.

To compute the 1-D displacement measurements, let s_d correspond to a point in a deformed image with phase $\phi_d(s_d)$. From Equation (6.3), the point in the reference image with the same phase is $s_r = (\phi_d(s_d) - b)/m$. The displacement measurement is then $d = s_d - s_r$. Figure 6.5 shows an example of displacement estimates measured from a short-axis slice of a normal human volunteer at end-systole. Note that due to through-plane motion a 1-D displacement does not establish a one-to-one correspondence between points at the

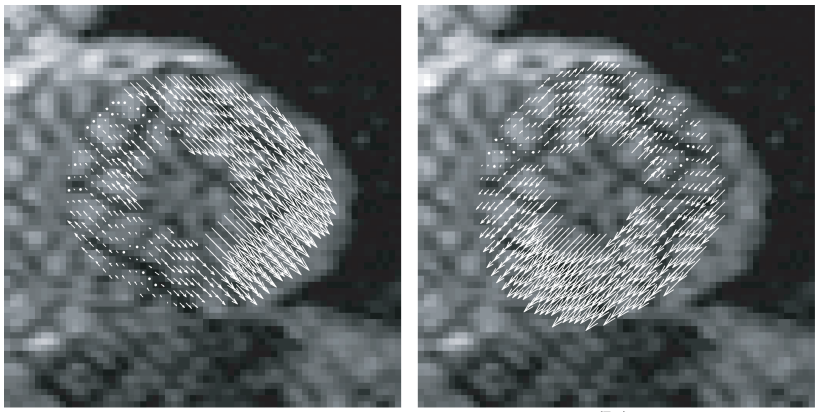

Figure 6.5: 1-D displacement vectors superimposed for (a) the +45 and (b) -45 tag directions. The arrows point to the position of the points at the time of tag line imposition.

reference and deformed times. Rather, it is a 1-D constraint on the 3-D displacement of a material point back to its position in the reference time [13, 14, 114].

Segmentation

Segmentation of the myocardium is the first step in most cardiac image analysis procedures [44, 50, 82]. Both the phase unwrapping and displacement measurement steps require that the LV wall be segmented in each slice and time of interest. In this algorithm, LV contours were drawn semi-automatically by the user at end-diastole (ED) and end-systole (ES). Non-rigid registration [115] was then used to propagate ED and ES contours to all the time frames. ED contours are used in almost all tagged MRI analysis algorithms to define a material-point mesh or other set of points of interest. ES contours were included because they improve the ability of the propagated contours to distinguish between papillary muscles and the LV wall.

Strain Calculation

The 1-D displacement measurements and a material-point mesh automatically constructed from the ED contours were used to compute 3-D LV deformation and strain in

each time frame. The deformation and strain were reconstructed using the Affine Prolate Spheroidal B-Spline (APSB) method in [116], which fits a B-spline deformation model defined in prolate-spheroidal coordinates to the displacement measurements. First, a backward fit was performed in each time frame that maps each point back to its undeformed position. A series of forward fits were then performed to compute the deformed position of each point in the undeformed mesh of the initial time frame. The trajectory of each point in the material-point mesh through the cardiac cycle is thus obtained. 3-D strain was computed by spatially differentiating the deformation model.

Validation Experiments

The mSUP technique was validated on the cohort of 40 human subjects described above. In each subject, 3D strain was computed in all imaged time frames using the mSUP technique. 3D strain was computed at end-systole (ES) with the feature-based (FB) technique in [116]. Both the FB and mSUP methods use the APSB deformation model described in [116]. The tags were tracked using the FB technique and then manually corrected by an expert. 2D strain in each time frame was computed using HARP analysis [117].

To assess the accuracy of 1D displacement measurements obtained from unwrapped phase images, 1D displacement measurements were computed from tag lines tracked in the FB method and compared to 1D measurements computed from the unwrapped phase images at the tracked tag line points. The accuracy of 3D strains at end-systole was assessed by comparing mSUP strains and FB strains with a paired t-test. The accuracy of strains versus time was assessed by comparing peak strains and strain rates computed using mSUP and HARP with paired t-tests. In all statistical comparisons, a P value of 0.05 or less was considered statistically significant.

6.3 Results

6.3.1 Computation Time

All studies were processed using the mSUP technique described above, which was implemented in MATLAB (The Mathworks Inc, Natick, MA). Unwrapping all images in a study took less than a minute on a 2.6GHz Core2 Duo processor with 4 GB of memory. Approximately 30 minutes per study of user interaction were required to resolve residues. Strain reconstruction took approximately 15 minutes per study. The total time required to analyze 20 time frames of a typical study was 45 minutes.

6.3.2 Quantitative Comparisons

Comparison of Displacement Estimates with Feature-Based Technique

Table 6.1 shows statistics of the differences between 1D displacement measurements computed from unwrapped phase images and tracked tag lines at end-systole. The mSUP and tag line methods showed excellent agreement on long-axis images and short-axis images in the proximal and middle thirds of the LV (relative to the base). The mean differences are a few hundredths of a pixel, which means there is no bias toward under- or overestimation of displacement. The difference standard deviation is around 1/3 of a pixel, which is close to the tag line tracking accuracy [114, 118]. In three slices at or next to the apex, (out of a total of 429 processed) the maximum difference was large (≈ 8 pixels) due to partial volume effects that severely diminished the contrast-to-noise ratio (CNR). These slices were removed from the differences in Table 6.1, but left in for the comparison of strains in subsequent comparisons.

Comparison of End-Systolic Strains with Feature-Based Technique

Figure 6.6 shows the maps of 3D circumferential strain (Ecc) in a representative normal human volunteer computed using mSUP and the FB method. The same material-point mesh

Table 6.1: Comparison of displacement measurements computed from mSUP at tracked tag lines at end-systole. Proximal, middle, and distal refer to the LV base. Difference = mSUP - tag line. All measurements are in pixels. RMSE = root mean squared error.

Slices	Mean Diff.	Std. Dev.	Max. Diff.
All slices	0.0012	0.3963	
4-Chamber	-0.0263	0.3364	2.0479
2-Chamber	0.0052	0.3349	2.7517
Short-axis Proximal 3rd	-0.017	0.3572	2.5694
Short-axis - Middle 3rd	-0.0217	0.3299	2.4348
Short-axis Distal 3rd	0.0787	0.5625	2.9898

and deformation model were used to reconstruct strain in both methods. Note that strain is computed in the entire LV except the apex, which is typically not included in this type of analysis. The strain maps are similar.

Table 6.2 shows statistics of the difference between the mSUP and FB methods. In all strains in Table 6.2, the standard deviation of the difference is less than 5% of the average of the two methods. The correlation between the methods is strongest in circumferential strain. Only two long-axis images were acquired, so the correlation in longitudinal strain (Ell) and torsion is lower but still good. In fact, the mSUP method may provide more accurate measurements of Ell, torsion and other strains than the FB method, but further investigation is needed to support this claim.

Table 6.2: Comparison of 3D, end-systolic strains computed from strain from unwrapped phase (mSUP) and feature-based (FB) methods. Differences = mSUP-FB. Differences = Mean ± Standard Error. ρ = Correlation coefficient. CV = coefficient of variation. Ecc = Circumferential shortening strain. Ell = Longitudinal shortening strain. Emin = Maximal shortening strain.

Strain	Differences			p	ρ	p	CV
Ecc	0.0009	±	0.0017	0.9105	0.9613	<0.001	2.04%
Ell	-0.0022	±	0.0019	0.7752	0.9351	<0.001	2.88%
Emin	-0.0028	±	0.0019	0.6717	0.9201	<0.001	1.59%
Torsion	-0.3498	±	0.2251	0.5757	0.8697	<0.001	3.66%

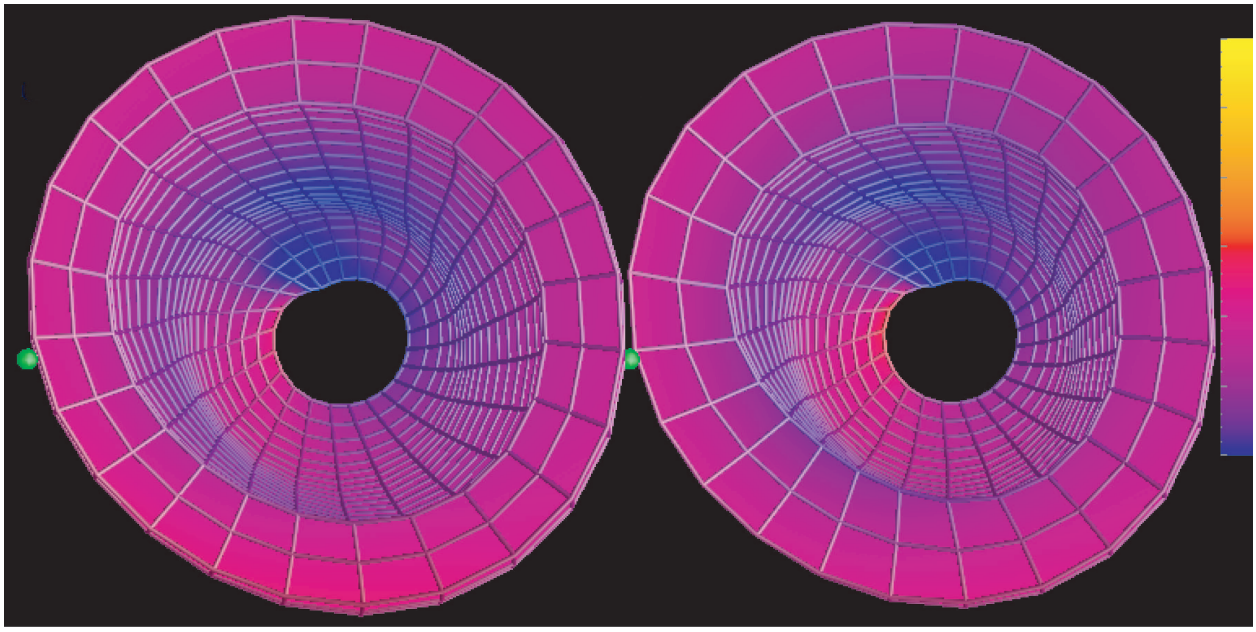

Figure 6.6: Maps of circumferential strain (Ecc) using feature-based (left) and unwrapped phase (right) methods. Strains are mapped from blue = -30% to yellow = +30%. The green balls denote the basal mid septum.

Comparison with HARP Strains

Table 6.3 shows statistics of the difference between the 3D strains calculated from mSUP and the 2D strains from the HARP method [117]. 2D LV torsion using HARP was measured using the procedure described in [51]. One slice each at the basal and apical levels was used to compute torsion. The basal slice chosen was the slice closest to and below the mitral valve at the end-systolic (ES) phase. The apical slice chosen was the slice closest to the apex where the blood pool could be identified. A mesh consisting of 3 concentric rings and 24 circumferential points was defined in each slice at end-diastole (ED) from semi-automatically-drawn contours. Each mesh was tracked through all time frames using the improved harmonic phase (HARP) method for motion tracking [52].

The peak strain and systolic strain rate of the measured circumferential strain show a high correlation. Correlation in longitudinal strain is lower because the mSUP method uses 3D deformation model fitting to compute longitudinal strain from the motion of all tag points, whereas HARP computes strain from two long-axis images. Also, the tag line CNR

decreases through the cycle due to T_1 decay of the tag pattern, so early diastolic correlations are lower than correlations for peak strain and systolic strain rate. It was seen that HARP in general underestimated the strains as compared to the mSUP method. This could be attributed to the improved accuracy of tracking using the mSUP method as a result of removal of inconsistencies in the HARP image using branch cuts.

A few degrees of difference was seen in comparison of peak torsion. The 3D method corrects for the through-plane motion, but the 2D method tracks points in a given slice through time. In the 2D method, the tracked points in the basal slice start out near mid-ventricle and become more basal through systole. Since the base typically rotates more than the mid-ventricle, though-plane motion can distort the 2D rotation and torsion curves.

Table 6.3: Comparison of strains and torsion using the strain from unwrapped phase (mSUP) and HARP methods. Difference = mSUP - HARP. Differences = Mean ± Standard Error. ρ = Correlation coefficient. CV = coefficient of variation. Ecc = Circumferential shortening strain. Ell = Longitudinal shortening strain.

Strain	**Differences**			**p**	ρ	**p**	**CV**
Ecc							
Peak Strain	-0.0223	±	0.0005	0.004	0.8361	<0.001	3.91%
Systolic Rate	-0.1004	±	0.0024	0.011	0.8387	<0.001	3.49%
Early-Diastolic Rate	-0.0494	±	0.0068	0.502	0.6615	<0.001	8.10%
Ell							
Peak Strain	-0.0217	±	0.0005	<0.001	0.7023	<0.001	4.93%
Systolic Rate	0.0657	±	0.0042	0.132	0.624	<0.001	6.41%
Early-Diastolic Rate	-0.2091	±	0.0111	0.052	0.5739	<0.001	12.77%
Torsion							
Peak Torsion	-0.0036	±	0.1092	0.998	0.6567	<0.001	7.00%
Systolic Rate	-9.4941	±	0.5079	0.069	0.649	<0.001	7.053
Early-Diastolic Rate	3.9996	±	0.8812	0.533	0.2578	0.108	10.41%

6.3.3 mSUP Strains in Normals and Patients

Figure 6.7 shows plots of torsion versus time averaged over 10 normal human volunteers, 10 patients with myocardial infarction, 10 patients with hypertension and 10 patients with mitral regurgitation. The hypertensive patients showed an increase in torsion, which has

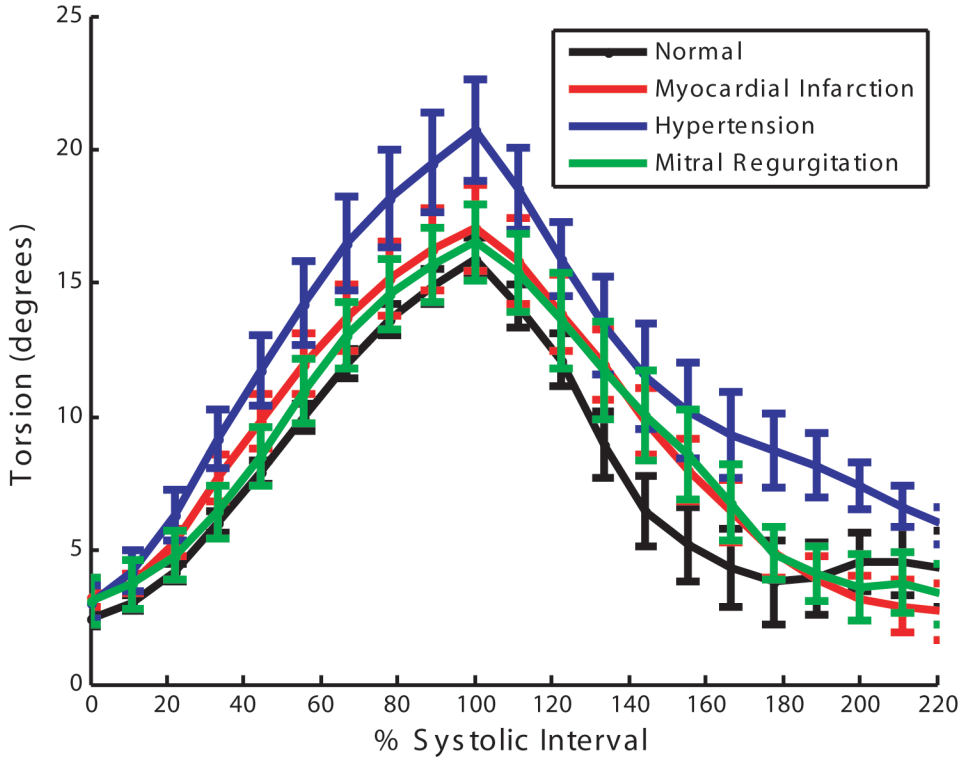

Figure 6.7: Torsion angle (rotation of the apex relative to the base) versus % systolic interval averaged over 10 normal human volunteers, 10 patients with myocardial infarction, 10 patients with hypertension and 10 patients with mitral regurgitation. Error bars represent ± one standard error.

been reported in the clinical literature [39]. The untwisting in early-diastole was slower for patients with mitral regurgitation as compared to normal human volunteers, which is consistent with previously reported results [119].

6.4 Discussion

The mSUP method was presented for measuring 3D strain from tagged MRI. Strains computed using mSUP demonstrate excellent agreement with a previously published feature based method. Some user interaction is also required to resolve phase-unwrapping residues (especially later in the cycle), but the mSUP method can compute strains in the entire LV instead of just the middle third.

The time required for the mSUP-measured 3D strains in the entire LV over 20 time frames is approximately 45 minutes per study. The same analysis using the feature-based method would require approximately 3 hours.

While the tagged imaging protocol used in this research is commercially available and is widely used clinically, advanced tagged imaging techniques such as Complementary SPAMM, can yield a higher tag CNR throughout the cardiac cycle. Higher CNR images will result in fewer phase inconsistencies, and less user interaction will be required to correct them.

The use of residues to automatically detect phase inconsistencies in wrapped phase images and the use of branch cuts to correct them can also be used in unwrapping the phase in DENSE imaging.

Spottiswoode et al. [82] used a spatio-temporal method of phase unwrapping to maintain inter-frame phase consistency in DENSE images, where a group of pixels are selected in the first time frame and these pixels are sequentially unwrapped in each successive time frame. This technique works well in DENSE images because there are only a few phase wraps across the myocardium. The mSUP method, however, is based on HARP images, which make it easier to place branch cuts. HARP images have 6-10 phase wraps across the myocardium. Temporal phase unwrapping in HARP images is sensitive to large (greater than one-half tag spacing) interframe displacements. Therefore, we used a method based on the phase of the entire myocardium over time to maintain phase consistency. This allows for local tissue to have displacements greater than one-half tag-spacing between time frames as long as the average deformation of tissue between time frames is less than one-half tag-spacing.

The mSUP technique reconstructs full 3-D strain maps from tagged MR images through the cardiac cycle and takes into account the through-plane motion of the heart. Slice-following DENSE [83], zHARP [86] and HARP-SENC [85] can account for through-plane motion, but these techniques require two breath-holds per slice. In contrast, tagged images can be acquired with multiple slices per breath-hold, which allows the entire LV to be imaged in significantly less time.

In conclusion, the strain from unwrapped phase (mSUP) method can compute 3-D strains in the LV through the cardiac cycle in a reasonable amount of time and user interaction compared to other 3D analysis methods.

Chapter 7

Comparison Of 2D And 3D Torsion Measured From Tagged MRI

7.1 Introduction

Cardiac left ventricular (LV) torsion is the difference between rotation of the apex and base (see Chapter 1). LV torsion can provide important information about both systolic and diastolic myocardial function [120]. In MRI data, torsion is typically measured by tracking an annular mesh in an apical and a basal slice with two-dimensional (2D) HARP analysis [51, 52]. 2D-techniques may not take into account the through-plane myocardial motion that may significantly affect the torsion measurements. In Chapter 6, a method for computing 3D torsion was presented [90]. The purpose of this research is to quantitatively compare 2D and 3D LV rotation and torsion measurements computed from tagged MRI.

7.2 Methods

A group of 40 subjects were imaged consisting of 10 normal volunteers (NRM), 10 diabetics with myocardial infarction (DMI), 9 patients with mitral regurgitation (MRR), and 10 patients with hypertension (HTN). All participants underwent MRI on a 1.5T MRI scanner (GE, Milwaukee, WI) optimized for cardiac application. Both cine and tagged images were acquired in standard views (2 and 4 chamber long axis and short axis) with a fast gradient-echo cine sequence with the following parameters: FOV = 300 mm, image matrix = 224x256, flip angle = 45, TE = 1.82ms, TR = 5.2ms, number of cardiac phases = 20, slice thickness = 10 mm. A 2D spatial modulation of magnetization tagging preparation was done with a tag spacing of 7 pixels.

2D LV torsion was measured using the procedure described in [51]. One slice each at the basal and apical levels was used to compute torsion. The basal slice chosen was the slice closest to and below the mitral valve at the end-systolic (ES) phase. The apical slice chosen was the slice closest to the apex where the blood pool could be identified. A mesh consisting of 3 concentric rings and 24 circumferential points was defined in each slice at end-diastole (ED) from semi-automatically-drawn contours. Each mesh was tracked through all time frames using the improved harmonic phase (HARP) method for motion tracking [52]. Drawing contours and mesh tracking took approximately 5min per study.

3D LV torsion was measured using the method described in chapter 6 [90]. Myocardial contours were semi-automatically drawn at ED and end-systolic (ES) time frames for all slices and then propagated to all time frames [115]. 3D LV deformation in each time frame was computed by fitting the 1D displacement measurements derived from unwrapping the HARP phase in each image to the affine prolate spheroidal B-spline method in [116]. Drawing contours and other processing took approximately 30min per study.

Displacement of the mitral annulus toward the apex during systole was measured by tracking a user-specified point on the mitral annulus through each frame of a 4-chamber view using non-rigid registration [115].

7.3 Results and Discussion

Figure 7.1 shows rotation and torsion versus time curves averaged over the studies in each of the four patient groups. Differences between 2D and 3D curves can be attributed to two factors. First, a few degrees of rotation occur between tag pattern application and the first images. The 3D method corrects for this initial deformation, but the 2D method does not because it is based on tracking points identified in the first image. This factor shifts the 3D curves by a constant angle through time. The second factor is through-plane motion — primarily motion of the base toward the apex during systole and back again during diastole. The 3D method corrects for this motion, but the 2D method tracks points in a given slice

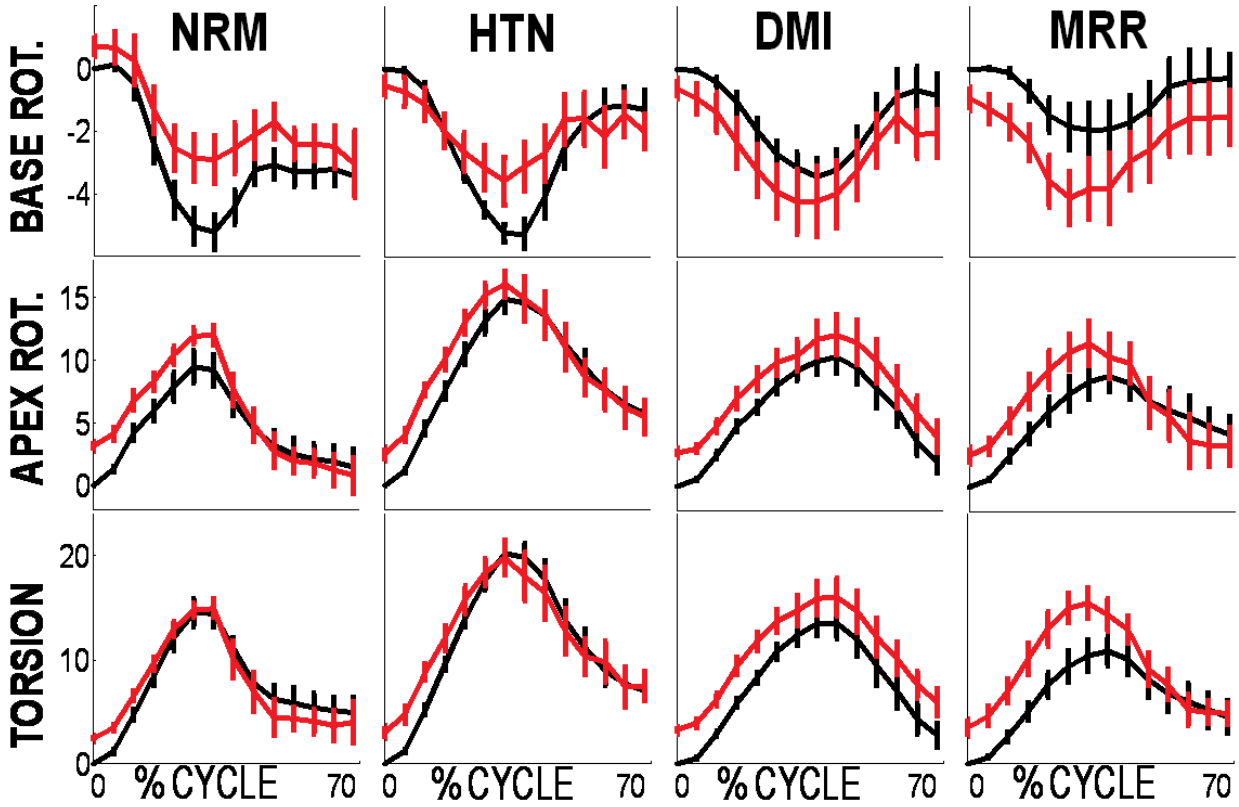

Figure 7.1: Plots of average base and apex rotation, and torsion obtained from 2D (black) and 3D (red) methods through 70% of the cardiac cycle. Error bars represent ± one standard error. All angles are in degrees

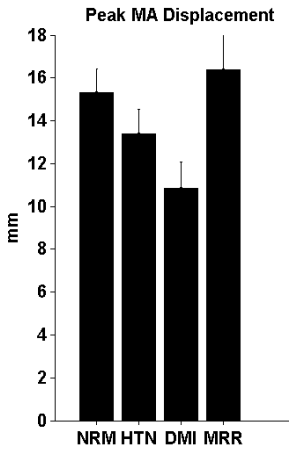

Figure 7.2: Peak mitral annulus displacement.

Table 7.1: Comparison of differences between 3D and 2D rotation and torsion (3D-2D). $*p < 0.05$ relative to 3D.

	Peak (deg)			Sys Rate (deg/s)			Early Dia Rate (deg/s)		
Base Rotation									
NRM	4.3	±	0.8*	7.4	±	4.8	-47.1	±	18.8*
HTN	3.1	±	1.3	7.4	±	6.3	-23.1	±	11.5
DMI	3.1	±	1.1	6.1	±	6	-1.1	±	14.5
MRR	3.9	±	1.4	11.3	±	7.8	-34.6	±	7.4*
Apex Rotation									
NRM	1.9	±	0.4*	6.6	±	2.4	-6.8	±	2.8
HTN	1.3	±	0.8	7.6	±	2.5	-14.4	±	3.8*
DMI	-0.9	±	1	-3.1	±	4.4	2.7	±	3.4
MRR	-2.1	±	0.9	-7.9	±	5.1	6.2	±	4.8
Torsion									
NRM	1.8	±	1	-3.6	±	6.2	-36.3	±	18.2
HTN	1.2	±	1.8	-0.9	±	6.8	-8	±	15.2
DMI	4	±	0.9	9	±	6.3	-7.6	±	13.5
MRR	5.8	±	1.6*	21	±	5.5*	-43.5	±	6.1*

through time. In the 2D method, the tracked points in the basal slice start out near mid-ventricle and become more basal through systole. Since the base typically rotates more than the mid-ventricle, through-plane motion can distort the rotation and torsion curves.

The effect of through-plane motion can be seen by comparing the measurements of mitral annulus displacement (MAD) in Figure 7.2 with the curves in Figure 7.1. The DMI patients have the lowest amount of MAD, and the 3D rotation and torsion curves are shifted versions of the 2D curves. Normals and MR patients have thr largest amount of MAD, and 2D curves are more distorted relative to 3D. Table 7.1 shows the difference between 2D and 3D peak torsion/rotation and peak torsion/rotation rates. The significant differences are primarily in the normal and MR patient groups because of the relatively high through-plane motion.

7.4 Conclusion

While 2D and 3D rotation and torsion measurements are similar in subjects with low base-to-apex motion such as patients with MI, the 3D method measures larger and probably more accurate rotation and torsion in subjects with normal or elevated base-to-apex motion. This may allow improved assessment of cardiac mechanics in patients with a variety of myocardial diseases.

Chapter 8

3D+t Bi-Ventricular Strain using Phase Unwrapped HARP

8.1 Introduction

Accurate measurement of cardiac ventricular mechanical function is important for diagnosing and managing patients with heart disease and assessing the efficacy of therapies over time. The right ventricle (RV) plays a vital role in cardiac function and is adversely affected by many cardiac and pulmonary diseases. Compared to the left ventricle (LV), RV functional analysis is relatively difficult due to its lack of geometric symmetry and relatively thin wall.

Accurate assessment of right ventricular (RV) function is particularly important in patients with pulmonary hypertension (PHTN) and congestive heart failure. Also, in PHTN, relatively higher systolic pressure in the RV can cause excursion of the inter-ventricular septum into the LV cavity (see Figure 8.1a). As a result, the LV cavity can also lose its geometric symmetry, which is assumed in many 3D LV deformation models [7, 29, 65, 69, 121].

In Chapter 6, the strain from unwrapped phase (mSUP) method was presented for computing three-dimensional plus time (3D+t) strain in the LV [90]. The mSUP method is based on unwrapping 2D harmonic phase (HARP) images [49] from tagged MRI and a prolate-spheroidal deformation model [7]. The mSUP strains compared well with strains from 3D feature-based methods [7] and (wrapped) 2D HARP [49], but the prolate-spheroidal deformation model does not fit the RV geometry and is difficult to extend to a biventricular model. The discrete model free (DMF) model proposed by Denney and McVeigh [114], however, is geometry independent and can be easily adapted to biventricular morphology. Also, the unwrapped HARP produces displacement measurements at each pixel, which is useful when estimating the deformation of the thin-walled RV.

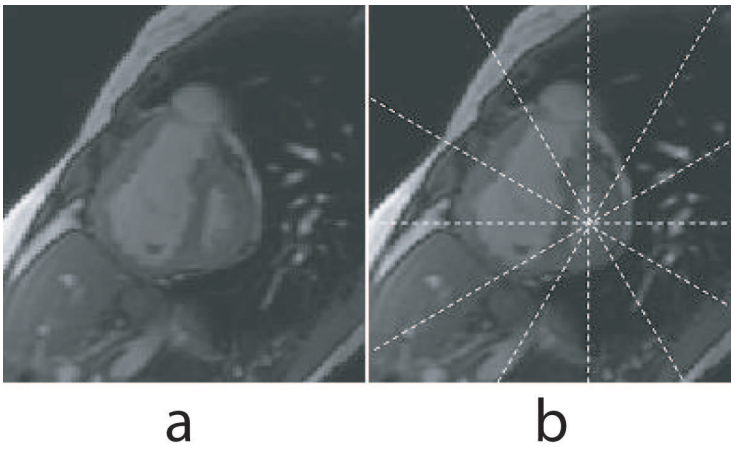

Figure 8.1: (a) Basal short-axis slice of a PHTN patient near end-systole showing RV excursion. (b) Same image with the radially-oriented long axis prescriptions shown.

In this chapter, myocardial displacements from unwrapped HARP in both the RV and LV were used with DMF deformation to reconstruct 3D+t biventricular strain in each imaged time frame through systole and early diastole. We refer to this method as the biventricular strain unwrapped phase (BiSUP) technique. The BiSUP technique produces 3D+t biventricular displacements and strains with minimal manual intervention and with high spatial resolution. Results are presented in normal volunteers, patients with LV hypertension (HTN), patients with PHTN, and diabetic patients with myocardial infarction (DMI).

8.2 Materials and Methods

8.2.1 Human Subjects

The BiSUP algorithm was validated on a cohort of 30 human subjects (10 normal volunteers, 7 patients with pulmonary hypertension, 8 patients with hypertension, and 5 diabetics with myocardial infarction). All human studies were approved by the Institutional Review Board of both institutions (Auburn University and University of Alabama at Birmingham) and informed consent was obtained from all participants.

8.2.2 Materials

All participants underwent MRI on a 1.5T MRI scanner (GE Healthcare, Milwaukee, WI) optimized for cardiac application. Standard short-axis cardiac views were obtained, yielding on average 12 short-axis slices. Six equally-spaced, radially-oriented long-axis views (see Figure 8.1b) were obtained, which resulted in 2-3 long-axis slices through the RV free wall, with a fast gradient-echo cine sequence with the following parameters: FOV = 300 mm, image matrix = 224x256, flip angle = 45, TE = 1.82ms, TR = 5.2ms, number of cardiac phases = 20, slice thickness = 8 mm. A 2D fast gradient-recalled spatial modulation of magnetization (FGR-SPAMM) tagging preparation was done with a tag spacing of 7 pixels.

8.2.3 Segmentation

Myocardial contours modeled using active contours were semi-automatically drawn at end-diastole (ED) and end-systole (ES) time frames for all slices (see Figure 8.2). In the short-axis images, two closed contours (LV endo-contour and LV epi-contour) were drawn for the left ventricle, and two open contours (RV endo-contour and RV epi-contour) were drawn for the right ventricle. In the long-axis images, all four were open contours. The RV contours connected to the LV epi-contour at the insertion points. These contours were then propagated to all time frames [115].

8.2.4 Displacement Estimation

3D displacement was measured from the unwrapped HARP phase method described in [90] and in Chapter 6. Phase unwrapping involves adding integer multiples of 2π to the wrapped phase so that the unwrapped phase is continuous. A quality-guided path-following method, also used by Spottiswoode et al. [82] to unwrap wrapped DENSE images, is used to unwrap the wrapped HARP phase images.

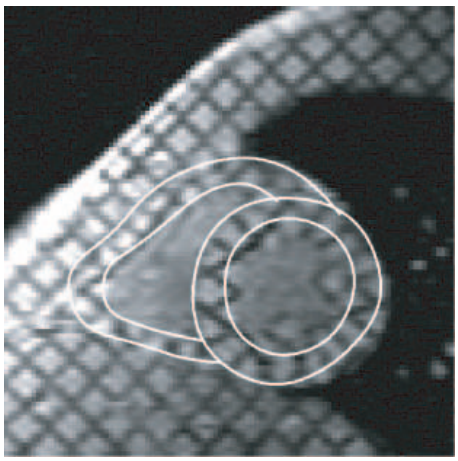

Figure 8.2: A short-axis slice in a normal volunteer at end-systole showing user-input RV and LV contours for the segmentation of the myocardium.

The unwrapped-phase method described uses residues [89] to detect inconsistencies in the wrapped HARP phase. Residues were computed by locally unwrapping a 2×2 neighborhood of each pixel in the region of interest. Phase inconsistencies were corrected using the residue compensation method [89], where residues were removed by connecting residues with branch cuts. Branch cuts are lines in the image where an unwrapping path is not allowed to cross. Branch cuts are specified by the user with a graphical user interface (GUI). Branch-cut placement in the RV is an extension of the method used for the LV in [90]. Since the LV and RV contours are connected at the RV insertion points, the two ventricles are unwrapped as a single entity.

Figure 8.3 shows the effect of branch cuts and the resulting unwrapped phase maps in a short-axis and a long-axis image. Once branch cuts were placed, the phase unwrapping technique described above resulted in a smooth unwrapped phase map as shown in Figure 8.3 (8.3g and 8.3h). Note that after branch cuts are placed, the unwrapped phase is independent of the path taken during the unwrapping process.

Once the phases were unwrapped, 1-D displacements were measured from each pixel in the myocardium similar to those measured from tag-line tracking data [14].

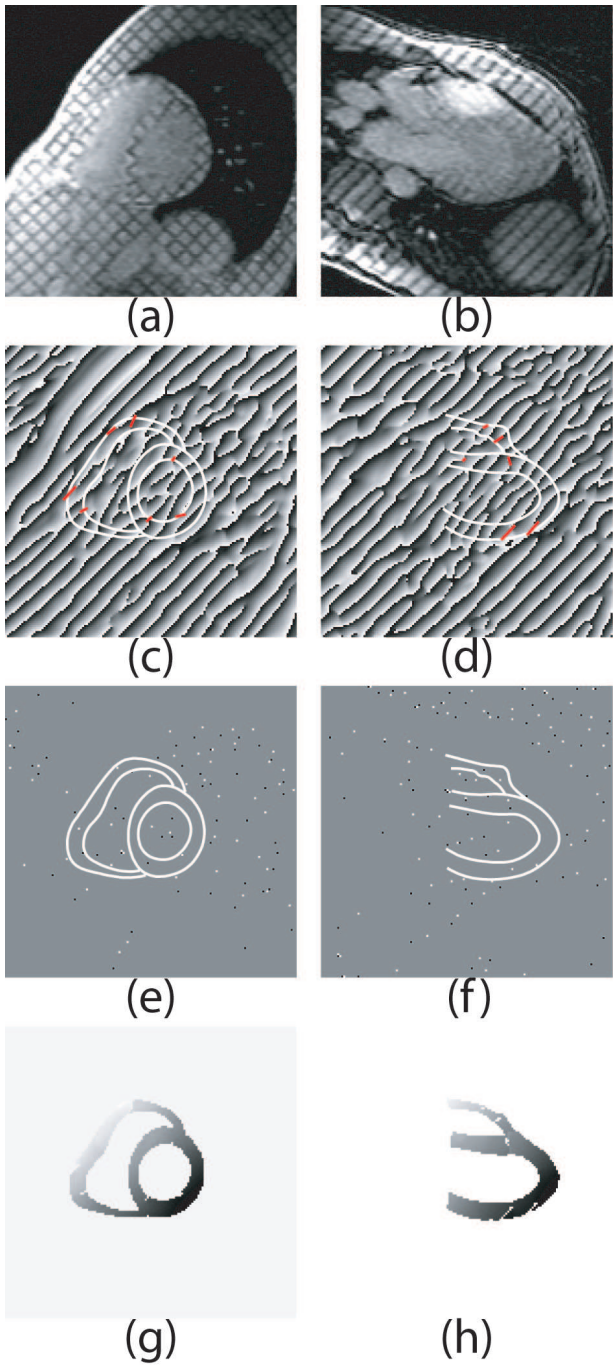

Figure 8.3: Phase Unwrapping example in a short-axis slice (left column) and a long-axis slice (right column) of a patient with pulmonary hypertension: (a-b) Tagged short-axis images acquired near end-systole; (c-d) HARP images obtained from (a) and (b) with branch cuts drawn(red lines). White contours delineate the myocardium. ; (e-f) HARP negative (black) and positive (white) residues in the HARP images in (c-d); (g-h) unwrapped HARP image with branch cuts.

8.2.5 Strain Computation

The DMF technique [114] was used to reconstruct 3D biventricular strains at each imaged time frame from 1D displacement measurements. The DMF technique makes no assumptions about the geometry of the object being analyzed, so both LV and RV strains can be reconstructed as a single object. In addition, because the DMF technique uses finite difference analysis, it does not require a specific coordinate system for the reconstruction [13].

The method proceeds as follows to reconstruct displacement and strain from tag lines and user-defined myocardial contours. For each imaged time frame, the DMF first constructs a 3D segmentation of the LV wall on a regularly spaced discrete grid of points from the user-defined endocardial and epicardial contours. The grid spacing is equal to the pixel size in the MR image. A displacement vector is estimated for each grid point in the LV segmentation that maps the grid point back to its end-diastolic position using finite-difference analysis. A smoothness constraint minimizes the spatial variation of the displacement gradient across the myocardium. The displacement gradient is then computed using a finite-difference derivative approximation averaged over a $3 \times 3 \times 3$ point neighborhood. Finally, the Lagrangian strain tensor is computed from the displacement gradient.

The strains were computed in the circumferential direction (Ecc), longitudinal direction (Ell), and in the direction of maximum principal shortening strain (Emin) in the LV. In the RV, strains were computed in the tangential direction along the short axis of the LV (EttRV), the longitudinal direction (EllRV) and the direction of maximum principal shortening strain (EminRV). In addition, 3D torsion in degrees was computed for the LV.

8.2.6 Validation Experiments

The BiSUP technique was validated on the cohort of 30 human subjects described above. In each subject, 3D strain was computed in all imaged time frames using the BiSUP technique. To validate 3D strain reconstruction, 3D strain was computed at end-systole (ES) with the feature-based (FB) technique in [114], which also uses the DMF strain reconstruction

technique. The tags were tracked using the FB technique and then manually corrected by an expert.

To assess the accuracy of 1D displacement measurements obtained from unwrapped phase images, 1D displacement measurements were computed from tag lines tracked in the FB method and compared to 1D measurements computed from the unwrapped phase images at the tracked tag line points. The accuracy of 3D strains at end-systole was assessed by comparing BiSUP strains and FB strains with paired t-tests, measuring the coefficient of variation and Bland-Altman plots.

To validate the evolution of strains over time, BiSUP strains were compared to 2D strain in each time frame computed using HARP analysis [49]. 2D LV torsion using HARP was measured using the procedure described in [51]. One slice each at the basal and apical levels was used to compute torsion. The basal slice chosen was the slice closest to and below the mitral valve at the end-systolic (ES) phase. The apical slice chosen was the slice closest to the apex where the blood pool could be identified. A mesh consisting of 3 concentric rings and 24 circumferential points was defined in each slice at end-diastole (ED) from semi-automatically-drawn contours. Each mesh was tracked through all time frames using the improved harmonic phase (HARP) method for motion tracking [52]. The accuracy of strains versus time was assessed by comparing peak strains and strain rates computed using BiSUP and HARP with paired t-tests. In all statistical comparisons, a p-value of 0.05 or less was considered statistically significant.

8.3 Results

8.3.1 Computation time

All studies were processed using the BiSUP technique described above, which was implemented in MATLAB (The Mathworks Inc, Natick, MA). Unwrapping all images in a study took less than a minute on a 2.6GHz Core2 Duo processor with 4 GB of memory. Approximately 60 minutes per study of user interaction were required to resolve residues.

Strain reconstruction took approximately 30 minutes per study of automatic computation. The total time required to analyze 20 time frames of a typical study was 90 minutes.

8.3.2 Comparison of Displacement Estimates with FB Technique

Table 8.1 shows statistics of the differences between 1D displacement measurements computed from unwrapped phase images and tracked tag lines at end-systole. The BiSUP and tag line methods showed excellent agreement on long-axis images and short-axis images in the proximal and middle thirds of the LV (relative to the base). The mean differences are a few hundredths of pixel, which means there is no bias toward under or over estimation of displacement. The difference standard deviation is around 1/2 of a pixel, which is close to the tag line tracking accuracy [114, 118]. A small number of differences ($< 1\%$) were in the range of 2-5 pixels. Most of these were near the apex in both the LV and RV where partial volume effects diminished the contrast-to-noise ratio (CNR). However, these measurements were small in number and isolated and had little effect on the resulting strain map due to the smoothness constraints used in the reconstruction.

Table 8.1: Comparison of displacement measurements computed from BiSUP at tracked tag lines at end-systole. Proximal, middle, and distal refer to the LV base. Difference = BiSUP - Tagline

Slices	**Mean Diff.**	**Std. Dev.**	**Diff >2 px**
All slices	0.03	0.51	0.73%
Long-axis	0.03	0.44	0.75%
Short-axis Proximal 3rd	0.00	0.44	0.38%
Short-axis - Middle 3rd	0.06	0.55	0.79%
Short-axis Distal 3rd	0.10	0.69	1.46%

8.3.3 Comparison of End-Systolic Strains with Feature-Based Technique

Figure 8.4 shows the maps of 3D maximal shortening strain (Emin) in a representative normal human volunteer computed using BiSUP method and the FB method. The same DMF reconstruction method was used to reconstruct strain in both methods. Note that

strain is computed in the entire LV and RV, except the apex which is typically not included in this type of analysis. The strains maps are similar. Table 8.2 shows statistics of the difference between the BiSUP and FB methods. In all strains in Table 8.2, the standard deviation of the difference is less than 4% of the average of the two methods. The correlation between the methods is strongest in longitudinal strain. Six long-axis images were acquired, allowing more comparisons so the correlation in longitudinal strain (Ell) and torsion is higher, but the other strains measured showed a high correlation as well. Comparisons between the two sets of strains are displayed in Bland-Altman and correlation plots shown in Figure 8.5 and Figure 8.6. The differences between the computed strains are small with no significant difference found in the LV as shown in Table 8.2. The tangential strain in the RV was found to be significantly different between the BiSUP and FB methods, but this could be because of the increased number of short-axis measurements with BiSUP, which would have a larger effect on the relatively sparsely sampled RV.

Table 8.2: Comparison of 3D, end-systolic strains computed from strain from unwrapped phase (BiSUP) and feature-based (FB) methods. Differences = Mean Standard Error. ρ = Correlation coefficient. CV = coefficient of variation. Ecc = LV Circumferential shortening strain. Ell = LV Longitudinal shortening strain. Emin = LV Maximal shortening strain. EttRV = RV Tangential shortening strain. EllRV = RV Longitudinal shortening strain. EminRV = RV Maximal shortening strain.

Strain	**Differences**			**p**	ρ	**p**	**CV**
Ecc	0.0095	±	0.0019	0.18	0.93	<0.001	2.01%
Ell	-0.0046	±	0.0018	0.63	0.97	<0.001	1.62%
Emin	-0.0048	±	0.0022	0.56	0.93	<0.001	1.59%
Torsion	-1.8019	±	0.2461	0.10	0.97	<0.001	3.01%
EttRV	0.0212	±	0.0026	0.03	0.93	<0.001	3.11%
EllRV	0.0151	±	0.0025	0.15	0.95	<0.001	2.31%
EminRV	0.0154	±	0.0021	0.13	0.96	<0.001	1.51%

8.3.4 Comparison with HARP Strains

Table 8.3 shows statistics of the difference between the 3D strains calculated from BiSUP and the 2D strains from the HARP method [49]. Significant differences were found between

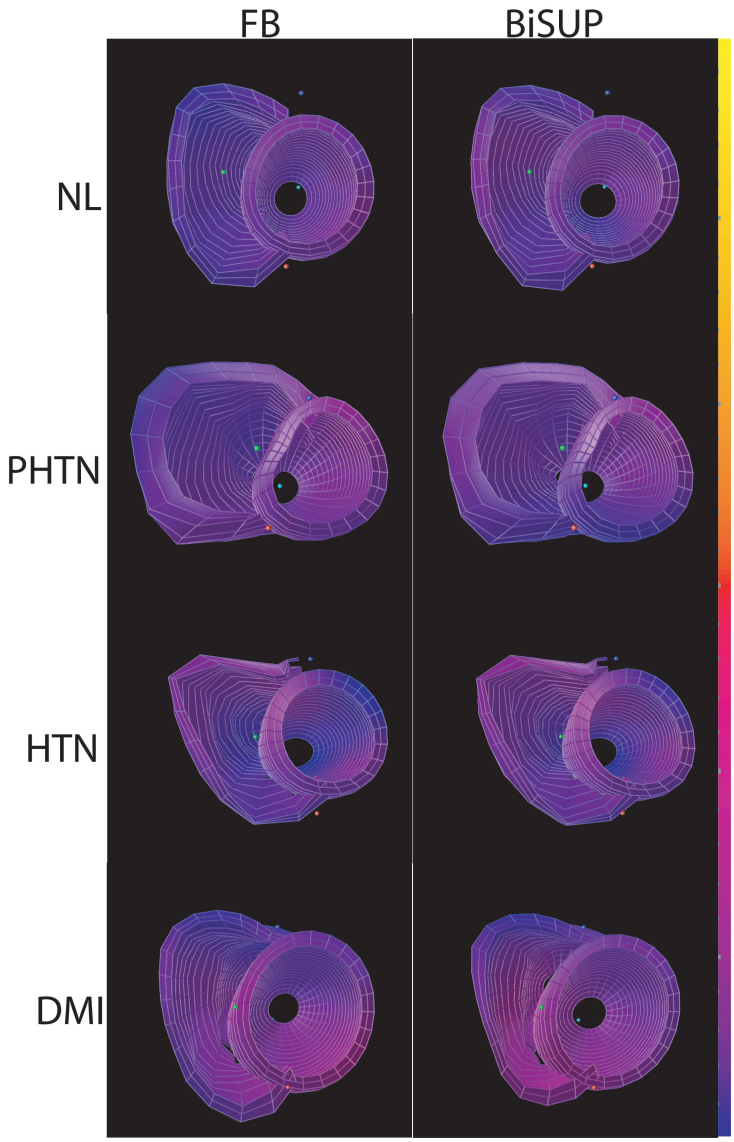

Figure 8.4: Maps of maximum shortening strain (Emin) using feature-based (left) and BiSUP (right) methods for a normal volunteer (NL), and patients with pulmonary hypertension (PHTN), LV hypertension (HTN) and diabetics with myocardial infarction (DMI). Strains are mapped from blue = -25% to yellow = +25%. The anterior LV wall is at the bottom of each strain map.

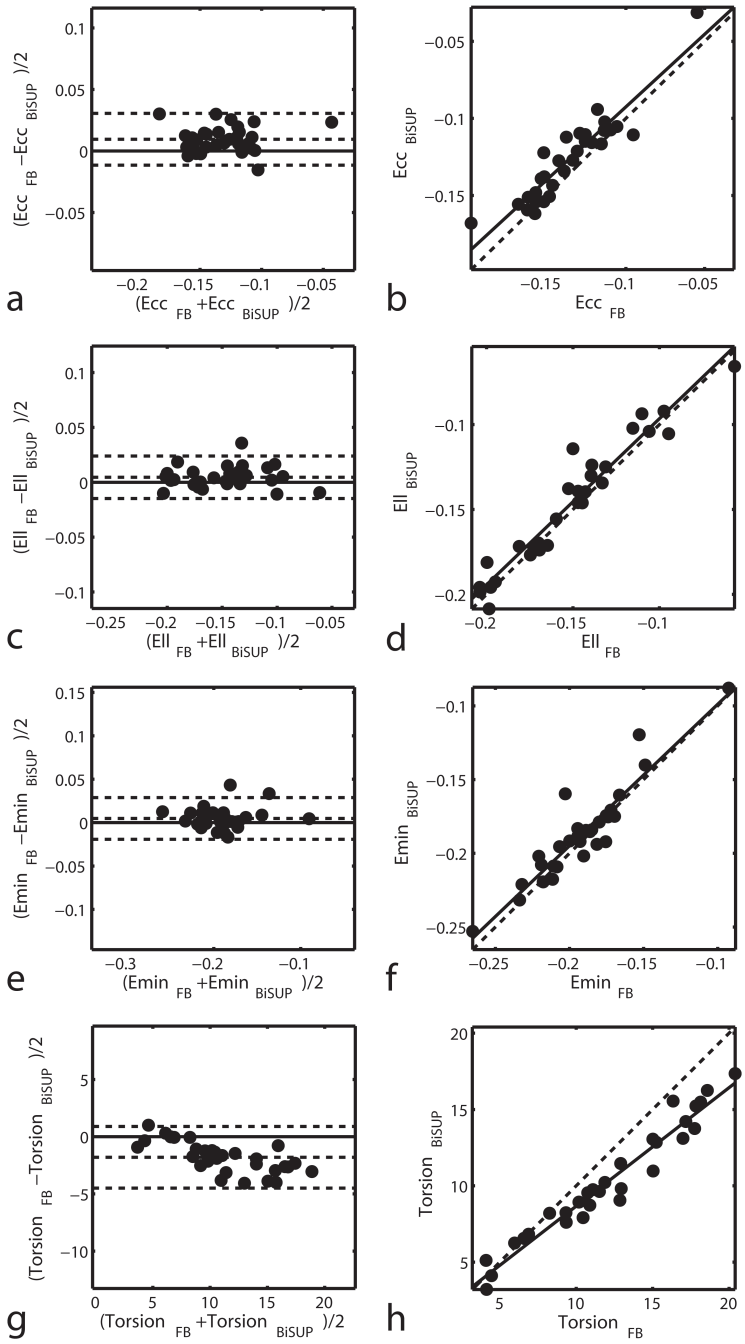

Figure 8.5: Bland-Altman (left) and correlation (right) plots for comparing BiSUP and FB strain measurements in the LV. In the Bland-Altman plots, lines above and below the zero-difference line represent 2 SD of the difference. In the correlation plots, the dashed line represents perfect agreement.

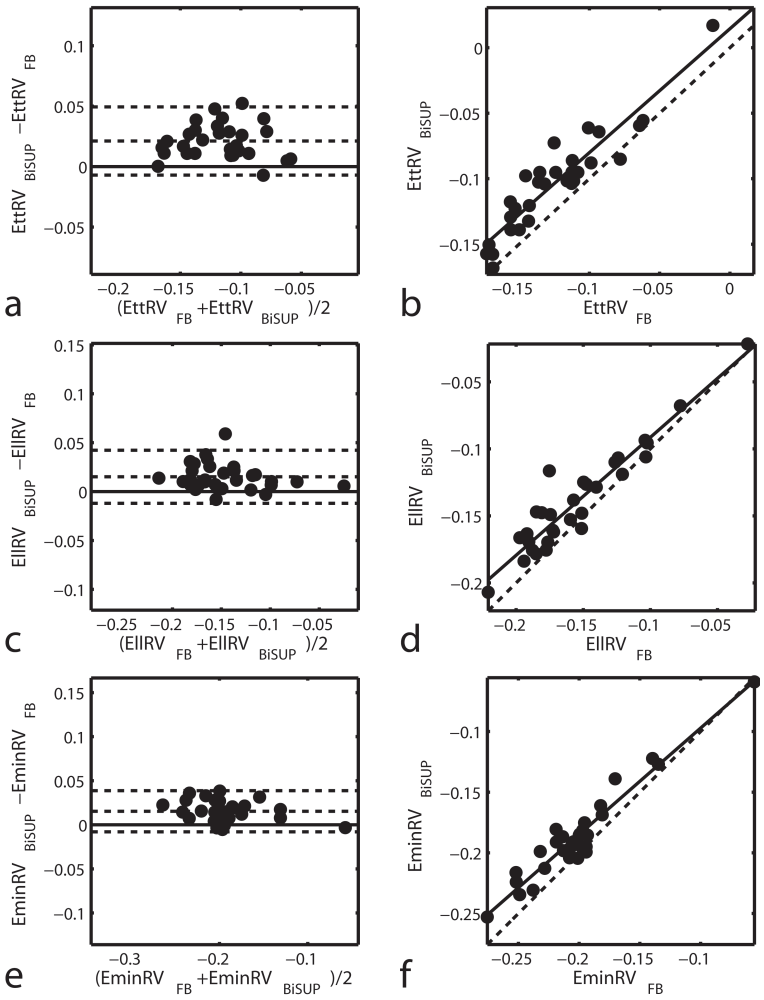

Figure 8.6: Bland-Altman (left) and correlation (right) plots for comparing BiSUP and FB strain measurements in the RV. In the Bland-Altman plots, lines above and below the zero-difference line represent 2 SD of the difference. In the correlation plots, the dashed line represents perfect agreement.

the two techniques in maximum shortening strains (Emin), peak systolic torsion rate and EminRV rate, but the coefficients of variation for these parameters were all less than 10%. Peak strains showed the strongest correlations between the two techniques. Weakest correlations and largest coefficients of variation were found in early diastolic rates due to tag fading in late diastole. Tag fading causes phase inconsistencies, which are corrected in BiSUP with branch cuts. HARP does not provide a mechanism for correcting phase inconsistencies.

Figure 8.7 shows strain and torsion curves for both BiSUP and HARP averaged over the studies for each of the four patient groups showing good agreement between BiSUP and HARP in the temporal evolution of strain.

Table 8.3: Comparison of strains and torsion using the strain from unwrapped phase (BiSUP) and HARP methods. Differences = Mean Standard Error. ρ = Correlation coefficient. CV = coefficient of variation. Ecc = LV Circumferential shortening strain. Emin = LV Maximal shortening strain. EttRV = RV Tangential shortening strain. EminRV = RV Maximal shortening strain.

Strain	**Differences**			**p**	ρ	**p**	**CV**
Ecc							
Peak Strain	-0.0066	±	0.0009	0.39	0.61	<0.001	5.35%
Systolic Rate	-0.0659	±	0.0045	0.10	0.61	<0.001	5.06%
Early-Diastolic Rate	-0.0604	±	0.0127	0.52	0.53	<0.001	13.27%
Emin							
Peak Strain	-0.0224	±	0.0006	0.01	0.83	<0.001	2.64%
Systolic Rate	-0.2604	±	0.0057	0.00	0.66	<0.001	5.99%
Early-Diastolic Rate	0.1328	±	0.0063	0.01	0.58	<0.001	8.81%
Torsion							
Peak Torsion	-1.5122	±	0.1322	0.23	0.70	<0.001	7.35%
Systolic Rate	-16.1142	±	0.7465	0.01	0.58	<0.001	8.49
Early-Diastolic Rate	13.0258	±	0.8720	0.07	0.55	0.0018	9.48%
EttRV							
Peak Strain	0.0011	±	0.0010	0.90	0.61	<0.001	6.86%
Systolic Rate	0.0934	±	0.0105	0.16	0.24	0.2031	10.81%
Early-Diastolic Rate	-0.3137	±	0.0248	0.07	0.39	0.0315	20.08%
EminRV							
Peak Strain	-0.0119	±	0.0008	0.21	0.80	<0.001	3.13%
Systolic Rate	-0.1659	±	0.0076	0.01	0.60	<0.001	7.47%
Early-Diastolic Rate	0.0150	±	0.0094	0.83	0.48	0.0069	11.44%

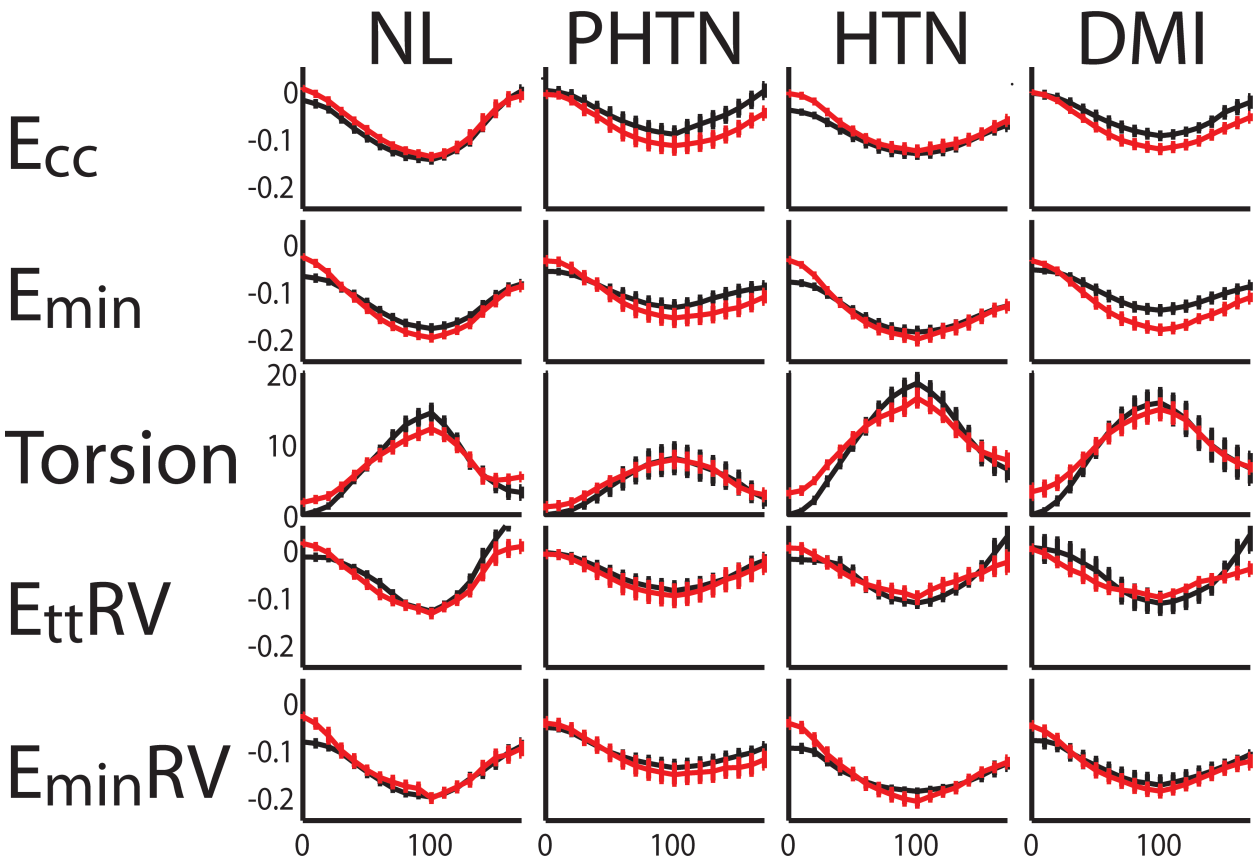

Figure 8.7: Plots of average mid-ventricular strain and torsion obtained from 2D HARP (black) and 3D BiSUP (red) methods for normal volunteers (NL) and, patients with pulmonary hypertension (PHTN), LV hypertension (HTN) and diabetics with myocardial infarction (DMI). X-axis represents in percentage systolic interval. Error bars represent one standard error.

Figure 8.8 shows maximal shortening strain for a normal volunteer and patients with pulmonary hypertension, left ventricular hypertension and a diabetic with myocardial infarction at different phases of the cardiac cycle. It is clear that the shortening in the RV is depressed in patients with pulmonary hypertension relative to the normal volunteers (also see Figure 8.7). Also, note the excursion of the RV into the LV at the septum.

8.4 Discussion

The application of tagged MRI to the RV has various difficulties; the thin wall of the normal RV limits the number of tag lines, which may hinder accurate quantification [122]. Several myocardial tagging studies have been performed on the RV to investigate and characterize mechanical deformation. Klein et al. [123] used measures of percent segmental shortening of the RV free wall. Zahi et al. [122] designed a specific breath hold imaging sequence with 1-D tag lines for RV tagging acquisition and thus were able to characterize the RV regional deformation. Young et al. [124] used a finite-element model for 3D reconstruction of the in-plane deformations of the RV free wall as a surface. Haber et al. [29] also used a finite-element model to obtain 3D strains in the RV. Using this model, they were able to quantify components of the in-plane strain tensor in the RV free wall. Tustison et al. [74] computed biventricular strains using volumetric deformable models with a non-uniform rational B-splines (NURBS) basis. All the 3D methods [29, 74, 124] feature tag tracking to obtain displacements.

In this chapter, an unwrapped phase technique to compute 3D biventricular strain in about three-fourths of the cardiac cycle using tagged cardiac MR images has been described and validated. The BiSUP technique consists of an unwrapped phase technique to compute the 1D displacements followed by a discrete model-free reconstruction method to obtain 3D strain measurements.

We demonstrated on human subjects of different pathologies that the circumferential, longitudinal and maximal shortening strains measured using BiSUP are similar to those

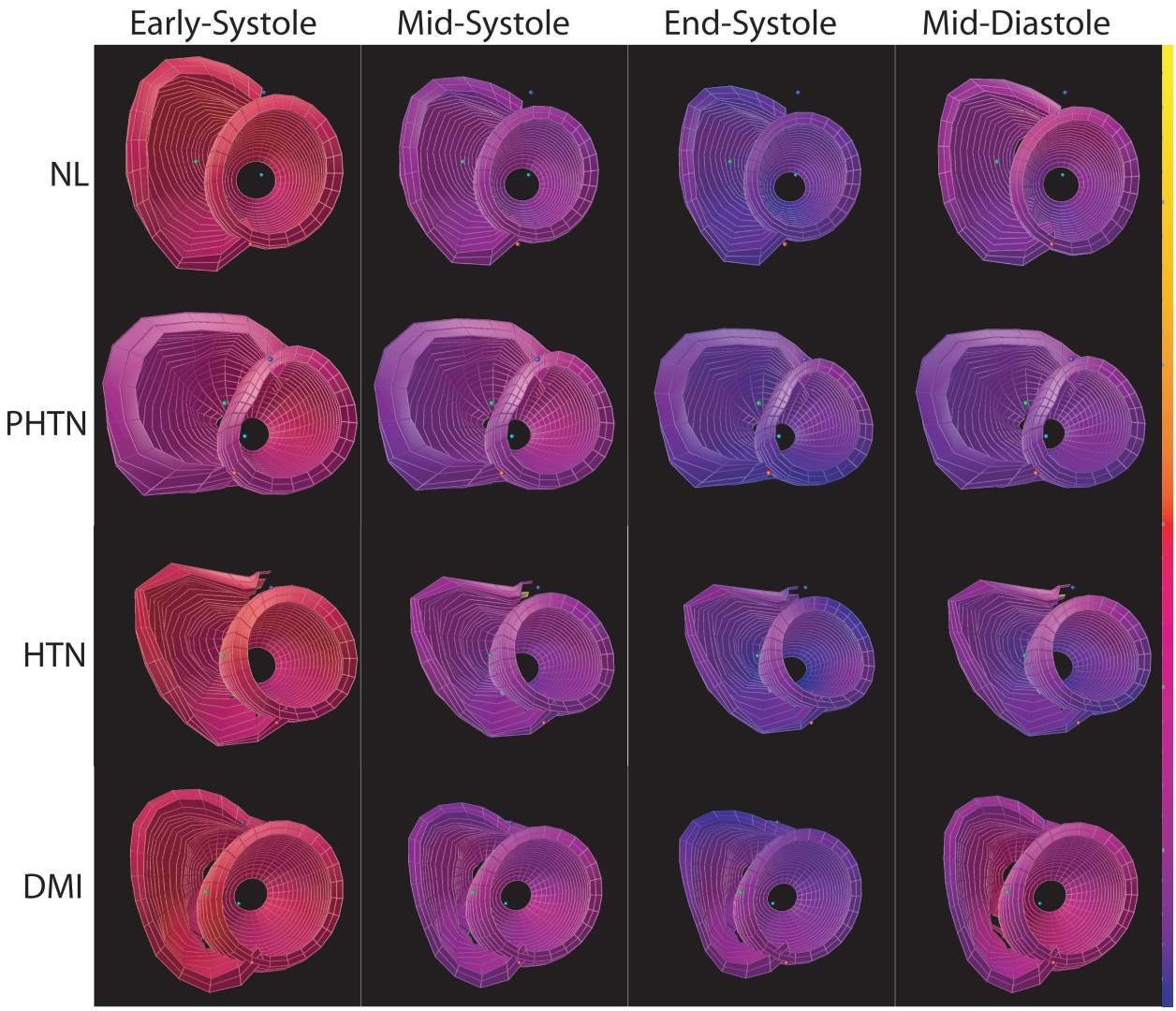

Figure 8.8: Maps of maximum shortening strain (Emin) using the BiSUP method for a normal volunteer (NL), and patients with pulmonary hypertension (PHTN), LV hypertension (HTN) and diabetics with myocardial infarction (DMI) from early-diastole through mid-diastole of a cardiac cycle. Strains are mapped from blue = -25% to yellow = +25%. The anterior LV wall is at the bottom of each strain map.

obtained from a feature-based method that uses tag tracking to obtain the displacement measurements. The time required for the BiSUP measured strains in the entire LV and RV combined over 20 time frames is less than 1.5 hours per study with less than an hour of manual intervention. The same analysis using the feature-based method would require approximately 4 hours with significantly higher manual intervention. Compared to methods based on tracking tag lines [29,122,124], displacement measurements from the BiSUP method are dense, potentially resulting in more accurate estimates of strain.

The strains from the BiSUP method were also compared to the strains from HARP. BiSUP-HARP agreement was not as strong as BiSUP-FB agreement because the BiSUP computes 3D strain, while HARP computes 2D strain. Also, the tag line CNR decreases through the cycle due to T_1 decay of the tag pattern, so early diastolic correlations are lower than correlations for peak strain and systolic strain rate. It was seen that HARP in general underestimated the maximal shortening strains as compared to the BiSUP method. This could be attributed to the improved accuracy of tracking using the BiSUP method as a result of removal of inconsistencies in the HARP image using branch cuts. Also, HARP analysis does not correct for motion through the stationary basal and apical image planes, whereas BiSUP reconstructs 3D deformation and strain in each time frame, which corrects for through-plane motion. With HARP, torsion is computed with HARP tracking, and large deformations between time frames can cause errors. The unwrapped phase technique used in BiSUP is more robust than HARP to large interframe deformations [90]. With unwrapped phase, points can be tracked through an image sequence as long as the average inter-frame deformation over the entire myocardium is less than one-half tag spacing.

The DMF method has advantages that are utilized for the reconstruction of strain in the RV and in the LV in patients with pulmonary hypertension. The DMF method does not need a specific coordinate system to do the LV reconstruction and uses less smoothing than other reconstruction methods [13]. Therefore, the lack of a consistent geometry does

not affect the performance of the DMF method as opposed to finite-element methods and prolate-spheroidal methods.

In conclusion, the BiSUP method can compute accurate 3D biventricular strains through the cardiac cycle in a reasonable amount of time and user interaction compared to other 3D analysis methods.

Chapter 9

Computer-Assisted Strain from Unwrapped Phase

9.1 Introduction

The unwrapped-phase (mSUP) [90] method previously described in Chapter 6 uses residues [89] to detect inconsistencies in the wrapped HARP phase. Residues were computed by locally unwrapping a 2×2 neighborhood of each pixel in the region of interest. Phase inconsistencies were corrected by a technique called branch cuts, which removed certain pixels from the region of interest. Branch cuts are specified by the user with a graphical user interface (GUI). With unwrapped phase, points can be tracked through an image sequence as long as the deformation between time frames is less than half a tag spacing. Compared to other feature-based methods, displacement measurements from unwrapped HARP phase images are denser than those obtained from tracking tag lines or tag intersections, potentially resulting in more accurate estimates of strain. It can compute strains in the entire LV and is also more robust to interframe motion compared to methods based on tracking the wrapped phase. This method still requires user interaction to place the branch cuts.

In this chapter, a computer-assisted branch-cut placement in short-axis HARP images is presented to compute the strain from unwrapped phase (caSUP). This method is based on branch-cut placement using simulated annealing, which has been proposed for general-purpose phase unwrapping [125]. The method in [125], however, minimizes the branch cut length, which is a reasonable criterion in single-image unwrapping. In cardiac imaging, we wish to unwrap a sequence of images. We propose a new energy function for simulated annealing-based phase unwrapping that is based on temporal continuity of the unwrapped phase. An energy term is proposed that enables the application of the phase unwrapping

method to a sequence of images. The caSUP method described here requires user interaction other than segmentation of the myocardium, to correct for any detected errors in the unwrapping. It saves about one-third of the time involved in manual branch-cut placement. To compute 3D LV strain, the caSUP method is used to unwrap short-axis images and the manual branch-cut method [90] is used to unwrap long-axis images.

This chapter is organized as follows. The caSUP method and strain reconstruction is presented in Section 2. Experimental validation results on 40 human studies and conclusions are presented in Sections 3 and 4.

9.2 Materials and Methods

9.2.1 Human Subjects

A cohort of 40 studies consisting of 10 normal volunteers, 10 diabetics with myocardial infarction, 10 patients with mitral regurgitation, and 10 patients with hypertension was used to validate the caSUP method. All human studies were approved by the Institutional Review Board of both institutions (Auburn University and University of Alabama at Birmingham) and informed consent was obtained from all participants.

9.2.2 Data Acquisition

All participants underwent MRI on a 1.5T MRI scanner (GE, Milwaukee, WI) optimized for cardiac application. Tagged images were acquired in standard views (2-chamber and 4-chamber long-axis and short-axis) with a fast gradient-echo cine sequence with the following parameters: FOV = 300 mm, image matrix = 224x256, flip angle = 45, TE = 1.82ms, TR = 5.2ms, number of cardiac phases = 20, slice thickness = 8 mm. A 2D fast gradient-recalled spatial modulation of magnetization (FGR-SPAMM) tagging preparation was done with a tag spacing of 7 pixels. This protocol resulted in 2 long-axis slices and on average 12 short-axis slices per study.

9.2.3 Phase Unwrapping

In the unwrapped-phase (mSUP) method previously described in [90], branch cuts are specified by the user with a graphical user interface (GUI). In this chapter we explore the possibility of an automated branch-cut placement method. Ideally, given a set of positive and negative residues, the surest way of finding the correct branch-cut configuration is to explore every possible combination (exhaustive search). The configuration that minimizes a defined energy function is chosen as the best fit.

A new energy function is proposed for phase unwrapping that minimizes the difference in unwrapped phase between successive time frames. The energy function E_t is defined as,

$$E_t = \sum \|\phi_t - \phi_{t-1}\|, \tag{9.1}$$

where ϕ_t is the unwrapped phase at time frame t. In the phase unwrapping literature, algorithms seek to minimize the aggregate branch-cut length, which is a reasonable criterion in single-image unwrapping. In cardiac imaging, we wish to unwrap a sequence of images. The proposed energy function allows us to maintain temporal continuity of the unwrapped phase, enabling its application to unwrap a sequence of images. The unwrapped phase ϕ is obtained by unwrapping the HARP phase (wrapped) using flood-fill quality-guided phase unwrapping [89, 90] after the application of the present branch-cut configuration.

The exhaustive search method is adequate when the number of residues is low, but as the number of resiudes increases, exploration of all combinations is impractical as the number of possible configurations becomes prohibitively large (see Figure 9.1). In such cases, it is more economical to use a method such as the simulated-annealing-based branch-cut (SABrCut) placement method described below.

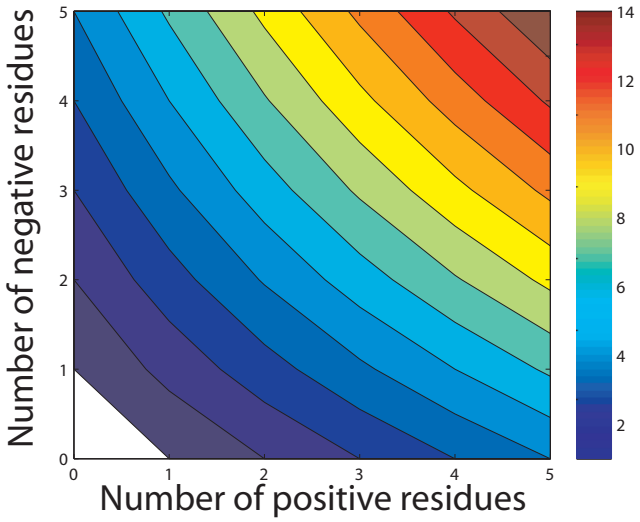

Figure 9.1: A logarithmic (log_2) plot showing the number of possible branch cut configurations given the number of residues in the image.

9.2.4 Simulated Annealing

This method is based on branch-cut placement using simulated annealing, which has been proposed for general-purpose phase unwrapping [125]. The method in [125], however, minimizes the branch-cut length, while we minimize energy defined in Equation (9.1).

Simulated annealing based branch cut placement [125] consists of:

1. An initial random configuration of branch cuts, which can be addressed as a proposed solution to the branch-cut placement problem. In this research, the initial branch-cut configuration is chosen by nearest-neighbor method, but any automatic algorithm can be used. In the nearest-neighbor method, each residue is connected to the closest residue of opposite polarity or the border, whichever is the nearest.

2. An energy function E that describes the quality of a proposed solution. In this research, we minimize energy defined in Equation (9.1).

3. A generation mechanism that applies small changes to produce a new branch-cut configuration. For each iteration k, a small change to the branch-cut configuration is applied.

A negative and a positive residue are randomly selected. Existing branch cuts involving these residues are deleted, and new branch cuts are applied according to the scheme described in Figure 9.2. This scheme is similar to the one used in [125] with the exception of the endocardial/epicardial configuration, which is unique to our algorithm. If there is more than one possible new branch-cut configuration, one is chosen at random. The energy E_t^{k+1} of the new configuration is then calculated. The energy difference is

$$\Delta E_t^k = E_t^{k+1} - E_t^k \tag{9.2}$$

4. An acceptance criterion to decide whether the new proposed solution is accepted. The new configuration is always accepted if $\Delta E < 0$. Accepting a new configuration only if $\Delta E < 0$, though, may mean that the algorithm is trapped in a local minimum. Therefore, increasing values of E are also accepted at a Boltzmann probability. The acceptance probability p, therefore is

$$p = \begin{cases} 1 & , \quad \text{if } \Delta E \leq 0 \\ e^{-\Delta E/T} & , \quad \text{if } \Delta E > 0 \end{cases} \tag{9.3}$$

5. A control parameter T to control the acceptance probability of proposed solutions and a cooling schedule for T. The Boltzmann probability is controlled by the temperature T. For high values of T, even high increases in energy could be accepted, while for low values of T the acceptance probability of these moves is close to zero. When a number of transitions are applied to the system at a constant temperature, the system reaches a thermal equilibrium. The series of configurations resulting from these transitions is called a homogeneous Markov chain. The SABrCut algorithm consists of several Markov chains that start at high values of T. Reducing the temperature T slowly reduces the internal energy of the system until it reaches a minimum, which is identified as the solution of our

optimization problem. The values of T are determined by a cooling schedule

$$T^{k+1} = \frac{T^k}{1 + [T^k \ln(1+\delta)/(3\sigma^k)]}, \tag{9.4}$$

with Equation (9.4) controlling the cooling speed and σ the standard deviation of the energy during the final Markov chain. The cooling speeds are kept low to allow the algorithm to reach the global minimum. The values $T_{initial} = 10000$ and $\delta = 0.25$ were chosen empirically.

6. A stopping criterion to decide whether the algorithm has found a final solution. When there is no change in the accepted energy for a number of consecutive configuration changes, the algorithm is terminated and the final configuration is accepted as the solution.

9.2.5 caSUP

Figure 9.3 shows the time taken using the exhaustive search and simulated annealing methods to find a suitable solution for a given number of residues in the image. In this research, we utilized the fact that the exhaustive search to determine the best branch-cut configuration was faster than the SABrCut when the number of residues is small, but the SABrCut method is faster for a greater number of residues. Therefore, the exhaustive search method was used when the number of residues is less than 6, and the SABrCut method was used otherwise.

As explained in [90], branch cuts are required because of prematurely ending tag lines, tag-line merging or spurious phase wraps. The branch cuts can be seen as either the continuation or deletion of a tag line. Therefore, branch cuts are drawn parallel to the tag lines (i.e. along the tag line direction) when connecting to the myocardial borders.

A discontinuity map, similar to the one used in [82], was used to detect images with incorrect unwrapping. A discontinuity map measures the gradient of the unwrapped phase, and if the unwrapping is correct, the gradient magnitude of the unwrapped phase does not

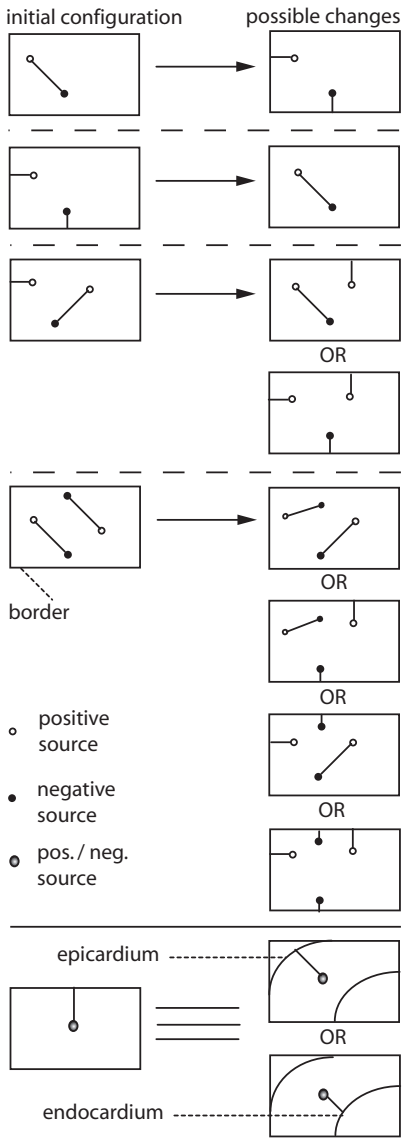

Figure 9.2: Generation mechanism to apply small changes to the existing set of branch cuts. Two sources of opposite sign are selected randomly. Depending on the initial situation, branch cuts are deleted and new branch cuts are set. A border connection is a connection to either the epicardial or the endocardial boundary, each of which is chosen with equal probability.

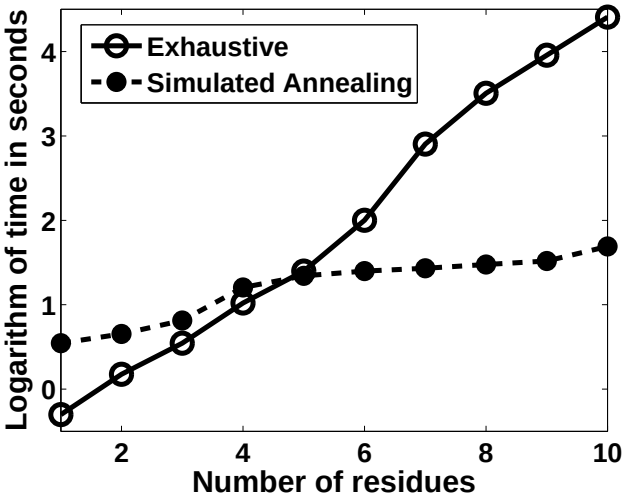

Figure 9.3: The logarithm (log_{10}) of the time taken in seconds using the exhaustive search and simulated annealing methods to find a suitable solution depending on the number of residues.

exceed π. When discontinuity is detected in the unwrapping of a slice, user interaction (as in [90]) is used to manually place the branch cuts for the slice. The entire procedure involved is called computer-assisted strain from unwrapped phase (caSUP).

9.2.6 Motion and Strain Estimation

Each image is unwrapped independently, and the starting point for phase unwrapping may be different in each image. As a result, the unwrapped phases in two adjacent time frames may differ by an integer multiple of 2π. This difference can be corrected by adding an integer multiple of 2π to all unwrapped phases in the current time frame. The multiple is chosen to minimize the L_1 norm of all displacements between the current and previous frames. Note that this correction assumes that the L_1 norm of the actual unwrapped phase difference between consecutive frames is less than π, which corresponds to one-half of the tag spacing. Also, interframe deformation of more than one-half tag spacing in a localized region or regions will not affect the unwrapped phase as long as the average deformation is less than one-half tag spacing.

The caSUP method described above was used to unwrap all short-axis slices. Long-axis slices were unwrapped using the manually placed branch-cut method described in [90]. Once the phases were unwrapped, 1-D displacements were measured from each pixel in the myocardium using the technique described in [90]. Each 1-D displacement measurement is the displacement of the point back to its undeformed position along a line perpendicular to the tag plane (see [90] for details). Both the phase alignment and displacement measurement steps required that the LV wall be segmented in each slice and time of interest. This segmentation was done using the automated dual-contour propagation method described in [126]. The 1-D displacement measurements and a material-point mesh automatically constructed from the end-diastolic (ED) contours were used to compute 3-D LV deformation and strain in each time frame. The deformation and strain are reconstructed using the Affine Prolate Spheroidal B-Spline (APSB) method described in [90].

9.3 Experiments

9.3.1 Computation Time

All studies were processed using the caSUP technique described above, which was implemented in MATLAB (The Mathworks Inc, Natick, MA). Unwrapping all images in a study took less than a minute on a 2.6GHz Core2 Duo processor with 4 GB of memory. Approximately 30 minutes per study of automated processing followed by 15 minutes of user interaction were required to resolve residues. Strain reconstruction took approximately 5 minutes per study. The total time required to analyze 20 time frames of a typical study was 50 minutes. This saves 15-20 minutes of user interaction for the user.

9.3.2 Validation

The caSUP technique was validated on the cohort of 40 human subjects. In each subject, 3D strain was computed in all imaged time frames using the caSUP and mSUP techniques. Both the caSUP and mSUP methods use the APSB deformation model described in [116].

The mSUP method was earlier validated with and compared to HARP strains [50] and 3D strain from a feature-based method [45, 116]. The accuracy of 3D strains was assessed by comparing caSUP strains and mSUP strains at end-systole with a paired t-test. In all statistical comparisons, a P value of 0.05 or less was considered statistically significant.

A total of 349 short-axis slices were processed. In 338 of these slices, the caSUP algorithm placed branch cuts correctly, and no user interaction was required. In eleven slices, errors were detected automatically using the discontinuity map and manually corrected. The errors occur predominantly at the apical slices, caused by partial volume effects and low contrast-to-noise ratio (CNR).

Table 9.1 shows statistics of the difference in averaged mid-ventricular strains between the unwrapped phase methods caSUP and mSUP. In all strains in Table 9.1, the caSUP strains are highly correlated with mSUP strains, and the difference standard deviation is less than 3% of the average of the two methods. The mean difference between caSUP and mSUP methods is low across all measured quantities, showing no bias toward under- or overestimation of strain. The longitudinal strain and torsion show a slightly lower correlation compared to the circumferential and maximal shortening strains, because there are 8-12 short-axis slices per study but only two long-axis images. Also, the torsion measurements show a lower correlation without corrections as most of the errors occur at the apex.

Figure 9.5 shows maps of 3D circumferential strain (Ecc) computed from the caSUP and the mSUP methods for a representative from all the patient groups. Note that the same material-point mesh and deformation model was used to reconstruct strain in all methods. The strain maps are mostly similar. Differences, if any, are noted at the apex where the increased through-plane motion and rotation affects the ability of the computer-assisted branch cut placement method to obtain the correct branch-cut configuration.

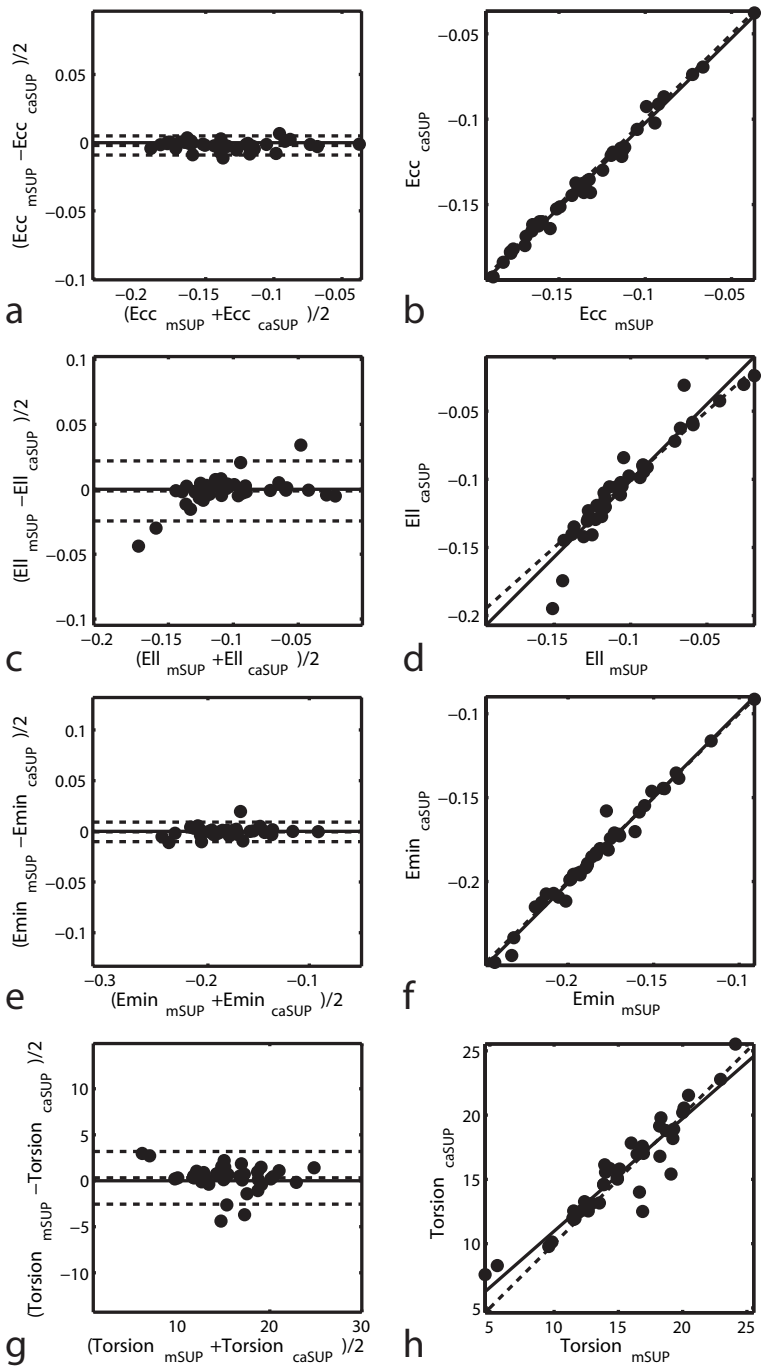

Figure 9.4: Bland-Altman (left) and correlation (right) plots for comparing caSUP and mSUP strain measurements. In the Bland-Altman plots, lines above and below the zero-difference line represent 2 SD of the difference. In the correlation plots, the dashed line represents perfect correlation.

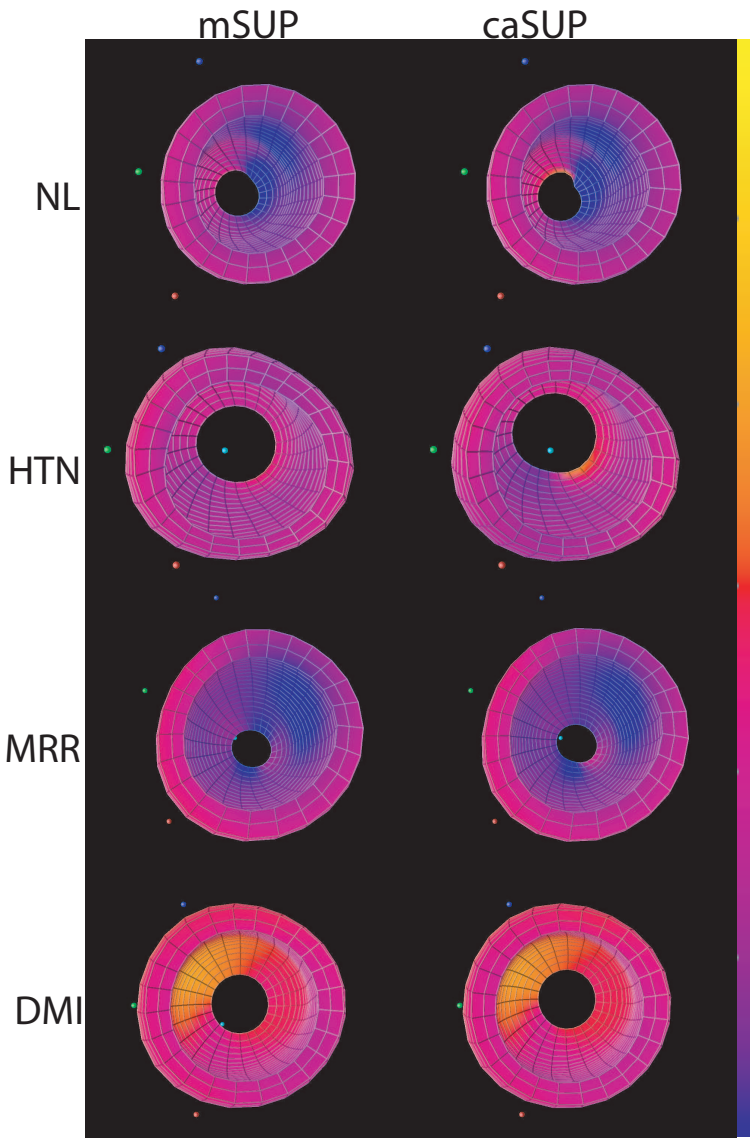

Figure 9.5: Maps of circumferential (Ecc) strain using computer-assisted strain from unwrapped phase (left) and manual strain from unwrapped phase for normal (NL), hypertensive (HTN), mitral regurgitant (MRR) and myocardial infarct (DMI) hearts at end-systole. Strains are mapped from blue = -25% to yellow = 25%. The mid-septum is marked by the green landmark.

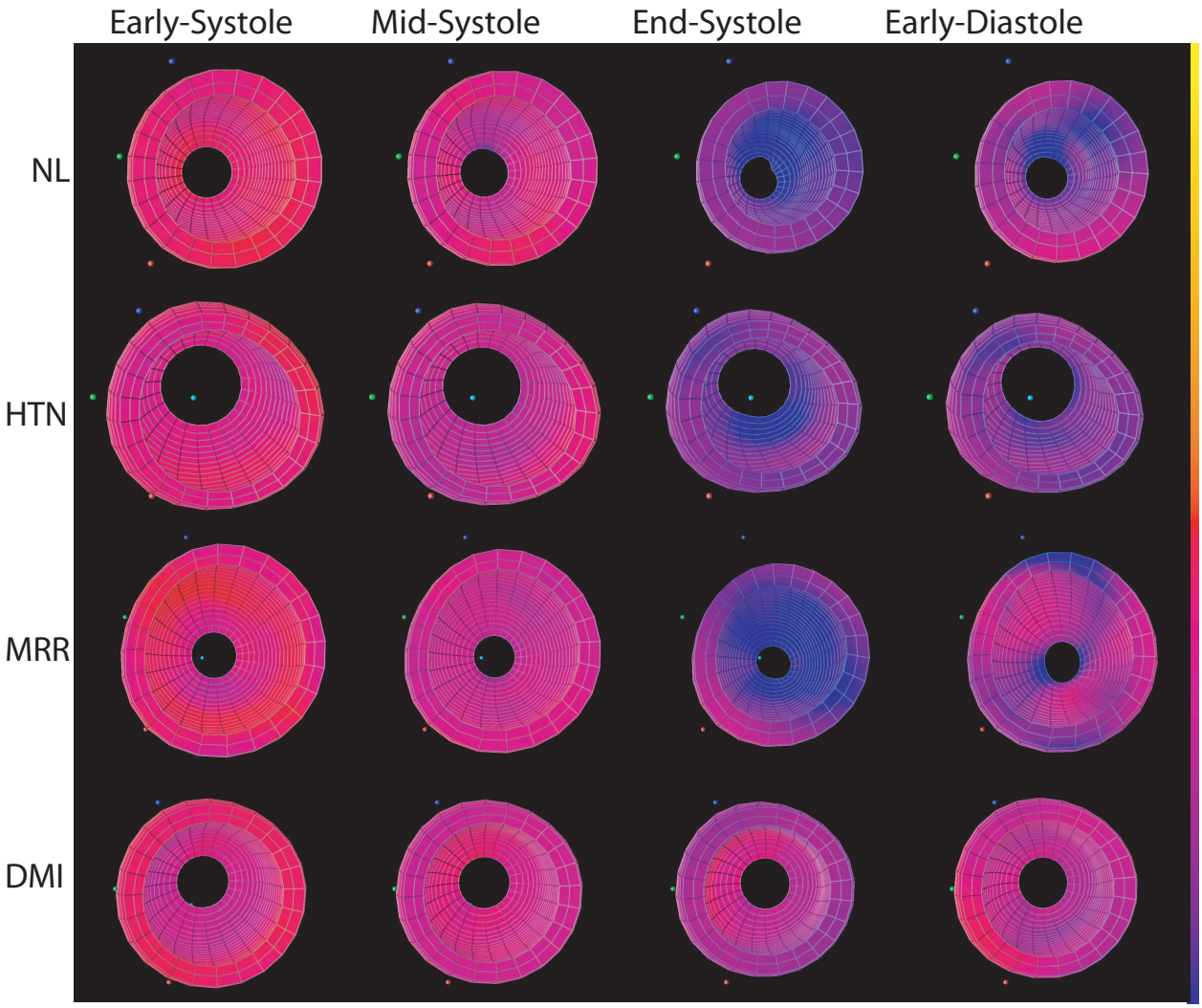

Figure 9.6: Maps of maximal shortening (Emin) strain using computer-assisted strain from unwrapped phase for normal (NL), hypertensive (HTN), mitral regurgitant (MRR) and myocardial infarct (DMI) hearts through the cycle. Strains are mapped from blue = -25% to yellow = 25%. The mid-septum is marked by the green landmark.

Table 9.1: Comparison of strains and torsion computed using caSUP and mSUP methods. Differences are caSUP-mSUP. Differences = Mean ± Standard Error. ρ= Correlation coefficient. For all correlation coefficients, $p < 0.001$. CV = coefficient of variation.

Strain	Differences			p	ρ	CV
After corrections						
E_{cc}	-0.002	±	0.001	0.79	0.99	0.65%
E_{ll}	0.001	±	0.002	0.87	0.96	2.78%
E_{min}	0.001	±	0.001	0.94	0.99	0.66%
Torsion	0.321	±	0.227	0.72	0.94	2.33%
Without corrections						
E_{cc}	-0.003	±	0.001	0.71	0.99	0.77%
E_{ll}	-0.001	±	0.001	0.97	0.97	1.72%
E_{min}	-0.003	±	0.002	0.72	0.95	1.38%
Torsion	0.354	±	0.296	0.71	0.91	3.03%

9.3.3 caSUP in Normals and Patients

Figure 9.6 shows maps of 3D maximal shortening strain (Emin) computed from the caSUP method for a representative from all the patient groups. The figure demonstrates the ability of the caSUP method to produce strains in various pathologies and with different cardiac morphologies.

9.4 Discussion

A computer-assisted strain from unwrapped phase (caSUP) procedure was presented for measuring 3D deformation from tagged MRI. This method used automated branch cut placement to resolve residues, before unwrapping HARP images. Manual intervention is used to modify the branch-cut configuration when errors are discovered in the proposed branch cuts. Displacement and 3D strain can then be calculated from the unwrapped phase images. 40 studies from different groups were used to validate the algorithm. caSUP strains demonstrated excellent agreement with the previously presented manual strain from unwrapped phase (mSUP).

The time required for the caSUP-measured 3D strains in the entire LV over 20 time frames is approximately 45 minutes per study with about 10 minutes of user interaction

required. The same analysis would require around 30-40 minutes of user interaction using the manual strain from unwrapped phase (mSUP). The feature-based method [45,116] would require approximately 3 hours of user interaction. Most of the user interaction required is usually later in the cycle (mid to late diastole) when the tag CNR reduces rapidly. Advanced tagged imaging techniques such as Complementary SPAMM, can yield a higher tag CNR throughout the cardiac cycle. Higher CNR images will result in fewer phase inconsistencies, and therefore, automated resolving of branch cuts is faster and lesser user interaction will be required to correct them. Consequently, if strains are to be computed only through systole as is so often the case, required user interaction would drastically reduce.

The HARP method [50] is sensitive to large (greater than one-half tag spacing) interframe displacements. Therefore, we used a method based on the phase of the entire myocardium over time to maintain phase consistency. This allows for local tissue to have displacements greater than one-half tag-spacing between time frames as long as the average deformation of tissue between time frames is less than one-half tag-spacing. Moreover, it allows the users to check for errors and correct them, unlike HARP.

In conclusion, the computer assisted strain from unwrapped phase (caSUP) method can compute parameters such as 3-D strain, strain rate and torsion in the LV through the cardiac cycle in a reasonable amount of time and with minimal user interaction compared to other 3D analysis methods.

Chapter 10

Torsion Hysteresis

10.1 Introduction

Left ventricular (LV) diastolic dysfunction is characterized by abnormal myocardial mechanical properties that include impaired diastolic distensibility, impaired LV filling and slow or delayed myocardial relaxation [127]. Up to 50% of patients with heart failure have predominant diastolic dysfunction in the presence of preserved LV ejection fraction (EF) [128]. Measurement of LV pressure-volume relations is perhaps the reference standard for diagnosing diastolic dysfunction. This is based on the premise that the LV diastolic pressure rises excessively during ventricular filling due to impaired LV distensibility and/or compliance. Quantifying the exponential fall of pressure during isovolumic relaxation phase by the time constant of relaxation, τ, is considered a reliable, relatively load independent measure of diastolic relaxation of the LV.

LV torsion/twist is an important mechanical property of the myocardium that promotes more efficient cardiac function. It represents the myocardial rotation gradient from the base to apex along a longitudinal axis [120]. Torsion is due to the criss-crossing helical orientation of the myofibrils from the subendocardium to the subepicardium. Contraction of myocardial bundles and their interaction with extracellular matrix during systole results in storage of torsional potential energy. Torsional recoil during isovolumic relaxation and early diastole releases the potential energy stored in the deformed matrix during systole [129,130]. Previous work with cardiac magnetic resonance imaging (MRI) in an animal model [131] and recently in humans [132] has shown that LV early untwist rate correlates closely with the time constant of LV relaxation.

The term 'hysteresis' is used in mechanical engineering, to describe history-dependent stress-strain relationships in materials undergoing cyclic loading. In these applications, the area between stress-strain loops is related to energy loss due to friction [133]. Research groups have used hysteresis in stress-strain loops to study viscoelastic losses in isolated myocytes [134, 135], chick embryo heart [136–138] and other animal models [139].

In the current investigation, we apply the hysteresis concept to torsion-volume loops obtained in normal subjects and in patients with hypertension (HTN) and mitral regurgitation (MR) patients with preserved LVEF and no evidence of coronary artery disease. We hypothesized that the area enveloped by these curves (torsional hysteresis) represents loss of energy from work against viscoelastic properties of myocardium and hence will represent global diastolic function.

10.2 Magnetic Resonance Imaging

Magnetic resonance imaging was performed on a 1.5T MRI scanner (Signa GE, Milwaukee, Wisconsin) optimized for cardiac application. Electrocardiographically gated breath-hold steady-state free precision was used to obtain standard (2-, 3-, and 4-chamber short-axis) views using the following parameters: slice thickness of the imaging planes 8 mm, field of view 44×44, scan matrix 256×128, flip angle 45, repetition/echo times 3.8/1.6 ms. The temporal resolution of the cine MRI was < 50 ms. Tagged magnetic resonance images were acquired on the same scanner with repetition/echo times 8/44 ms, and tag spacing 7 mm. Typical temporal resolution of the tagged MRI scan was 80 ms. Imaged population included 37 normal volunteers (NL), 78 patients with hypertension (HTN) and patients with mitral valve disease (MR).

10.3 Geometric analysis

LV geometric parameters were measured from endocardial and epicardial contours manually traced on cine images acquired near end-diastole and end-systole. These contours were

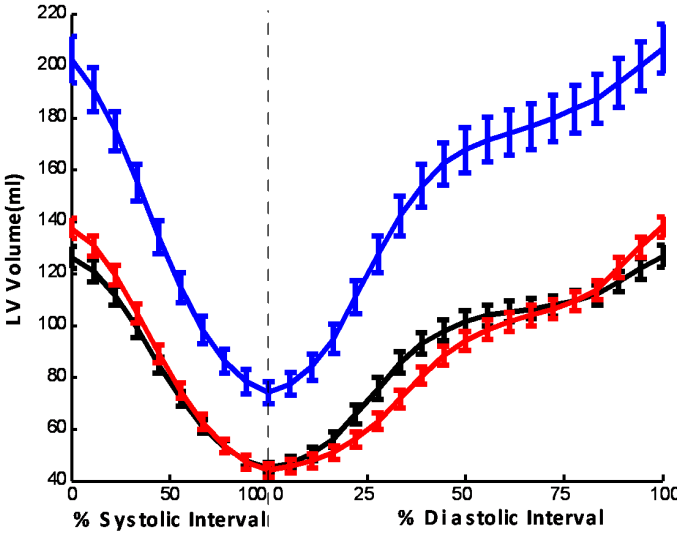

Figure 10.1: Volume time curve for the 3 groups. Data points are expressed as mean ± standard error. Normal is represented in black, hypertension is represented in red and mitral regurgitation is represented in blue. Early filling rate is significantly lower in Hypertension group compared to the other two groups.

propagated throughout the cardiac cycle using in-house software [115, 126] to create LV time-volume curves 10.1.

10.4 Torsional Deformation Analysis

Two-dimensional (2D) strain rates were measured using harmonic phase (HARP) analysis [49–51]. 2D torsion and torsion rates were measured by tracking a circular mesh of points in a basal and apical slice. The mesh was identified in the first time based on user-defined contours and tracked through the remaining imaged phases using improved HARP tracking [50, 52]. Because the tag lines faded with time due to T_1 relaxation, torsion was only computed through systole and the first 70% of diastole (see Figure 10.2).

10.5 Torsional Hysteresis

The torsion hysteresis area was computed with the following procedure for each subject. First, each point on the torsion-versus-time curve was divided by peak torsion, and each point on the LV volume-versus-time curve was divided by EDV to give normalized values. The

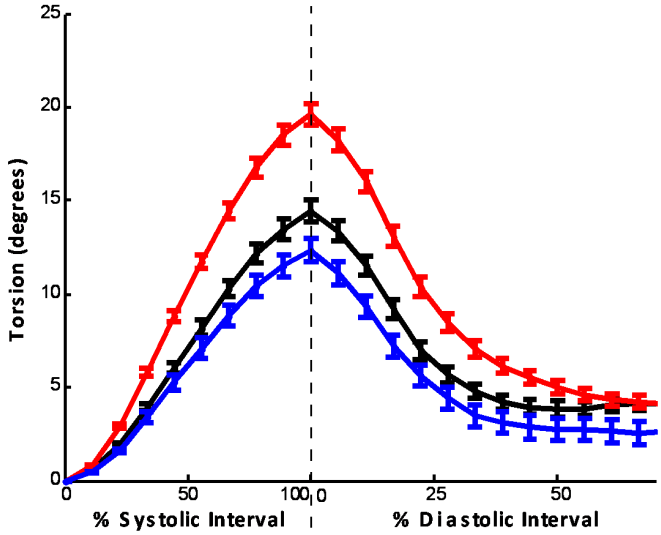

Figure 10.2: Torsion time curve for the 3 groups. Data points are expressed as mean ± standard error. Normal is represented in black, hypertension is represented in red and mitral regurgitation is represented in blue. Peak systolic torsion is highest in Hypertension group.

areas under the systolic and diastolic sections of the torsion-volume curve were computed numerically using the trapezoidal rule. Both areas were computed over the volume interval between the ESV and the volume at 70% diastole as shown in Figure 10.3. The normalized torsion hysteresis area was computed by subtracting the diastolic area from the systolic area. Similarly non-normalized torsion hysteresis was also computed.

10.6 Results and Discussion

The LV torsional hysteresis as measured by the net area difference was highest in HTN compared to MR or NL ($p < 0.001$) (Figures 10.4 and 10.5).

In this study we demonstrate for the first time that under distinct physiological conditions, one of eccentric remodeling (MR) and the other of concentric remodeling (HTN), the area within the torsion-volume loop (torsional hysteresis) is increased in HTN compared to NL or MR. We believe that the underlying mechanism for torsional hysteresis is likely due

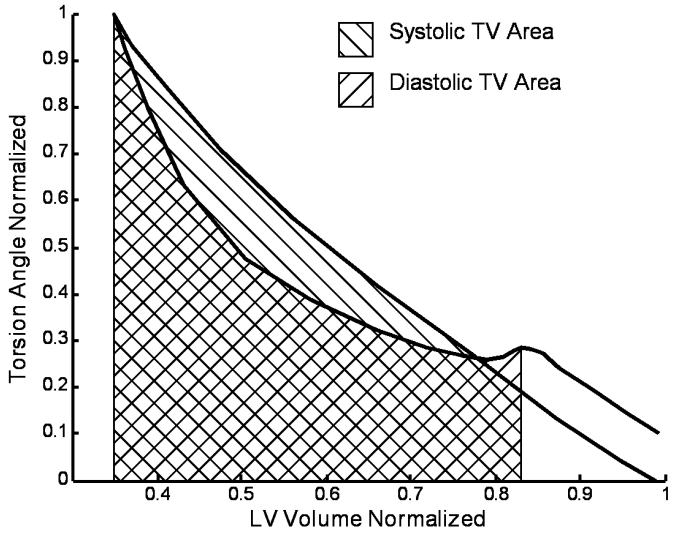

Figure 10.3: Schematic diagram for calculating torsional hysteresis. Torsional hysteresis represents the difference in area within the systolic and diastolic arms of the normalized torsion volume (TV) curves.

to loss of stored torsional energy through inefficient myocardial relaxation. Diastolic untwist/torsion is characterized by early rapid recoil with little change in LV volume, followed by more gradual untwisting when the bulk of diastolic filling occurs.

Hysteresis in the stress-strain relationship for a material is due to frictional losses during material motion; these stress-strain relationships may be linear (stretching); shear (sliding), or torsional (twisting), reflecting degrees of freedom in the motion of the body. Measurement of the torsional stress (i.e., the torque) is difficult in the heart in vivo. Therefore, we have used the LV volume as a surrogate for torque, since a twisting force acting on a shape with a larger radius will result in increased torque, compared to a shape with a smaller radius. In the case of the LV, apart from the intrinsic passive myocardial stiffness, the torsion-volume loop may also be influenced by the rate of LV filling and the active ATP dependent relaxation process occurring in the myofibrils. In HTN due to a stiffer ventricle, a greater amount of work is expended for both active and passive relaxation and therefore greater torsional hysteresis.

In our study we included MR as another group with a distinctly different remodeling compared to HTN. This group demonstrated eccentric remodeling with a dilated LV cavity

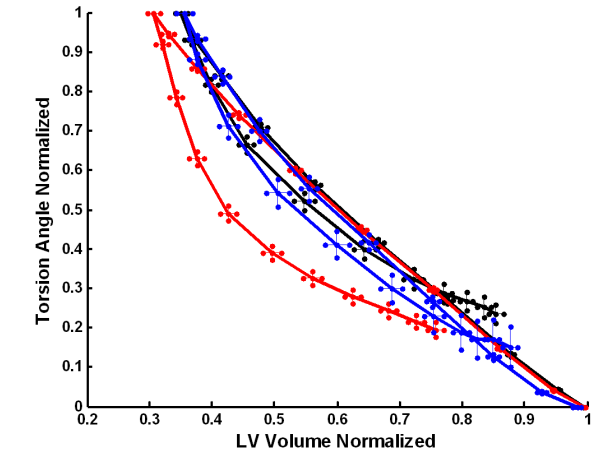

Figure 10.4: a) Normalized b) non-normalized torsion volume curves for the 3 groups. Data points are expressed as mean ± standard error. Normal is represented in black, hypertension is represented in red and mitral regurgitation is represented in blue. Torsional hysteresis as measured by the area within the systolic and diastolic arm is greater in Hypertension group compared to the other two groups.

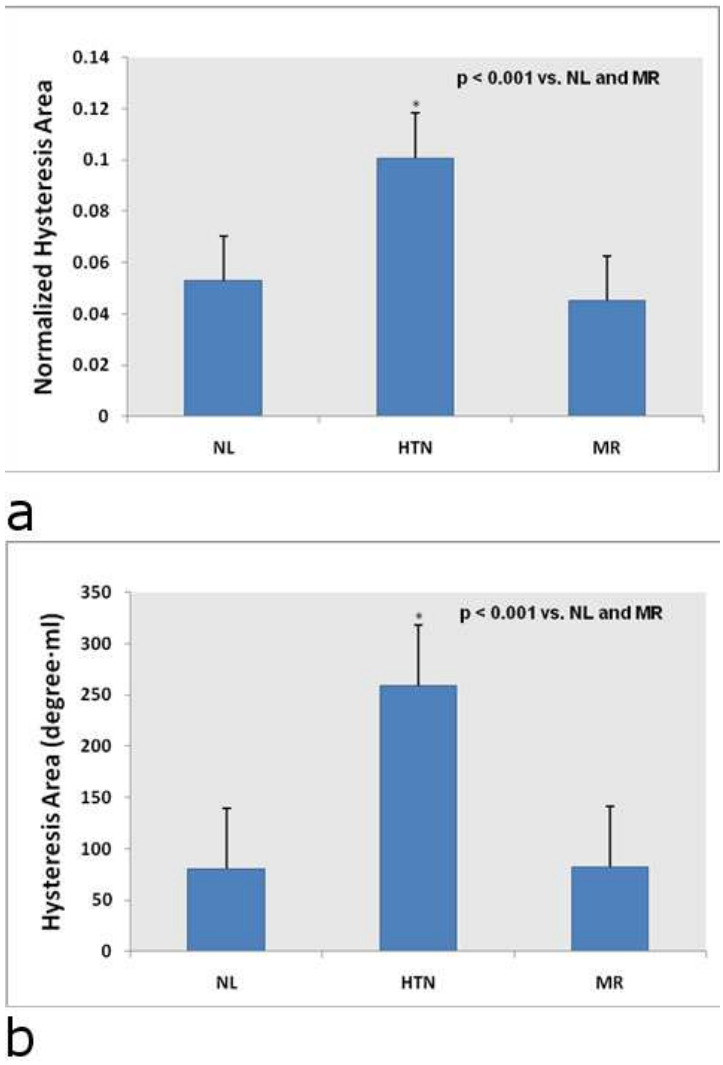

Figure 10.5: a) Normalized and b) non-normalized torsional hysteresis measured as described in Figure 10.3. Torsional hysteresis is significantly higher in Hypertension group compared to Mitral Regurgitation or Normal control groups.

but LVEF $> 60\%$. We found no difference in the torsional hysteresis in this group compared to NL. Previous investigators have demonstrated that there is a loss or at the most no net gain of collagen in MR [140]. The present study and previous studies have also demonstrated relatively preserved diastolic function as measured by conventional parameters in MR and preserved LVEF [141].

In conclusion, torsional hysteresis may be an important global parameter to assess both systolic and diastolic function. To our knowledge, this is the first study to propose the concept of torsional hysteresis as a measure of diastolic dysfunction, and its application may provide greater insight into multiple forms of cardiac hypertrophy and heart failure.

Chapter 11

Conclusion and Future Work

In this dissertation, a method to compute displacement measurements from tagged MR images is presented that depends on unwrapping the harmonic phase images. A branch-cut placement method was used to remove inconsistencies and unwrap the images. Temporal consistency is imposed while unwrapping the images. Initially, a GUI-based approach, called manual Strain from Unwrapped Phase (mSUP) was designed where the user placed branch-cuts. This was later replaced by a semi-automated method to place branch cuts in short-axis images, called computer-assisted Strain from Unwrapped Phase (caSUP). Using caSUP reduced the amount of manual intervention considerably.

The viability of applying the same methods in the right ventricle was also explored. Computing strains in the RV has proven especially difficult, but the application of unwrapped phase HARP to the RV (BiSUP) yielded accurate and quality 3D strain maps. BiSUP also demonstrated the ability to compute strains over time in hearts of different pathologies and morphologies.

An area of future work could be filtering techniques to obtain better phase images (with fewer residues). This would reduce the inconsistencies in the image, and consequently make the caSUP method faster while also requiring lesser manual intervention. Conversely, techniques such as CSPAMM could be used to obtain higher-quality tagged images, that would lead to fewer inconsistencies in the image and also reduce tag fading later in the cycle. Exploration of faster and more accurate algorithms to place branch cuts is another prospective area of research. It would especially be useful if this could be extended to 3D (in either time or spatial domain) in an efficient manner.

Finally, extensive data has been collected for this research. 110 patients and volunteers with 3D+t and 2D+t strains have been used. This could be useful in studying relationships between 3D and 2D strains and strain rates and specifically studying the advantages of 3D strain.

Bibliography

[1] "*http* : *//en.wikipedia.org/wiki/cardiology*."

[2] "*http* : *//www.invisionguide.com/heart/*."

[3] "http://www.cvphysiology.com/index.html."

[4] "*http* : *//www.columbiasurgery.org/pat/cardiac/anatomy.html*."

[5] "*http* : *//www.americanheart.org/*."

[6] J. L. Prince and J. M. Links, *Medical Imaging Signals and Systems*. Prentice-Hall, 2001.

[7] J. Li, "Tag line tracking and cardiac motion modeling from tagged MRI," Ph.D. dissertation, Auburn University, 2006.

[8] C. Ozturk, J. A. Derbyshire, and E. R. McVeigh, "Estimating motion from MRI data," *Proceedings of the IEEE*, vol. 91, no. 10, pp. 1627–1648, 2003.

[9] S. Masood, G.-Z. Yang, D. J. Pennell, and D. N. Firmin, "Investigating intrinsic myocardial mechanics: The role of MR tagging, velocity phase mapping and diffusion imaging," *Journal of Magnetic Resonance Imaging*, vol. 12, pp. 873–878, 2000.

[10] J. Duncan, P. Shi, T. Constble, and A. Sinusas, "Physical and geometrical modeling for image-based recovery of left ventricle deformation," *Progress in Biophysics and Molecular Biology*, vol. 69, no. 2-3, pp. 333–351, 1998.

[11] E. A. Zerhouni, D. M. Parish, W. J. Rogers, A. Yang, and E. P. Shapiro, "Human heart: tagging with MR imaging–a method for noninvasive assessment of myocardial motion," *Radiology*, vol. 169, no. 1, pp. 59–63, 1988.

[12] E. Atalar and E. R. McVeigh, "Optimization of tag thickness for measuring position with magnetic resonance imaging," *IEEE Transactions on Medical Imaging*, vol. 13, no. 1, pp. 152–160, 1994.

[13] J. Declerck, T. S. Denney, C. Ozturk, W. O'Dell, and E. R. McVeigh, "Left ventricular motion reconstruction from planar tagged MR images: a comparison," *Physics in Medicine and Biology*, vol. 45, no. 6, pp. 1611–1632, 2000.

[14] T. S. Denney and J. L. Prince, "Reconstruction of 3-D left ventricular motion from planar tagged cardiac MR images: an estimation theoretic approach," *Medical Imaging, IEEE Transactions on*, vol. 14, no. 4, pp. 625–635, 1995.

[15] J. Bogaert and F. E. Rademakers, "Regional nonuniformity of normal adult human left ventricle," *Am J Physiol Heart Circ Physiol*, vol. 280, no. 2, pp. H610–620, 2001.

[16] C. C. Moore, C. H. Lugo-Olivieri, E. R. McVeigh, and E. A. Zerhouni, "Three-dimensional systolic strain patterns in the normal human left ventricle: Characterization with tagged MR imaging," *Radiology*, vol. 214, no. 2, pp. 453–466, 2000.

[17] L. Axel, "Biomechanical dynamics of the heart with MRI," *Annual Review of Biomedical Engineering*, vol. 4, pp. 321–347, 2002.

[18] C. Petitjean, N. Rougon, and P. Cluzel, "Assessment of myocardial function: A review of quantification methods and results using tagged MRI," *Journal of Cardiovascular Magnetic Resonance*, vol. 7, no. 2, pp. 501–516, 2005.

[19] M. D. Cerqueira, N. J. Weissman, V. Dilsizian, A. K. Jacobs, S. Kaul, W. K. Laskey, D. J. Pennell, J. A. Rumberger, T. Ryan, and M. S. Verani, "Standardized myocardial segmentation and nomenclature for tomographic imaging of the heart: A statement for healthcare professionals from the cardiac imaging committee of the council on clinical cardiology of the American Heart Association," *Circulation*, vol. 105, no. 4, pp. 539–542, 2002. [Online]. Available: http://circ.ahajournals.org

[20] M. B. Buchalter, J. L. Weiss, W. J. Rogers, E. A. Zerhouni, M. L. Weisfeldt, R. Beyar, and E. P. Shapiro, "Noninvasive quantification of left ventricular rotational deformation in normal humans using magnetic resonance imaging myocardial tagging," *Circulation*, vol. 81, no. 4, pp. 1236–1244, 1990.

[21] R. E. Henson, S. K. Song, J. S. Pastorek, J. J. H. Ackerman, and C. H. Lorenz, "Left ventricular torsion is equal in mice and humans," *Am J Physiol Heart Circ Physiol*, vol. 278, no. 4, pp. H1117–1123, 2000.

[22] M. A. Fogel, K. B. Gupta, P. M. Weinberg, and E. A. Hoffman, "Regional wall motion and strain analysis across stages of Fontan reconstruction by magnetic resonance tagging," *Am J Physiol Heart Circ Physiol*, vol. 269, no. 3, pp. H1132–1152, 1995.

[23] E. Pettersen, T. Helle-Valle, T. Edvardsen, H. Lindberg, H.-J. Smith, B. Smevik, O. A. Smiseth, and K. Andersen, "Contraction pattern of the systemic right ventricle: Shift from longitudinal to circumferential shortening and absent global ventricular torsion," *Journal of the American College of Cardiology*, vol. 49, no. 25, pp. 2450–2456, 2007.

[24] E. W. Remme, K. F. Augenstein, A. A. Young, and P. J. Hunter, "Parameter distribution models for estimation of population based left ventricular deformation using sparse fiducial markers," *Medical Imaging, IEEE Transactions on*, vol. 24, no. 3, pp. 381–388, 2005.

[25] A. A. Young, C. M. Kramer, V. A. Ferrari, L. Axel, and N. Reichek, "Three dimensional left ventricular deformation in hypertrophic cardiomyopathy," *Circulation*, vol. 90, no. 2, pp. 854–867, 1994.

[26] I. Russel, M. Gotte, J. Kuijer, and J. T. Marcus, "Regional assessment of left ventricular torsion by CMR tagging," *Journal of Cardiovascular Magnetic Resonance*, vol. 10, no. 1, p. 26, 2008.

[27] L. Pan, J. Prince, J. Lima, and N. Osman, "Fast tracking of cardiac motion using 3D-HARP," *Biomedical Engineering, IEEE Transactions on*, vol. 52, no. 8, pp. 1425–1435, 2005.

[28] C. C. Moore, E. R. McVeigh, and E. A. Zerhouni, "Quantitative tagged magnetic resonance imaging of the normal human left ventricle," *Topics in Magnetic Resonance Imaging*, vol. 11, no. 6, pp. 359–371, 2000.

[29] I. Haber, D. N. Metaxas, and L. Axel, "Three-dimensional motion reconstruction and analysis of the right ventricle using tagged MRI," *Medical Image Analysis*, vol. 4, no. 4, pp. 335–355, 2000.

[30] J. Garcia-Barnes, D. Gil, J. Barajas, F. Carreras, S. Pujadas, and P. Radeva, "Characterization of ventricular torsion in healthy subjects using gabor filters and a variational framework," in *Computers in Cardiology, 2006*, 2006, pp. 877–880.

[31] R. Mankad, C. J. McCreery, W. J. Rogers, R. J. Weichmann, E. B. Savage, N. Reichek, and C. M. Kramer, "Regional myocardial strain before and after mitral valve repair for severe mitral regurgitation," *Journal of Cardiovascular Magnetic Resonance*, vol. 3, no. 3, pp. 257 – 266, 2001.

[32] S.-J. Dong, A. P. Crawley, J. H. MacGregor, Y. F. Petrank, D. W. Bergman, I. Belenkie, E. R. Smith, J. V. Tyberg, and R. Beyar, "Regional left ventricular systolic function in relation to the cavity geometry in patients with chronic right ventricular pressure overload : A three-dimensional tagged magnetic resonance imaging study," *Circulation*, vol. 91, no. 9, pp. 2359–2370, 1995.

[33] C. F. Azevedo, L. C. Amado, D. L. Kraitchman, B. L. Gerber, N. F. Osman, C. E. Rochitte, T. Edvardsen, and J. A. C. Lima, "Persistent diastolic dysfunction despite complete systolic functional recovery after reperfused acute myocardial infarction demonstrated by tagged magnetic resonance imaging," *Eur Heart J*, vol. 25, no. 16, pp. 1419–1427, 2004.

[34] A. A. Young, H. Imai, C. N. Chang, and L. Axel, "Two-dimensional left ventricular deformation during systole using magnetic resonance imaging with spatial modulation of magnetization," *Circulation*, vol. 89, no. 2, pp. 740 – 752, 1994.

[35] D. Bree, J. R. Wollmuth, B. P. Cupps, M. D. Krock, A. Howells, J. Rogers, N. Moazami, and M. K. Pasque, "Low-dose dobutamine tissue-tagged magnetic resonance imaging with 3-dimensional strain analysis allows assessment of myocardial viability in patients with ischemic cardiomyopathy," *Circulation*, vol. 114, no. 1suppl, pp. I–33–36, 2006.

[36] P. Moustakidis, B. P. Cupps, B. J. Pomerantz, R. P. Scheri, H. S. Maniar, A. M. Kates, R. J. Gropler, M. K. Pasque, and T. M. Sundt, "Noninvasive, quantitative assessment

of left ventricular function in ischemic cardiomyopathy," *Journal of Surgical Research*, vol. 116, no. 2, pp. 187–196, 2004.

[37] H. Kanzaki, S. Nakatani, N. Yamada, S.-i. Urayama, K. Miyatake, and M. Kitakaze, "Impaired systolic torsion in dilated cardiomyopathy: Reversal of apical rotation at mid-systole characterized with magnetic resonance tagging method," *Basic Research in Cardiology*, vol. 101, no. 6, pp. 465–470, 2006, 10.1007/s00395-006-0603-6.

[38] E. Nagel, M. Stuber, M. Lakatos, M. B. Scheidegger, P. Boesiger, and O. M. Hess, "Cardiac rotation and relaxation after anterolateral myocardial infarction," *Coron Artery Dis*, vol. 11, pp. 261 – 267, 2000.

[39] M. Stuber, M. B. Scheidegger, S. E. Fischer, E. Nagel, F. Steinemann, O. M. Hess, and P. Boesiger, "Alterations in the local myocardial motion pattern in patients suffering from pressure overload due to aortic stenosis," *Circulation*, vol. 100, no. 4, pp. 361–8, 1999.

[40] H. C. Oxenham, A. A. Young, B. R. Cowan, T. L. Gentles, C. J. Occleshaw, C. G. Fonseca, R. N. Doughty, and N. Sharpe, "Age-related changes in myocardial relaxation using three-dimensional tagged magnetic resonance imaging," *Journal of Cardiovascular Magnetic Resonance*, vol. 5, no. 3, pp. 421 – 430, 2003.

[41] J. L. Prince and E. R. McVeigh, "Motion estimation from tagged MR image sequences," *IEEE Transactions on Medical Imaging*, vol. 11, no. 2, pp. 238–249, 1992.

[42] J. L. Prince and E. R. McVeigh, "Optical flow for tagged MR images," *IEEE Transactions on Medical Imaging*, vol. 7, pp. 2441–2444, 1991.

[43] J. L. Prince, S. N. Gupta, and N. F. Osman, "Bandpass optical flow for tagged MRI." *Med Phys*, vol. 27, no. 1, pp. 108–118, 2000.

[44] M. A. Guttman, J. L. Prince, and E. R. Mcveigh, "Tag and contour detection in tagged MR images of the left ventricle," *IEEE Transactions on Medical Imaging*, vol. 13, no. 1, pp. 74–88, 1994.

[45] T. S. Denney, "Estimation and detection of myocardial tags in MR image without user-defined myocardial contours," *IEEE Transactions on Medical Imaging*, vol. 18, no. 4, pp. 330–334, 1999.

[46] Z. Qian, A. Montillo, D. Metaxas, and L. Axel, "Segmenting MRI tagging lines using gabor filter banks," *International Conference on the Engineering in Medical and Biology Society*, pp. 630–633, 2003.

[47] D. Xiang and T. S. Denney, "Combined tag tracking and myocardium motion reconstruction from planar tagged MR image data without user-defined myocardial contours," in *Biomedical Imaging: Nano to Macro, 2004. IEEE International Symposium on*, 2004, pp. 888–891 Vol. 1.

[48] L. Xiaofeng, E. Murano, M. Stone, and J. L. Prince, "HARP tracking refinement using seeded region growing," in *Biomedical Imaging: From Nano to Macro, 2007. ISBI 2007. 4th IEEE International Symposium on*, 2007, pp. 372–375.

[49] N. F. Osman and E. R. McVeigh, "Imaging heart motion using harmonic phase MRI," *IEEE Transactions on Medical Imaging*, vol. 19, no. 3, pp. 186–202, 2000.

[50] N. F. Osman, W. S. Kerwin, E. R. McVeigh, and J. L. Prince, "Cardiac motion tracking using cine harmonic phase (HARP) magnetic resonance imaging," *Magnetic Resonance in Medicine*, vol. 42, no. 6, pp. 1048–1060, 1999.

[51] W. Liu, J. Chen, S. Ji, J. S. Allen, P. V. Bayly, S. A. Wickline, and X. Yu, "Harmonic phase MR tagging for direct quantification of Lagrangian strain in rat hearts after myocardial infarction." *Magn Reson Med*, vol. 52, no. 6, pp. 1282–1290, 2004.

[52] A. Khalifa, A. B. M. Youssef, and N. Osman, "Improved Harmonic Phase (HARP) method for motion tracking a tagged cardiac MR images." *Conf Proc IEEE Eng Med Biol Soc*, vol. 4, pp. 4298–4301, 2005.

[53] J. Goutsias and S. Batman, "Morphological methods for biomedical image analysis." in *Handbook of Medical Imaging: Medical Imaging Processing and Analysis*, M. Sonka and J. Fitzpatrick, Eds. SPIE, 2000, pp. 255–263.

[54] Y. Chen and A. Amini, "A MAP framework for tagline detetction in SPAMM data using Markov random fields on the B-spline solid," *IEEE Workshop on Mathematical Models in Biomedical Image Analysis*, pp. 131–138, 2001.

[55] D. N. Metaxas, L. Axel, H. Zhenhua, A. Montillo, K. Park, and Q. Zhen, "Segmentation and analysis of 3D cardiac motion from tagged MRI images," in *Engineering in Medicine and Biology Society, 2003. Proceedings of the 25th Annual International Conference of the IEEE*, vol. 1, 2003, pp. 122–125 Vol.1.

[56] D. N. Metaxas, L. Axel, Z. Qian, and X. Huang, "A segmentation and tracking system for 4D cardiac tagged MR images," in *Engineering in Medicine and Biology Society, 2006. EMBS '06. 28th Annual International Conference of the IEEE*, 2006, pp. 1541–1544.

[57] Z. Qian, D. Metaxas, and L. Axel, "A learning framework for the automatic and accurate segmentation of cardiac tagged MRI images," in *Computer Vision for Biomedical Image Applications*, 2005, pp. 93–102, 10.1007/11569541 11.

[58] W. Feng, T. S. Denney, S. Lloyd, L. Dell'Italia, and H. Gupta, "Contour regularized left ventricular strain analysis from cine MRI," in *Biomedical Imaging: From Nano to Macro, 2008. ISBI 2008. 5th IEEE International Symposium on*, 2008, pp. 520–523.

[59] L. Axel, A. Montillo, and D. Kim, "Tagged magnetic resonance imaging of the heart: A survey," *Medical Image Analysis*, vol. 9, pp. 376–393, 2005.

[60] C. A. Davis, L. Jin, and T. S. Denney, "Analysis of spectral changes and filter design in tagged cardiac MRI," in *Biomedical Imaging: Nano to Macro, 2006. 3rd IEEE International Symposium on*, 2006, pp. 137–140.

[61] M. Marinelli, V. Positand, N. F. Osman, F. A. Recchia, M. Lombardi, and L. Landini, "Automatic filter design in HARP analysis of tagged magnetic resonance images," in *Biomedical Imaging: From Nano to Macro, 2008. ISBI 2008. 5th IEEE International Symposium on*, 2008, pp. 1429–1432.

[62] A. A. Amir, W. C. Rupert, and C. G. John, "Snakes and splines for tracking non-rigid heart motion," 1996, 649040 251-261.

[63] A. A. Amini, Y. Chen, J. Sun, and V. Mani, "Constrained thin-plate spline reconstruction of 2D deformations from tagged MRI," 1998, 836884 36.

[64] A. A. Amini, C. Yasheng, R. W. Curwen, V. Mani, and J. Sun, "Coupled B-snake grids and constrained thin-plate splines for analysis of 2-D tissue deformations from tagged MRI," *Medical Imaging, IEEE Transactions on*, vol. 17, no. 3, pp. 344–356, 1998.

[65] P. Radeva, A. Amini, H. Jiantao, and E. Marti, "Deformable B-solids and implicit snakes for localization and tracking of SPAMM MRI-data," in *Mathematical Methods in Biomedical Image Analysis, 1996., Proceedings of the Workshop on*, 1996, pp. 192–201.

[66] W. S. Kerwin and J. L. Prince, "Cardiac material markers from tagged MR images," *Medical Image Analysis*, vol. 2, no. 4, pp. 339–353, 1998.

[67] A. A. Young, D. L. Kraitchman, L. Dougherty, and L. Axel, "Tracking and finite element analysis of stripe deformation in magnetic resonance tagging," *Medical Imaging, IEEE Transactions on*, vol. 14, no. 3, pp. 413–421, 1995.

[68] A. A. Young, "Model tags: direct three-dimensional tracking of heart wall motion from tagged magnetic resonance images," *Medical Image Analysis*, vol. 3, no. 4, pp. 361–372, 1999.

[69] W. G. O'Dell, C. C. Moore, W. C. Hunter, E. A. Zerhouni, and E. R. McVeigh, "Three-dimensional myocardial deformations: calculation with displacement field fitting to tagged MR images," *Radiology*, vol. 195, no. 3, pp. 829–835, 1995.

[70] R. Chandrashekara, R. H. Mohiaddin, and D. Rueckert, "Analysis of 3-D myocardial motion in tagged MR images using nonrigid image registration," *Medical Imaging, IEEE Transactions on*, vol. 23, no. 10, pp. 1245–1250, 2004.

[71] D. Perperidis, R. H. Mohiaddin, and D. Rueckert, "Spatio-temporal free-form registration of cardiac MR image sequences," *Medical Image Analysis*, vol. 9, no. 5, pp. 441–456, 2005.

[72] C. Ozturk and E. R. McVeigh, "Four-dimensional B-spline based motion analysis of tagged MR images: introduction and in vivo validation," *Physics in Medicine and Biology*, vol. 45, pp. 1683–1702, 2000.

[73] J. Huang, D. Abendschein, V. G. Davila-Roman, and A. A. Amini, "Spatio-temporal tracking of myocardial deformations with a 4-D B-spline model from tagged MRI," *Medical Imaging, IEEE Transactions on*, vol. 18, no. 10, pp. 957–972, 1999.

[74] N. J. Tustison and A. A. Amini, "Biventricular myocardial strains via nonrigid registration of AnFigatomical NURBS models," *Medical Imaging, IEEE Transactions on*, vol. 25, no. 1, pp. 94–112, 2006.

[75] N. F. Osman and J. L. Prince, "Visualizing myocardial function using HARP MRI," *Phys. Med. Biol.*, vol. 45, pp. 1665–1682, 2000.

[76] Z. A.-E. Khaled, P. Vijay, and L. P. Jerry, "Artifact reduction in HARP strain maps using anisotropic smoothing," M. Armando and A. A. Amir, Eds., vol. 6143. SPIE, 2006, p. 61432P, medical Imaging 2006: Physiology, Function, and Structure from Medical Images 1.

[77] S. R. Tecelao, J. J. M. Zwanenburg, J. P. A. Kuijer, and J. T. Marcus, "Extended harmonic phase tracking of myocardial motion: improved coverage of myocardium and its effects on strain results," *J Magn Res Im*, vol. 23, pp. 682 – 690, 2006.

[78] M. J. Ledesma-Carbayo, J. A. Derbyshire, S. Sampath, A. Santos, M. Desco, and E. R. McVeigh, "Unsupervised estimation of myocardial displacement from tagged MR sequences using nonrigid registration," *Magnetic Resonance in Medicine*, vol. 59, no. 1, pp. 181–189, 2008, 10.1002/mrm.21444.

[79] S. Ryf, M. A. Spiegel, M. Gerber, and P. Boesiger, "Myocardial tagging with 3D-CSPAMM," *Journal of Magnetic Resonance Imaging*, vol. 16, no. 3, pp. 320–325, 2002, 10.1002/jmri.10145.

[80] N. Pelc, R. Herfkens, A. Shimakawa, and D. Enzmann, "Phase contrast cine magnetic resonance imaging," *Magn Reson Q.*, vol. 7, no. 4, pp. 229–54, 1991.

[81] E. Bergvall, P. Cain, H. Arheden, and G. Sparr, "A fast and highly automated approach to myocardial motion analysis using phase contrast magnetic resonance imaging," *Journal of Magnetic Resonance Imaging*, vol. 23, no. 5, pp. 652–661, 2006, 10.1002/jmri.20565.

[82] B. S. Spottiswoode, X. Zhong, A. T. Hess, C. M. Kramer, E. M. Meintjes, B. M. Mayosi, and F. H. Epstein, "Tracking myocardial motion from cine DENSE images using spatiotemporal phase unwrapping and temporal fitting," *Medical Imaging, IEEE Transactions on*, vol. 26, no. 1, pp. 15–30, 2007.

[83] A. H. Aletras, S. Ding, R. S. Balaban, and H. Wen, "DENSE: Displacement encoding with stimulated echoes in cardiac functional MRI," *Journal of Magnetic Resonance*, vol. 137, no. 1, pp. 247–252, 1999.

[84] D. Kim, W. D. Gilson, C. M. Kramer, and F. H. Epstein, "Myocardial tissue tracking with two-dimensional cine displacement-encoded MR imaging: Development and initial evaluation," *Radiology*, p. 2303021213, 2004.

[85] S. Sampath, N. F. Osman, and J. L. Prince, "A combined harmonic phase and strain-encoded pulse sequence for measuring three-dimensional strain," *Magnetic Resonance Imaging*, vol. 27, no. 1, pp. 55–61, 2009.

[86] K. Z. Abd-Elmoniem, M. Stuber, and J. L. Prince, "Direct three-dimensional myocardial strain tensor quantification and tracking using zharp," pp. 778–786, 2008.

[87] S. Sampath and J. L. Prince, "Automatic 3d tracking of cardiac material markers using slice-following and harmonic-phase MRI," *Magnetic Resonance Imaging*, vol. 25, no. 2, pp. 197–208, 2007.

[88] A. H. Aletras, R. S. Balaban, and H. Wen, "High-resolution strain analysis of the human heart with Fast-DENSE," *Journal of Magnetic Resonance*, vol. 140, no. 1, pp. 41–57, 1999.

[89] D. C. Ghiglia and M. D. Pritt, *Two-dimensional phase unwrapping : theory, algorithms, and software*. New York: Wiley, 1998.

[90] B. Ambale, H. Gupta, S. G. Lloyd, L. D. 'Italia, and T. S. Denney, "3D left ventricular strain from unwrapped harmonic phase measurements," *Journal of Magnetic Resonance Imaging*, vol. 31, no. 4, pp. 854–862, 2010. [Online]. Available: http://dx.doi.org/10.1002/jmri.22099

[91] B. Ambale, T. S. Denney, H. Gupta, S. Lloyd, and L. Dell'Italia, "Measuring 3D left ventricular strain from unwrapped harmonic phase," in *Biomedical Imaging: From Nano to Macro, 2008. ISBI 2008. 5th IEEE International Symposium on*, 2008, pp. 1433–1436.

[92] B. Ambale, S. Lloyd, T. S. Denney, L. Dell'Italia, R. Benza, and H. Gupta, "Comparison of 2D and 3D torsion measured from tagged MRI," in *17th Meeting of the International Society for Magnetic Resonance in Medicine*, April 2009.

[93] B. Ambale, S. Lloyd, T. S. Denney, L. Dell'Italia, R. Benza, and H. Gupta, "4D right ventricular strain and geometry in pulmonary hypertension and normals," in *18th Meeting of the International Society for Magnetic Resonance in Medicine*, April 2010.

[94] B. Ambale, S. Lloyd, T. S. Denney, L. Dell'Italia, R. Benza, and H. Gupta, "3D right ventricular strain and geometry in pulmonary hypertension and normals," in *16th Meeting of the International Society for Magnetic Resonance in Medicine*, May 2008.

[95] B. Ambale, T. S. Denney, H. Gupta, S. Lloyd, and L. Dell'Italia, "3D left ventricular strain by phase unwrapping: a simulated annealing based branch-cut placement method," in *Proceedings of the Sixth IEEE international conference on Symposium on Biomedical Imaging: From Nano to Macro*. Boston, Massachusetts, USA: IEEE Press, 2009, pp. 466–469.

[96] W. Xu and I. Cumming, "A region-growing algorithm for InSAR phase unwrapping," *Geoscience and Remote Sensing, IEEE Transactions on*, vol. 37, no. 1, pp. 124–134, 1999.

[97] D. C. Ghiglia and L. A. Romero, "Robust two-dimensional weighted and unweighted phase unwrapping that uses fast transforms and iterative methods," *Journal- Optical Society OF America*, vol. 11, pp. 1–107, 1994.

[98] S. Moon-Ho Song, S. Napel, N. Pelc, and G. Glover, "Phase unwrapping of MR phase images using poisson equation," *Image Processing, IEEE Transactions on*, vol. 4, no. 5, pp. 667–676, 1995.

[99] U. Spagnolini, "2-d phase unwrapping and instantaneous frequency estimation," *Geoscience and Remote Sensing, IEEE Transactions on*, vol. 33, no. 3, pp. 579–589, 1995.

[100] T. Flynn, "Consistent 2-D phase unwrapping guided by a quality map," *Geoscience and Remote Sensing Symposium, 1996. IGARSS '96. 'Remote Sensing for a Sustainable Future.', International*, vol. 4, pp. 2057–2059vol.4, 1996.

[101] S. Kim and Y.-S. Kim, "Least squares phase unwrapping in wavelet domain," *Vision, Image and Signal Processing, IEE Proceedings-*, vol. 152, no. 3, pp. 261–267, 2005.

[102] B. Friedlander and J. Francos, "Model based phase unwrapping of 2-D signals," *Signal Processing, IEEE Transactions on [see also Acoustics, Speech, and Signal Processing, IEEE Transactions on]*, vol. 44, no. 12, pp. 2999–3007, 1996.

[103] N. Ching, D. Rosenfeld, and M. Braun, "Two-dimensional phase unwrapping using a minimum spanning tree algorithm," *Image Processing, IEEE Transactions on*, vol. 1, no. 3, pp. 355–365, 1992.

[104] R. Sivley and J. Havlicek, "Multidimensional phase unwrapping for consistent APF estimation," *Image Processing, 2005. ICIP 2005. IEEE International Conference on*, vol. 2, pp. II–458–61, 2005.

[105] C. Chen and H. Zebker, "Phase unwrapping for large SAR interferograms: statistical segmentation and generalized network models," *Geoscience and Remote Sensing, IEEE Transactions on*, vol. 40, no. 8, pp. 1709–1719, 2002.

[106] H. A. Zebker and Y. Lu, "Phase unwrapping algorithms for radar interferometry: residue-cut, least-squares, and synthesis algorithms," *J. Opt. Soc. Am. A*, vol. 15, no. 3, pp. 586–598, 1998. [Online]. Available: http://josaa.osa.org/abstract.cfm?URI=josaa-15-3-586

[107] B. R. Hunt, "Matrix formulation of the reconstruction of phase values from phase differences," *Journal of the Optical Society of America (1917-1983)*, vol. 69, p. 393, 1979.

[108] M. Pritt, "Comparison of path-following and least-squares phase unwrapping algorithms," *Geoscience and Remote Sensing, 1997. IGARSS '97. 'Remote Sensing - A Scientific Vision for Sustainable Development'., 1997 IEEE International*, vol. 2, pp. 872–874vol.2, 1997.

[109] T. S. Denney and J. L. Prince, "Optimal brightness functions for optical flow estimation of deformable motion," *Image Processing, IEEE Transactions on*, vol. 3, no. 2, pp. 178–191, 1994.

[110] H. Wen, K. A. Marsolo, E. E. Bennett, K. S. Kutten, R. P. Lewis, D. B. Lipps, N. D. Epstein, J. F. Plehn, and P. Croisille, "Adaptive postprocessing techniques for myocardial tissue tracking with displacement-encoded MR imaging," *Radiology*, vol. 246, no. 1, pp. 229–240, 2008. [Online]. Available: http://radiology.rsnajnls.org/cgi/content/abstract/246/1/229

[111] D. Xiang and T. S. Denney, "Three-dimensional myocardial strain reconstruction from tagged MRI using a cylindrical B-spline model," *Medical Imaging, IEEE Transactions on*, vol. 23, no. 7, pp. 861–867, 2004.

[112] M. D. Pritt, "Phase unwrapping by means of multigrid techniques for interferometric SAR," *Geoscience and Remote Sensing, IEEE Transactions on*, vol. 34, no. 3, pp. 728–738, 1996.

[113] J. P. Kuijer, M. B. M. Hofman, J. J. M. Zwanenburg, J. T. Marcus, A. C. v. Rossum, and R. M. Heethaar, "DENSE and HARP: Two views on the same technique of phase-based strain imaging," *Journal of Magnetic Resonance Imaging*, vol. 24, no. 6, pp. 1432–1438, 2006, 10.1002/jmri.20749.

[114] T. S. Denney and E. R. McVeigh, "Model-Free reconstruction of three-dimensional myocardial strain from planar tagged MR images," *J Magn Reson Imaging.*, vol. 7, no. 5, pp. 799–810, 1997.

[115] W. Feng, H. Nagaraj, H. Gupta, S. Lloyd, I. Aban, G. Perry, D. Calhoun, L. Dell'Italia, and T. S. Denney, "A dual propagation contours technique for semi-automated assessment of systolic and diastolic cardiac function by CMR," *Journal of Cardiovascular Magnetic Resonance*, vol. 11, no. 1, p. 30, 2009. [Online]. Available: http://www.jcmr-online.com/content/11/1/30

[116] J. Li and T. S. Denney, "Left ventricular motion reconstruction with a prolate spheroidal B-spline model." *Phys Med Biol*, vol. 51, no. 3, pp. 517–537, 2006.

[117] N. Osman and J. Prince, "On the design of the bandpass filters in harmonic phase MRI," *Image Processing, 2000. Proceedings. 2000 International Conference on*, vol. 1, pp. 625–628vol.1, 2000.

[118] T. S. Denney, L. Yan, and B. L. Gerber, "Unsupervised reconstruction of a three-dimensional left ventricular strain from parallel tagged cardiac images," *Magnetic Resonance in Medicine*, vol. 49, no. 4, pp. 743–754–, 2003. [Online]. Available: http://dx.doi.org/10.1002/mrm.10434

[119] A. N. Borg, J. L. Harrison, R. A. Argyle, and S. G. Ray, "Left ventricular torsion in primary chronic mitral regurgitation," *Heart*, vol. 94, no. 5, pp. 597–603, 2008.

[120] P. P. Sengupta, A. J. Tajik, K. Chandrasekaran, and B. K. Khandheria, "Twist mechanics of the left ventricle: Principles and application," *JACC: Cardiovascular Imaging*, vol. 1, no. 3, pp. 366 – 376, 2008.

[121] D. Jerome, A. Nicholas, and R. M. Elliot, "Use of a 4D planispheric transformation for the tracking and analysis of LV motion with tagged MR images," C. Chin-Tu and V. C. Anne, Eds., vol. 3660. SPIE, 1999, pp. 69–80, medical Imaging 1999: Physiology and Function from Multidimensional Images 1.

[122] Z. A. Fayad, V. A. Ferrari, D. L. Kraitchman, A. A. Young, H. I. Palevsky, D. C. Bloomgarden, and L. Axel, "Right ventricular regional function using MR tagging: Normals versus chronic pulmonary hypertension," *Magn. Reson. Med.*, vol. 39, no. 1, pp. 116–123, 1998. [Online]. Available: http://dx.doi.org/10.1002/mrm.1910390118

[123] S. S. Klein, T. P. Graham, and C. H. Lorenz, "Noninvasive delineation of normal right ventricular contractile motion with magnetic resonance imaging myocardial tagging," *Annals of Biomedical Engineering*, vol. 26, pp. 756–763, 1998, 10.1114/1.75. [Online]. Available: http://dx.doi.org/10.1114/1.75

[124] A. A. Young, Z. A. Fayad, and L. Axel, "Right ventricular midwall surface motion and deformation using magnetic resonance tagging," *Am J Physiol Heart Circ Physiol*, vol. 271, no. 6, pp. H2677–2688, Dec. 1996. [Online]. Available: http://ajpheart.physiology.org/cgi/content/abstract/271/6/H2677

[125] B. Gutmann and H. Weber, "Phase unwrapping with the branch-cut method: Clustering of discontinuity sources and reverse simulated annealing," *Appl. Opt.*, vol. 38, no. 26, pp. 5577–5593, 1999.

[126] W. Feng, H. Gupta, S. Lloyd, l. D. Italia, and T. S. Denney, "Myocardial contour propagation in cine cardiac MRI." ISMRM, May 2007, p. 766.

[127] M. R. Zile, C. F. Baicu, and W. H. Gaasch, "Diastolic heart failure–abnormalities in active relaxation and passive stiffness of the left ventricle," *N Engl J Med*, vol. 350, no. 19, pp. 1953–9, 2004.

[128] M. M. Redfield, S. J. Jacobsen, B. A. Borlaug, R. J. Rodeheffer, and D. A. Kass, "Age- and gender-related ventricular-vascular stiffening: a community-based study," *Circulation*, vol. 112, no. 15, pp. 2254–62, 2005.

[129] S. P. Bell, L. Nyland, M. D. Tischler, M. McNabb, H. Granzier, and M. M. LeWinter, "Alterations in the determinants of diastolic suction during pacing tachycardia," Cardiology Unit, University of Vermont College of Medicine, Burlington, VT, USA., pp. 235–40, 2000.

[130] F. E. Rademakers, M. B. Buchalter, W. J. Rogers, E. A. Zerhouni, M. L. Weisfeldt, J. L. Weiss, and E. P. Shapiro, "Dissociation between left ventricular untwisting and filling - accentuation by cathecholamines," *Circulation*, vol. 85, no. 4, pp. 1572 – 1581, 1992.

[131] S.-J. Dong, P. S. Hees, C. O. Siu, J. L. Weiss, and E. P. Shapiro, "Mri assessment of lv relaxation by untwisting rate: a new isovolumic phase measure of tau," *Am J Physiol Heart Circ Physiol*, vol. 281, no. 5, pp. H2002–2009, 2001. [Online]. Available: http://ajpheart.physiology.org/cgi/content/abstract/281/5/H2002

[132] A. T. Burns, A. La Gerche, D. L. Prior, and A. I. MacIsaac, "Left ventricular untwisting is an important determinant of early diastolic function," *J Am Coll Cardiol Img*, vol. 2, no. 6, pp. 709–716, 2009. [Online]. Available: http://imaging.onlinejacc.org/cgi/content/abstract/2/6/709

[133] W. Hosford. New York, NY: Cambridge University Press, 2005.

[134] J. M. Huyghe, D. H. van Campen, T. Arts, and R. M. Heethaar, "The constitutive behaviour of passive heart muscle tissue: a quasi-linear viscoelastic formulation," *J Biomech*, vol. 24, no. 9, pp. 841–9, 1991.

[135] J. Layland, I. S. Young, and J. D. Altringham, "The length dependence of work production in rat papillary muscles in vitro," *J Exp Biol*, vol. 198, no. Pt 12, pp. 2491–9, 1995.

[136] C. E. Miller, M. A. Vanni, L. A. Taber, and B. B. Keller, "Passive stress-strain measurements in the stage-16 and stage-18 embryonic chick heart," *J Biomech Eng*, vol. 119, no. 4, pp. 445–51, 1997.

[137] C. E. Miller and C. L. Wong, "Trabeculated embryonic myocardium shows rapid stress relaxation and non-quasi-linear viscoelastic behavior," *J Biomech*, vol. 33, no. 5, pp. 615–22, 2000.

[138] C. E. Miller, C. L. Wong, and D. Sedmera, "Pressure overload alters stress-strain properties of the developing chick heart," *Am J Physiol Heart Circ Physiol*, vol. 285, no. 5, pp. H1849–56, 2003.

[139] J. H. Omens, D. E. Milkes, and J. W. Covell, "Effects of pressure overload on the passive mechanics of the rat left ventricle," *Ann Biomed Eng*, vol. 23, no. 2, pp. 152–63, 1995.

[140] T. D. Ryan, E. C. Rothstein, I. Aban, J. A. Tallaj, A. Husain, P. A. Lucchesi, and L. J. Dell'Italia, "Left ventricular eccentric remodeling and matrix loss are mediated by bradykinin and precede cardiomyocyte elongation in rats with volume overload," *Journal of the American College of Cardiology*, vol. 49, no. 7, pp. 811–821, 2007.

[141] W. J. Corin, T. Murakami, E. S. Monrad, O. M. Hess, and H. P. Krayenbuehl, "Left ventricular passive diastolic properties in chronic mitral

regurgitation," *Circulation*, vol. 83, no. 3, pp. 797–807, 1991. [Online]. Available: http://circ.ahajournals.org/cgi/content/abstract/83/3/797